ON THE USE OF ENTROPY PRODUCTION TO IMPROVE MATHEMATICAL MODELS AND NUMERICAL METHODS FOR NON-DILUTE FLOW AND TRANSPORT IN POROUS MEDIA

Timothy M. Weigand

A dissertation submitted to the faculty of the University of North Carolina at Chapel Hill in partial fulfillment of the requirements for the degree of Doctor of Philosophy in the Department of Environmental Sciences and Engineering.

Chapel Hill
2020

Approved by:

Cass T. Miller

David Adalsteinsson

Matthew W. Farthing

William G. Gray

Richard M. McLaughlin

William Vizuete

ABSTRACT

Timothy M. Weigand: On the Use of Entropy Production to Improve Mathematical Models and Numerical Methods for Non-Dilute Flow and Transport in Porous Media
(Under the direction of Cass T. Miller)

Non-dilute flow and transport in porous media plays an important role in many natural and engineered systems, however a mature understanding is lacking. As environmental conditions change and water resources become scarcer, the need for a more complete understanding of non-dilute flow and transport will be necessary to address future challenges, for example, assessing impacts of climate change on fresh water supplies and examining mitigation strategies. The thermodynamically constrained averaging theory (TCAT) is an approach for developing mathematical models that ties together conservation and thermodynamic laws and connects all spatial scales. This approach is used to develop a new macroscale model for non-dilute flow and transport in porous media. This model is found to more accurately describe a set of non-dilute laboratory displacement experiments as compared to existing models. Through the development of the model, an entropy production rate is derived and a new numerical method is formulated that utilizes the entropy production rate to improve computational efficiency. The general framework of this new approach can be applied to other models where the entropy production rate is known. To further improve macroscale models and our understanding of non-dilute behavior, microscale simulations are performed. As TCAT relates all spatial scales, the microscale simulations are averaged to gain insight on macroscale behavior. The importance that density, viscosity, and activity have on macroscale transport is assessed and microscale velocity distributions are analyzed to explain gravity stabilization and macroscale transport behavior.

ACKNOWLEDGEMENTS

Thank you to my family, friends, collaborators, fellow students, committee, and especially, Casey Miller.

TABLE OF CONTENTS

LIST OF TABLES

LIST OF FIGURES

LIST OF ABBREVIATIONS

AV	artificial viscosity
CEI	constrained entropy inequality
CFL	Courant-Friedrichs-Lewy condition
CG	continuous galerkin approach
DAE	differential-algebraic equation
DDD	de-aired, deionized, and distilled water
DOF	degree of freedom
EI	entropy inequality
EV	entropy viscosity
FEM	finite element method
IDA	implicit differential-algebraic solver
LED	local extrema diminishing
ODE	ordinary differential equation
PDE	partial differential equation
PISO	pressure-implicit with splitting of operators
REV	representative elementary volume
SAMOL	spatially-adaptive method of lines
SIMPLE	semi-implicit method for pressure-linked equations
SEI	simplified entropy inequality
TCAT	thermodynamically constrained averaging theory

LIST OF SYMBOLS

Roman Symbols

A	area
A_D	dilute advective operator
A_T	non-dilute advective operator
c_E	TCAT viscosity tuning parameter
$\mathbf{d}$	rate of strain tensor
d	artificial viscosity
d_{50}	mean grain diameter
$\hat{D}$	hydrodynamic dispersion
D_D	dilute dispersive operator
D_T	non-dilute dispersive operator
$\hat{D}_0$	dilute molecular diffusion coefficient
$\hat{D}_{Aw}$	variable molecular diffusion coefficient
$\hat{D}_u^{Aw}$	dispersive closure coefficient related to diffusion velocity
$\hat{D}_v^{Aw}$	dispersive closure coefficient related to momentum transfer
f	flux
F	entropy flux
$F^{\overline{\overline{Aw}}}$	total advective and dispersive flux
Fr	Froude number
F_T	flow operator
$\mathbf{g}$	acceleration vector due to an external force, such as gravity
G	magnitude of gravity vector
$\mathbf{h}$	reference datum
h	grid spacing
H^1	standard Sobolev space
$\mathbf{I}$	identity tensor
I	ionic strength
$I\left(S\right)$	indices of shape functions that are non-zero over a region

$\mathcal{I}_s$	index set of species
J	mass flux
K	transport matrix
$\hat{k}$	intrinsic permeability
ℓ_2	error norm
m	molality
$\dot{m}$	mass flow rate
$\mathcal{M}_h$	computational mesh
m_i	lumped mass matrix
M_{ij}	consistent mass matrix
MW	molecular weight
N_{dof}	number of degrees of freedom
N_g	gravity number
p	fluid pressure
P	non-advective mass flux related to pressure gradient
P^1	first order Lagrange polynomials
Pe	Peclet number
Pe_m	mesh Peclet number
Q	volumetric flow rate
R	entropy residual
Re	Reynolds number
R_G	ideal gas constant
$\hat{R}_u^{Aw}$	advective closure coefficient related to momentum tranfer
$\hat{R}_v^{Aw}$	advective closure coefficients related to deviation velocity
$\hat{R}^p$	closure coefficients related to pressure variations
S	support of a basis function
t	time
$\mathbf{t}$	stress tensor
T	transpose operator
$\overset{ws\to w}{\mathbf{T}}$	momentum transfer from species i to the water phase

u	diffusion velocity
v	velocity
V	partial mass volume
x	mole fraction
X	partial mass volume fraction
z	position defined as positive upwards

Greek Symbols

$\hat{\alpha}_L$	longitudinal dispersivity
$\hat{\beta}$	fitting parameter that accounts for non-dilute behavior
$\hat{\gamma}$	activity
Γ	non-advective mass flux related to activity gradient
Γ_0	inflow boundary
$\epsilon^{\overline{\overline{w}}}$	porosity
η	entropy function
θ	temperature
Λ	entropy production rate density
μ	chemical potential
$\hat{\mu}$	dynamic viscosity
ρ	mass density
$\hat{\tau}$	tortuosity
ϕ	basis function
ψ	acceleration potential (e.g., gravitational potential)
ω	mass fraction of a species in an entity
Ω_z	non-advective mass flux related to mass fraction gradient
Ω	Domain
Ω_w	spatial domain of wetting phase

Subscripts and Superscripts

$*$	non-dimensional variable
0	dilute value
A	species qualifier

b	parameter relating to non-linear Fickian model
B	species qualifier
EV	entropy viscosity approximation
D	non-advective mass flux due to dispersion
D_m	non-advective mass flux due to molecular diffusion
g	Galerkin solution
in	displacing/incoming fluid
L	low order approximation
res	resident fluid
T	parameter relating to TCAT model
w	entity index corresponding to the wetting phase

CHAPTER 1: INTRODUCTION

1.1 Non-Dilute Flow and Transport

The flow and transport of fresh and saline water in porous media play an important role in many natural and engineered environments. Seawater intrusion, or the displacement of fresh groundwater by saline water, can result in the contamination of fresh water supplies that are used for human consumption or to meet agricultural demand (Barlow and Reichard, 2010; Werner et al., 2013). Toxic and radioactive materials are often injected in subsurface rock salt formations as a disposal method (Kolditz et al., 1998; Oldenburg and Pruess, 1995). Brines, or concentrated saline waters, have also been injected into the subsurface as a strategy to prevent migration of dense non-aqueous phase liquids and other toxic chemicals into drinking water supplies (Hill et al., 2001; Miller et al., 2000; Wright et al., 2009).

Recent studies have shown that additional research is required for these applications due to changing environmental conditions and flawed assumptions. For seawater intrusion, climate change and sea level rise will further compound and reduce valuable fresh groundwater reserves (Ketabchi et al., 2016). Rock salts have been shown to not be impermeable to fluid flow, as previously believed, which raises significant concerns for toxic and radioactive waste disposal and the migration of chemicals (Ghanbarzadeh et al., 2015). To address these problems, a mechansitic understanding of the flow and transport of fresh and saline water in porous media is needed.

The interaction of fresh and saline water in porous media is a function of many factors, including the fluid properties (i.e. density, viscosity, chemical activity, pressure and temperature), the pore morphology and topology and operating conditions (Diersch and Kolditz, 2002; Gray and Miller, 2009; Homsy, 1987; Landman et al., 2007b; Sharp, 1984; Simmons et al., 2001; Watson et al., 2002b; Welty and Gelhar, 1991; Wright et al., 2009). Due to the salt species being at a high enough concentration to impact the fluid properties, the interaction of fresh and saline water is also referred to as non-dilute

flow and transport. This term is more general as it includes any chemical species that can affect fluid properties and not just salt.

Non-dilute flow and transport can be viewed as an extension of dilute flow and transport. For a dilute system, the flow and and transport components can be examined independently as the chemical species of concern does not impact the flow. The dilute species will move with the fluid while spreading from higher concentrations to lower concentrations due to molecular diffusion. For non-dilute flow and transport, the flow and transport components cannot be isolated because the species of interest affects the fluid properties and the flow field. The movement of the fluid in porous media is already complex when fluid properties are constant due to the tortuous path caused by pore morphology (Bijeljic et al., 2011). When the fluid properties become functions of the species concentration, fluid flow behavior becomes significantly more complicated and additional physical phenomena need to be considered such as gravity stabilization (Fernandez et al., 2002).

1.2 Non-Dilute Flow and Transport Models

1.2.1 Length Scales

The length scale of a model is one of its defining features and in this work we are concerned with the microscale and the macroscale. At the microscale, the smallest of the two scales considered in this work, the exact pore morphology and topology are known as well as the exact boundaries of each phase present in the system (Gray and Miller, 2014). For most practical porous media applications, exact microscale information is unknown. At the macroscale, the phase boundaries are no longer known and a macroscale point is represented by the average microscale conditions among all entities. The averaging region used to determine macroscale variables needs to be sufficiently large such that the average is well-defined and insensitive to small changes in the size of the region. This is known as a representative elementary volume (REV) (Bear, 2012).

1.2.2 Existing Models

The traditional approach for formulating macroscale non-dilute flow and transport models is to ignore the microscale, where we have a better understanding of system behavior, and apply conservation of mass and momentum equations directly at the macroscale (Bear, 2012; Simmons et al., 2001).

Empirical relations are then posed to have a closed system. As an example, many researchers have used the macroscale dilute flow and transport model to simulate non-dilute behavior by forcing the dispersivity parameter to agree with laboratory data (Boufadel et al., 1999; Frolkovic and Schepper, 2000; Ibaraki, 1998). Dispersivity is a measure of how a chemical species spreads due to variations of the microscale velocities but is only a property of the porous medium and not a function of the fluid properties. Rather than deriving a model from a mechanistic understanding of non-dilute behavior, macroscale parameters are forced to describe the empirical evidence thus severely limiting the applicability and predictive capabilities of the model (Jiao and Hötzl, 2004; Konz et al., 2009; Landman et al., 2007a,b; Starr and Parlange, 1976; Watson et al., 2002c).

More formal attempts at developing macroscale models for non-dilute flow and transport in porous media have been unable to provide a mechanistic description of non-dilute behavior and are not developed with a sound fundamental basis (Demidov, 2006; Hassanizadeh and Leijnse, 1995; Landman et al., 2007b). The most popular approach is by Hassanizadeh and Leijnse (1995) that combined averaged microscale conservation laws but used macroscale thermodynamics. While models should obey all conservation and thermodynamic laws, the thermodynamic equations should use microscale thermodynamic equations to have consistency across all spatial scales (Gray et al., 2013). To account for the complex non-dilute microscale behavior, a fitting parameter was introduced that is not explicitly related to any physical phenomena. While the model was able to adequately simulate non-dilute laboratory experiments, the usefulness and applicability of the model is reduced as the dependencies and physical phenomena that the fitting parameter represent are unknown (Watson et al., 2002c). There is a need for a macroscale model of non-dilute flow and transport in porous media that begins with a mechanistic understanding of microscale behavior, is developed on a sound fundamental basis and includes, if necessary, parameters that are applicable to a wide range of chemical species and porous media systems.

1.2.3 Thermodynamically Constrained Averaging Theory

The thermodynamically constrained averaging theory (TCAT) is an approach to formulate mathematical models that couples conservation laws and the laws of thermodynamics (Gray and Miller, 2005, 2014). All conservation and thermodynamic equations, and variables are first written at the microscale. A formal averaging approach is then used to upscale the microscale equations and variables

to the desired scale. As is often the case, the number of equations is less than the number of unknowns and additional relations are required to obtain a closed model. With TCAT, an entropy inequality is formed to guide the development of the closure relations such that the posited relations must obey the second law of thermodynamics. Evolution equations can be derived from the averaging theorems to account for larger scale geometric quantities that also need closure. The combination of the conservation equations, state equations, entropy-based closure relations, and evolution equations compose a closed, parameterized model.

The TCAT approach ensures that all physical and thermodynamic laws are obeyed. The models are formulated for the most complex scenario and then assumptions are made. This ensures that all assumptions are explicit and that the resulting models reduce to their simpler versions. For example, as the concentration of a species approaches the dilute limit, the non-dilute model should be able to accurately model dilute behavior. As model formulation begins at the microscale, all larger scale equations and variables are written in terms of microscale averages and therefore all variables are well-defined. The sum of these features is unique to TCAT.

Gray and Miller (2009) developed a closed macroscale model for non-dilute flow and transport using TCAT. This model includes all of the features described above and includes physics ignored by other models including dissipative terms related to gradients in activity and pressure. A simulator for this model has not been implemented. Additionally, the relations posited to close the model have not been evaluated and only relate terms through closure coefficients. Parameterization of the closure coefficients is still needed and should be based on a mechanistic understanding of non-dilute behavior.

1.3 Subscale Modeling

As mentioned, one of the features of the TCAT approach is that all variables are written in terms of microscale averages. While an improved model is needed for non-dilute flow and transport at the macroscale, microscale simulations can be preformed to gain a mechanistic understanding of macroscale behavior by averaging the microscale results. The governing equations that describe microscale behavior are better understood and high-fidelity simulators already exist (Weller et al., 1998). The use of smaller scale simulations to validate large scale models, parameterize unknown closure coefficients, and assess macroscale assumptions is known as subscale modeling.

Subscale modeling also allows for simulations where specific behavior can be isolated. For example, if we wanted to examine the effects that density has on non-dilute flow and transport but ignore other aspects such as activity and viscosity, we could simply force the activity and viscosity to be constant in the simulations. This is difficult in a laboratory setting as we are constrained to the combined properties of the species selected for the experiments.

Microscale non-dilute flow and transport simulations have been limited to the membrane literature where no porous media is present (Gruber et al., 2011, 2016). Dilute flow and transport in porous media has been studied extensively (Aramideh et al., 2018; Bijeljic et al., 2011, 2004, 2013; Icardi et al., 2014). Using subscale modeling as a tool to improve TCAT models has seen success for two-fluid-phase flow in porous media where closure coefficients have been parameterized, improved state equations have been developed, and enhanced understanding of microscale and macroscale physics has been provided (Bruning and Miller, 2019; Dye et al., 2016; McClure et al., 2017).

1.4 Numerical Methods for Non-Dilute Flow and Transport Problems

Obtaining an accurate solution to the existing macroscale models for non-dilute flow and transport is nontrivial (Landman et al., 2007a). The class of problems that include non-dilute flow and transport are known as sharp front problems and the defining feature is an advective term that is large as compared to the dispersive term, if present at all (Farthing and Miller, 2000; Smith et al., 1991; Widdowson et al., 1988). The characteristic of sharp front problems is a near instantaneous transition of the solution variable in space. Low-order numerical methods for sharp front problems will produce a solution free of non-physical oscillations but to obtain an accurate solution, a large number of degrees of freedom are needed to adequately resolve the front (LeVeque, 2002). A large number of degrees of freedom increases the computational cost and for many problems this may not be an option due to computational constraints and higher order numerical methods are needed. According to Godunov's theorem, only nonlinear higher-order methods and linear first-order methods can provide non-oscillatory solutions (Godunov, 1959).

The literature is rife with nonlinear higher-order methods for sharp front problems however low-order approximations have typically been used for solving non-dilute flow and transport models (Guermond and Popov, 2017; Hassanizadeh and Leijnse, 1995; Johannsen et al., 2002; Landman et al.,

2007b; LeVeque, 2002; Miller et al., 2013; Watson et al., 2002c). Many of the nonlinear higher-order methods are not ideal for irregularly shaped domains, which commonly occur in non-dilute flow and transport applications (Miller et al., 2016). Methods where an irregularly shaped domain can easily be incorporated, such as finite element methods (FEM), are not as mature for sharp front problems (Guermond and Popov, 2017; Kuzmin, 2006).

One class of FEM approaches is based on introducing artificial viscosity (or diffusion) into the solution to remove non-physical oscillations (Harten et al., 1976, 1997; Lax, 1971; LeVeque, 1992; Osher and Chakravarthy, 1984; Smoller, 1994). The difficulty with this method is determining the optimal amount of artificial viscosity to introduce; if too little artificial viscosity is included, the solution will oscillate, if too much artificial viscosity is added, the solution will be smeared. The optimal amount of viscosity to add is not known *a priori*. One approach for determining the amount of artificial viscosity to include is the entropy viscosity method (EV) that scales the amount of artificial viscosity based on a measure of the mathematical entropy, which is not inherently related to the thermodynamic entropy (Guermond and Nazarov, 2014; Guermond et al., 2010, 2017, 2014, 2011; Guermond and Popov, 2014, 2017). There is no rigorous definition of the optimal entropy function and the choice is problem dependent.

As discussed, an entropy production rate is derived when developing a TCAT model to guide model closure. Pairing the TCAT entropy production rate with the EV method, where a measure of entropy is needed, may produce an efficient solution scheme. This could potentially improve the numerical methods used for solving non-dilute flow and transport problems by using the known physics to improve the numerics. This method can easily incorporate irregular boundaries and potentially reduce the high computational cost associated with solving non-dilute flow and transport models.

1.5 Research Objectives

The research presented herein is focused on advancing the fundamental understanding of non-dilute flow and transport in porous media. This includes inspecting the physical phenomena that occur and improving numerical methods used to solve non-dilute flow and transport models. The specific objectives for this research are as follows:

- to develop and solve a parameterized macroscale model to describe non-dilute flow and transport in porous media using the thermodynamically constrained averaging theory (Chapter 2);
- to improve the numerical methods used to solve the newly developed macroscale model for non-dilute flow and transport in porous media by using the physics to improve the numerical methods (Chapter 3); and
- to advance fundamental mechanistic understanding of non-dilute transport in porous media using a microscale approach (Chapter 4).

CHAPTER 2: MODELING NON-DILUTE SPECIES TRANSPORT USING THE THERMODYNAMICALLY CONSTRAINED AVERAGING THEORY

2.1 Introduction

The use of models to describe the flow and transport of non-dilute systems and fresh water is commonplace. Applications include seawater intrusion in coastal aquifers, dense non-aqueous phase liquid remediation and management, and underground injection of hazardous materials (Hill et al., 2001; Kolditz et al., 1998; Miller et al., 2000; Werner et al., 2013; Wright et al., 2009). While existing uses for non-dilute flow and transport models will remain, newer applications are emerging, such as assessing the impacts that climate change and sea level rise will have on fresh water reserves and exploring approaches to mitigate climate change (Ketabchi et al., 2016).

The classical approach for modeling mass transport in porous media for a dilute species involves the use of conservation of mass equations for the fluid and species of interest, Darcy's law as an approximate conservation of momentum of the fluid, and Fick's law to represent deviations from the mean flow for the species (Bear, 1979). The form of the dispersion tensor used with Fick's law consists of a term related to molecular diffusion and a term that is a function of the Darcy velocity weighted by a longitudinal and transverse dispersivity. The dispersivity coefficients are solely functions of the porous medium and not a function of the fluid properties. For non-dilute systems, the density and viscosity are functions of the fluid composition, which affects species transport. Therefore, it is understood that the standard Fickian dilute model cannot be applied to non-dilute systems, even for restrictive laboratory cases of a homogeneous isotropic porous media in a system well above the representative elementary volume (REV) scale which is needed for Fickian transport to be a reasonable approximation of reality.

Experimental and theoretical work on gravitationally stable, non-dilute displacements in porous media has demonstrated that the observed dispersion is dependent on fluid properties (Anderson, 1997; Brigham et al., 1961; Hassanizadeh and Leijnse, 1995; Slobod, 1964; Welty and Gelhar, 1991). While Darcy's Law has been found to be applicable for approximating the momentum equation for

the fluid phase in these systems, Fick's law has been shown to be inadequate for describing deviations from mean transport for a non-dilute species (Konz et al., 2009; Starr and Parlange, 1976; Watson et al., 2002b; Wright et al., 2009). Dispersion in non-dilute systems has been found to depend on the density gradients, viscosity gradients, and mean flow rate, in addition to properties of the porous media (Broeke and Krishna, 1995; Jiao and Hötzl, 2004; Konz et al., 2009; Landman et al., 2007a,b; Noordman and Wesselingh, 2002; Starr and Parlange, 1976; Watson et al., 2002c). Due to gravity stabilization, the dispersion is reduced for larger density gradient displacements compared to the dilute transport case, and the density gradient has been shown to be the dominant factor in comparison to the viscosity gradient for systems evaluated to date (Landman et al., 2007a). The effects of chemical activity on non-dilute flow and transport have not been reported in the literature.

While some have applied the standard Fickian dilute model to non-dilute systems despite the inherent issues and shortcomings, others have attempted to develop new models to describe non-dilute species transport (Gray and Miller, 2009, 2014; Hassanizadeh, 1990, 1996; Hassanizadeh and Leijnse, 1995; Landman et al., 2007b). A variety of physical mechanisms can affect the observed behavior of non-dilute systems. Therefore, any new model requires significant validation by comparison to experimental data. Ideally, a model should functionally represent the observed data when parameter estimation is performed and successfully predict species transport in systems for which all parameters have been estimated independently. The wider the variety of conditions a model is exposed to, the more confidence one can have in the usefulness of the model. With these guiding principles in mind, non-dilute species transport models have been developed and evaluated with respect to the operative mechanisms.

The nonlinear Fickian model developed by Hassanizadeh and Leijnse (1995) is based on the theory of rational thermodynamics and is a macroscale model, which is the scale at which a point is represented by the average conditions among all phases (Hassanizadeh, 1986). In this model, the standard Fickian dispersion model is expanded by a Taylor series to include a new parameter to account for non-ideal dispersion (Hassanizadeh, 1986; Hassanizadeh and Leijnse, 1995). Chemical potential is used in the formulation of the model, however, an assumption is made that the chemical potential is only a function of the mass fraction of the salt. The nonlinear Fickian model has been applied to laboratory experiments (Hassanizadeh and Leijnse, 1995; Nick et al., 2009; Schotting et al., 1999; Watson et al., 2002c) as well as a set of numerical data (Landman et al., 2007b). All of the laboratory

experiments used NaCl as the non-dilute species. Multiple flow rates and coarse and medium grain sands were examined as well as different flow regimes including constant head and constant flow rate experiments. The optimized parameter in the nonlinear expansion has been found to be sensitive to the difference between the displacing and displaced fluid densities and has been shown to be a function of the velocity of the fluid, where the log of the parameter varies linearly with the log of the Darcy velocity (Landman et al., 2007b; Watson et al., 2002c).

The model of Demidov (2006) was formulated from the microscale, where the boundaries of all phases are resolved in space and in time, and homogenization was applied to derive a macroscale model. This approach requires knowledge of the characteristic pore morphology and topology and a parameterization of the flow field at the microscale. The model neglects viscosity and activity impacts at both scales. This model has only been applied to one set of numerically generated data (Landman et al., 2007b). Landman et al. (2007b) used the characteristic pore size parameter that appears in the model as a fitting parameter to allow for comparison to the numerically generated data, and an empirical relationship was used to represent the microscale flow fluid. An accurate fit for two types of porous media and various flow rates was obtained, however the fitting parameter depended upon system conditions.

The homogenization model of Egorov (Landman et al., 2007b) was formulated at the mesoscale, which is a scale above the macroscale used to account for heterogeneity at the macroscale. This model assumes that the dilute flow and transport model is an accurate model at the macroscale for non-dilute systems, which has been shown to be false (Anderson, 1997; Brigham et al., 1961; Hassanizadeh and Leijnse, 1995; Slobod, 1964; Welty and Gelhar, 1991). The macroscale permeability distribution field must be known and homogenization was used to derive a mesoscale model. This model neglects viscosity and activity effects at both scales. As with the homogenization model of Demidov (2006), this model has only been applied to a numerically generated set of data (Landman et al., 2007b) and success of the model was limited.

In addition to the three models described above, a model has been derived based on the thermodynamically constrained averaging theory (TCAT) (Gray and Miller, 2009). This approach poses all equations at the microscale and uses formal averaging approaches to derive the model at the scale of interest. The fluid and solid phases are considered, as well as the interface between the two. Microscale thermodynamic relations, based on classical irreversible thermodynamics, are also averaged

and an entropy inequality is formulated, through the use of Lagrange multipliers, to provide permissibility conditions for closure relations. An entity-based momentum equation, as well as a species-based momentum equation, model was derived (Gray and Miller, 2009). The TCAT model includes dispersion associated with activity and pressure gradients. This model has not yet been solved or compared to experimental data.

Currently, a mature level of understanding for modeling non-dilute transport has not yet been achieved. Only limited experimental data is available and all models posed to date have some combination of limited evaluation and validation or certain limitations in describing non-dilute systems mechanistically. Opportunities exist to advance understanding of non-dilute transport using both experimental methods that investigate a broader range of physical conditions than have been considered and alternative approaches for mechanistic modeling of these challenging systems.

The overall goal of this work is to improve the understanding of the behavior of non-dilute species transport in porous medium systems. The specific objectives of this work are: (1) to observe systems with a wide range of variability in fluid density, viscosity, and chemical activity of the reference species; (2) to advance a multiscale model formulation approach for describing such systems; (3) to develop efficient numerical approximation methods for the formulated model; (4) to compare experimental observations with the formulated model description in both an explanatory and predictive sense; and (5) to assess the importance of previously neglected phenomena, including species transport due to variations in chemical activity.

2.2 Experimental Materials and Methods

The purpose of the experimental work was to investigate non-dilute transport for systems that have not been studied to date to build the universe of data available for model evaluation and validation. As such, the intent was to investigate systems with a relatively large range in density, viscosity, and chemical activities in order to provide a challenging set of conditions to model. The materials and methods used to collect this experimental data are detailed in the sections that follow.

2.2.1 Materials

The materials used for this work included a uniform sand for the porous medium, water as a solvent, a radioactive tracer, and a non-dilute solute. A 12/20 Accusand was used for the porous medium, which is a uniform quartz sand with a reported mean particle diameter of 1.105 mm (σ = 0.014 mm), uniformity coefficient of 1.231 (σ = 0.043), and a saturated hydraulic conductivity of 30.19 cm/min (σ =1.00 cm/min) (Schroth et al., 1996). De-aired, deionized, and distilled (DDD) water was used for all experiments and dilutions. Tritium was used as a conservative tracer, and calcium bromide ($CaBr_2$) was the non-dilute solute (Dead Sea Bromine Group).

2.2.2 Measurement Methods

The measurements involved in this work included fluid density, fluid viscosity, and the concentration of the radioactive tracer. The methods used to make these measurements are described in turn.

Density was measured using a density meter (Anton Paar DMA 48), where measurements are typically $\pm$0.0001 g/mL. The instrument was calibrated using air (0.0012 g/ml at 25°C) and DDD water (0.9970 g/ml at 25°C). The density of the saturated brine was monitored through the course of this work and determined to be 1.7039 g/ml.

For determining the density of the solution as a function of the $CaBr_2$ mass fraction, a series of solutions were made to characterize density across the mass fractions of interest. Specifically, 30 solutions were analyzed, including pure water. Solutions of brine and water were made by combining volumetric ratios of saturated brine to DDD water starting at 3.33% brine (i.e., 1 part brine to 14 parts water), increasing the ratio of brine of 3.33% (i.e., 2:13, 3:12, 4:11, etc.), and ending with 100% brine (15:0). To ensure the solutions were mixed properly, the mass of each component was also measured and compared with the expected mass, given the known density of both water and brine. Solutions were allowed to equilibrate overnight prior to measuring. The glass tube in the density meter was rinsed several times with water and ethanol, dried with air, and equilibrated back to the known density of air between each measurement.

For the column experiments, the density meter was placed in-line with the column effluent to provide continuous measurements of density. The read-out from the density meter was recorded every 30 seconds using a time-lapsed camera.

Viscosity measurements were used to develop an equation of state between viscosity and $CaBr_2$ mass fraction at 25°C. Viscosity was measured using a falling ball viscometer (Haake Model B). To verify the measurements, results from the viscometer were compared to standards that spanned the range of the unknowns. The measured viscosity for water was compared to a value from the literature (0.890 mPa·s at 25°C). The error in the measurement was less than 5%. Similarly, the viscosity was measured for a commercial viscosity standard much higher than that of water (Cannon Instrument Company, General Purpose Viscosity Standard N10, 15.79 mPa·s 25°C). The error in the measurement was 11%.

A series of solutions were made to characterize viscosity across the $CaBr_2$ mass fractions of interest. Specifically, 10 solutions were made by combining volumetric ratios of brine to DDD water starting at 10% brine (i.e., 1 part brine to 9 parts water), increasing in 10% increments, and ending with 100% brine. Solutions were allowed to equilibrate overnight prior to measuring. Viscosity measurements were made by first adding each solution to the falling ball apparatus. Next, one of the calibrated balls was dropped through the fluid and the amount of time to travel the length of the apparatus was measured and used to calculate an estimate of the viscosity. A minimum of three measurements were made for each solution. An average of these measurements was used when fitting the data for the equation of state.

To measure the concentration of the radioactive tracer, samples were collected in plastic scintillation vials and samples were mixed with Fisher 30% scintillation cocktail. A Packard 1900TR scintillation counter measured the disintegrations per minute (DPM) for two minutes for the different samples and the results were averaged. These results were then converted to have units of mCi.

2.2.3 Displacement Experiment Methods

A set of stable brine displacement experiments were performed in a column packed with homogeneous porous media. A cylindrical glass column, 90 cm in length and 2.5 cm in diameter was used. Fluids were pumped through the column using syringe pumps (Harvard Apparatus) equipped with glass, air-tight syringes (Hamilton Model 1100). The Darcy velocity for all experiments was 5 m/day.

The column was dry-packed with the 12/20 Accusand. The dry-packed columns were vibrated and purged with gaseous CO_2. Column A was packed to a length of 88.9 cm and Column B to a length of 88.0 cm. We differentiate between the two columns as we had to repack the column and the lengths

of the columns changed and potentially the pore morphology and topology. The porosity for both columns was 0.33, which was determined by weighing the mass of sand added to the column and using the density of the sand (2.65 g/cm^3). To calculate the tortuosity ($\hat{\tau}$) for each column, the relation for a random homogeneous isotropic sphere packing was used, which is dependent on the porosity, and was calculated to be 1.33 for both columns (Shen and Chen, 2007).

For the tracer displacement experiments, 2-mL aliquots from the effluent were collected in 10-mL plastic scintillation vials. The experiment continued until at least 1.75 pore volumes had passed through column. The results from the end of the column were normalized by dividing by the radioactivity of the incoming fluid.

For the brine displacement experiments, the resident fluid was displaced with a fluid of greater density, such that all displacements were always density stable (i.e., $\rho_d^w > \rho_r^w$, where ρ^w is the density of the fluid, and the subscripts d and r refer to the displacing fluid density and resident fluid density, respectively). Two types of experiments were conducted: (1) a series where the resident fluid in the column was pure water and and the concentration of the $CaBr_2$ in the displacing fluid was varied; and (2) a series where both the resident and displacing fluid $CaBr_2$ concentrations were varied to result in a constant density difference between the two fluids. This second sequence of experiments had variations in viscosity and chemical activity for each pair of resident and displacing mass fractions to provide a means to examine the importance of changes in these variables. Both types of experiments were conducted in Column A and the second type of experiment was repeated in Column B as the column needed to be repacked midway through the replicates for the second type of experiment.

2.3 Model Formulations

The experimental data was designed to be macroscopically one-dimensional in space and the models used to simulate this data were similarly one-dimensional. Since the conditions examined are intentionally homogeneous and isotropic, and the systems are well above the REV limit, parameter variation due to changes in material properties and non-local effects was not considered. The focus was thus on evaluating the ability of models to describe non-dilute transport under stable displacements in homogeneous systems.

The nomenclature for all variables follows the TCAT convention (Gray and Miller, 2014). A superscript on a variable refers to an intrinsic average of a microscale variable to produce a macroscale variable. A single overbar on the superscript means that the term is a density weighted average of a microscale variable, and a double overbar is a unique average, which is defined. Terms with carats are coefficients that may be determined from experimental data using parameter estimation. Three models are considered: the standard Fickian model, a nonlinear Fickian model, and a TCAT model for non-dilute systems, which are summarized in turn in the sections that follow.

2.3.1 Fickian Model

The classical single-fluid-phase flow and Fickian dilute species transport model for a homogeneous, isotropic porous media has been used to describe non-dilute flow and transport by allowing the density and viscosity of the fluid phase to vary as functions of the species concentration (e.g. Steefel et al., 2015; Voss, 1984; Wright et al., 2009). This model is composed of a conservation of mass equation for the water phase

$$\frac{\partial\left(\epsilon^{\overline{\overline{w}}}\rho^{w}\right)}{\partial t}=-\frac{\partial}{\partial z}\left(\epsilon^{\overline{\overline{w}}}\rho^{w}v^{\overline{w}}\right)\ , \tag{2.1}$$

and a conservation of mass equation for the solute species

$$\frac{\partial\left(\epsilon^{\overline{\overline{w}}}\rho^{w}\omega^{A\overline{w}}\right)}{\partial t}=-\frac{\partial}{\partial z}\left(\epsilon^{\overline{\overline{w}}}\rho^{w}\omega^{A\overline{w}}v^{\overline{w}}\right)-\frac{\partial}{\partial z}\left(\epsilon^{\overline{\overline{w}}}\rho^{w}\omega^{A\overline{w}}u^{\overline{\overline{Aw}}}\right)\ , \tag{2.2}$$

where z is positive upwards, $\epsilon^{\overline{\overline{w}}}$ is the porosity, ρ^{w} is the density of the water phase, $v^{\overline{w}}$ is the velocity of the water phase, $\omega^{A\overline{w}}$ is the mass fraction of solute species A, and $u^{\overline{\overline{Aw}}}$ is the deviation velocity from the mean for species A. Darcy's law is used to solve for the velocity of the fluid phase

$$\epsilon^{\overline{\overline{w}}}v^{\overline{w}}=-\frac{\hat{k}}{\hat{\mu}}\left(\frac{\partial p^{w}}{\partial z}+\rho^{w}g^{\overline{w}}\right)\ , \tag{2.3}$$

where $\hat{k}$ is the intrinsic permeability, $\hat{\mu}$ is the viscosity of the water, p^{w} is the pressure of the water phase, and $g^{\overline{w}}$ is the gravitational acceleration.

A Fickian approximation for the mass flux resulting from the deviation velocity can be written as (Bear, 1979)

$$J^{\overline{\overline{Aw}}} = \epsilon^{\overline{\overline{w}}} \rho^w \omega^{A\overline{w}} u^{\overline{\overline{Aw}}} = -\epsilon^{\overline{\overline{w}}} \rho^w \hat{D} \frac{\partial \omega^{A\overline{w}}}{\partial z} \,, \tag{2.4}$$

where $J^{\overline{\overline{Aw}}}$ is defined as the mass flux of species A and $\hat{D}$ is the hydrodynamic dispersion for porous media systems. The hydrodynamic dispersion consists of a term related to molecular diffusion and a term that approximates variations in the microscale velocity. The most commonly used form in one dimension is

$$\hat{D} = \frac{\hat{D}_{Aw}}{\hat{\tau}} + \hat{\alpha}_L v^{\overline{w}} \,, \tag{2.5}$$

where $\hat{\tau}$ is the tortuosity of the porous medium, which is defined as the actual distance traveled by a species over a unit length of the medium and is greater than or equal to one, $\hat{D}_{Aw}$ is the molecular diffusion coefficient, and $\hat{\alpha}_L$ is the longitudinal dispersivity (Bear, 1979).

2.3.2 Nonlinear Fickian Model

The nonlinear Fickian model approximates the dependency of the dispersion on fluid properties. A series expansion of Fickian model yields

$$\left(1 + \hat{\beta} \left| J^{\overline{\overline{Aw}}} \right| \right) J^{\overline{\overline{Aw}}} = -\epsilon^{\overline{\overline{w}}} \rho^w \hat{D} \frac{\partial \omega^{A\overline{w}}}{\partial z} \,, \tag{2.6}$$

where $\hat{\beta}$ is a parameter and $\hat{D}$ is defined in Eqn (4.103). The nonlinear Fickian model was derived using rational thermodynamics (Hassanizadeh, 1986; Hassanizadeh and Leijnse, 1995), and it is assumed that the chemical potential is solely a function of the mass fraction of the species.

An alternative nonlinear Fickian model can also be written in the following form

$$J^{\overline{\overline{Aw}}} = -\epsilon^{\overline{\overline{w}}} \rho^w \left(\frac{\hat{D}_{Aw}}{\hat{\tau}} + \hat{\alpha}_L^B v^{\overline{w}} \right) \frac{\partial \omega^{A\overline{w}}}{\partial z} \,, \tag{2.7}$$

where

$$\hat{\alpha}_L^B = \frac{2\hat{\alpha}_L}{1 + \sqrt{1 - 4\hat{\beta}\epsilon^{\overline{\overline{w}}} \rho^w \hat{\alpha}_L v^{\overline{w}} \frac{\partial \omega^{A\overline{w}}}{\partial z}}} \,. \tag{2.8}$$

Eqns (2.7) and (2.8) result from assuming that only the mechanical dispersion component of Eqn (2.6) is nonlinear in the dispersive flux and that the molecular diffusion component does not depend upon $J^{\overline{\overline{Aw}}}$, although $\hat{D}_m$ may depend upon other solution variables.

2.3.3 Thermodynamically Constrained Averaging Theory Model

TCAT is a method for formulating models that provides a firm connection between the microscale, or pore scale, and the macroscale for conservation equations as well as thermodynamics (Gray and Miller, 2005, 2014; Miller and Gray, 2005). A formal averaging approach is used to upscale the microscale conservation and thermodynamic equations to the scale of interest. To solve the closure problem, the conservation equations and thermodynamic relations are combined in an entropy inequality. Explicit, formally-stated approximations are used to simplify the entropy inequality to a strict flux-force form. Closure relations are then posited, constrained by a requirement of consistency with the simplified entropy inequality (SEI), and a closed model results. Parameters in the closure relations can be determined with macroscale data using a parameter estimation approach such as nonlinear regression. Alternatively, due to the connection between all spatial scales, subscale or microscale modeling can be performed to determine the parameters in the closure relations (Gray et al., 2015; Miller et al., 2018b).

TCAT differentiates between primary restrictions, SEI approximations, and secondary restrictions (Gray and Miller, 2014). Primary restrictions specify the thermodynamic theory to be used, the system and scale to be considered, and the physical phenomena to be considered. For this problem, classical irreversible thermodynamics is used to describe both equilibrium and near-equilibrium states. The system of interest consists of a wetting phase, a relatively immobile solid phase, and an interface between the wetting and solid phase. The properties of the wetting phase are dependent on species composition. The scale of the system of interest is the macroscale and system length scales are well separated. The macroscale is defined at a scale that is consistent with the size of the REV (Gray and Miller, 2009). Additionally, the physical phenomena to be considered are the transport of mass, momentum, and energy for each phase and the interface.

From the primary restrictions, an exact constrained entropy inequality (CEI) is derived. Assumptions are made to the CEI so that all terms are in a strict macroscale force-flux form so that closure relations can be posited. The SEI approximations are based on mathematical approximations. Exam-

ples of the approximations made for this system include breaking of average quantities and elimination of terms that are expected to be small Gray and Miller (2009). Secondary restrictions are based on the specific system of interest. In this work, the following assumptions are made: the system is isothermal, the interface between the wetting phase and the solid can be neglected, the wetting phase consists of a species A fully dissolved in a solvent B, no reactions occur, no diffusion of the species into the solid phase, and the porous media is isotropic.

Miller and Gray (2008) and Gray and Miller (2009) have derived two different TCAT models for non-dilute species transport. One form uses a phase-based conservation of momentum equation, while the other uses a species-based conservation of momentum equation. Both of these models have features that are lacking in other attempts to describe non-dilute flow and species transport including gradients related to the pressure and activity that appear in the species conservation of mass equation. As with all TCAT models, the macroscale variables in these models are expressed explicitly in terms of specific averages of microscale quantities making a firm connection between the pore scale and the macroscale.

The phase-based momentum equation TCAT model for non-dilute species transport from Gray and Miller (2009) was extended in this work to include a cross-coupled closure. This formulation is detailed in the appendix, and the final model formulation is summarized as follows.

The simplified conservation of momentum equation for the fluid is

$$\begin{aligned}\hat{R}_v^{Aw} v^{\overline{w}} = &-\epsilon^{\overline{\overline{w}}} \frac{\partial p^w}{\partial z} - \epsilon^{\overline{\overline{w}}} \rho^w g^{\overline{w}} - R_G \theta^{\overline{\overline{w}}} \left(\frac{MW_W^3}{MW_A^2 MW_B^2} \right) \hat{D}_v^{Aw} \frac{\partial \omega^{A\overline{w}}}{\partial z} \\ &- R_G \theta^{\overline{\overline{w}}} \left(\frac{x^{\overline{\overline{Aw}}}}{\hat{\gamma}^{\overline{\overline{Aw}}}} \right) \left(\frac{MW_W}{MW_A MW_B} \right) \hat{D}_v^{Aw} \frac{\partial \hat{\gamma}^{\overline{\overline{Aw}}}}{\partial z} \\ &- \omega^{A\overline{w}} \left(\rho^w V^{\overline{\overline{Aw}}} - 1 \right) \left(\frac{MW_W^2}{MW_A MW_B} \right) \hat{D}_v^{Aw} \frac{\partial p^w}{\partial z} \ , \end{aligned} \tag{2.9}$$

where species A is defined as the salt and species B is the water, $\hat{R}_v^{Aw}$ and $\hat{D}_v^{Aw}$ are closure coefficients that need to be parameterized, R_G is the universal gas constant, $\theta^{\overline{\overline{w}}}$ is the temperature, MW_A and MW_B are the molecular weights of species A and B, MW_W is the molecular weight of the fluid mixture, $x^{\overline{\overline{Aw}}}$ is the mole fraction of species A, $\hat{\gamma}^{\overline{\overline{Aw}}}$ is the activity of species A, and $V^{\overline{\overline{Aw}}}$ is the partial mass volume of species A.

The conservation of mass equation for species A is

$$\begin{aligned}
&\frac{\partial\left(\epsilon^{\overline{\overline{w}}}\rho^{w}\omega^{A\overline{w}}\right)}{\partial t}+\frac{\partial}{\partial z}\left[\epsilon^{\overline{\overline{w}}}\rho^{w}\left(\omega^{A\overline{w}}-\hat{R}_{u}^{Aw}\right)v^{\overline{w}}\right]\\
&\quad-\frac{\partial}{\partial z}\left[\epsilon^{\overline{\overline{w}}}\left(\frac{MW_{W}^{2}}{MW_{A}MW_{B}}\right)\left(\rho^{w}V^{\overline{\overline{Aw}}}-1\right)\omega^{A\overline{w}}\hat{D}_{u}^{Aw}\frac{\partial p^{w}}{\partial z}\right]\\
&\quad-\frac{\partial}{\partial z}\left[\epsilon^{\overline{\overline{w}}}\rho^{w}R_{G}\theta^{\overline{\overline{w}}}\left(\frac{MW_{W}^{3}}{MW_{A}^{2}MW_{B}^{2}}\right)\hat{D}_{u}^{Aw}\frac{\partial\omega^{A\overline{w}}}{\partial z}\right]\\
&\quad-\frac{\partial}{\partial z}\left[\epsilon^{\overline{\overline{w}}}\rho^{w}R_{G}\theta^{\overline{\overline{w}}}\left(\frac{\omega^{A\overline{w}}}{\hat{\gamma}^{\overline{\overline{Aw}}}}\right)\left(\frac{MW_{W}^{2}}{MW_{A}^{2}MW_{B}}\right)\hat{D}_{u}^{Aw}\frac{\partial\hat{\gamma}^{\overline{\overline{Aw}}}}{\partial z}\right]=0\,,
\end{aligned}\tag{2.10}$$

where $\hat{R}_{u}^{Aw}$ and $\hat{D}_{u}^{Aw}$ are non-negative closure coefficients. The conservation of mass equation for the water phase is given in Eqn (2.1).

Preliminary work demonstrated that the cross-coupled terms are not significant for this system, therefore we set $\hat{D}_{v}^{Aw}$ and $\hat{R}_{u}^{Aw}$ to zero. We define $\hat{R}_{v}^{Aw}$ as

$$\hat{R}_{v}^{Aw}=\frac{\epsilon^{\overline{\overline{w}}2}\hat{\mu}}{\hat{k}}\tag{2.11}$$

so that Eqn (2.9) becomes Darcy's law, which has been shown to be valid for non-dilute systems (Watson et al., 2002b).

The remaining issue deals with the parameterization of $\hat{D}_{u}^{Aw}$. In addition to satisfying the entropy inequality constraint, the posited model should also reduce to the standard Fickian model for dilute systems in the limit of a small mass fraction for the solute species, and to an established form for non-dilute diffusion in the absence of advective transport. We posit a form that meets these criteria, which resulted from the examination of many potential forms.

For the remaining parameter in the conservation of mass equation for the species, we pose the following form

$$\hat{D}_{u}^{Aw}=\left(\frac{MW_{A}^{2}MW_{B}^{2}}{MW_{W}^{3}R_{G}\theta^{\overline{\overline{w}}}}\right)\left(\frac{\hat{D}_{Aw}}{\hat{\tau}}+\hat{\alpha}_{L}^{T}v^{\overline{w}}\right)\,,\tag{2.12}$$

where

$$\hat{\alpha}_{L}^{T}=\frac{2\hat{\alpha}_{L}}{1+\sqrt{1-\hat{\beta}_{1}^{T}\epsilon^{\overline{\overline{w}}}\rho^{w}\hat{\alpha}_{L}v^{\overline{w}}\frac{\partial\omega^{A\overline{w}}}{\partial z}-\hat{\beta}_{2}^{T}\epsilon^{\overline{\overline{w}}}\rho^{w}\frac{\omega^{A\overline{w}}}{\hat{\gamma}^{\overline{\overline{Aw}}}}\frac{MW_{B}}{MW_{W}}\hat{\alpha}_{L}v^{\overline{w}}\frac{\partial\hat{\gamma}^{\overline{\overline{Aw}}}}{\partial z}}}}\,.\tag{2.13}$$

From the SEI, $\hat{D}_u^{Aw}$ must be greater than or equal to zero. For our upward stable displacement experiments, the spatial gradient of the mass fraction is always negative, however, the spatial gradient of the activity, at low mass fractions, is positive. To ensure the SEI is obeyed, we restrict the two parameters $\left(\hat{\beta}_1^T \text{ and } \hat{\beta}_2^T\right)$ to be greater than or equal to zero and we neglect the activity portion of $\hat{\alpha}_L^T$ when the spatial gradient of the activity is positive, which occurs over a relatively small range of small mass fractions of the salt. The two TCAT parameters are fitting parameters that allow the model to vary the amount of dispersion based on chemical composition.

Thus, the conservation of mass equation for a species becomes

$$\begin{aligned}
&\frac{\partial\left(\epsilon^{\overline{\overline{w}}}\rho^w\omega^{A\overline{w}}\right)}{\partial t}+\frac{\partial}{\partial z}\left(\epsilon^{\overline{\overline{w}}}\rho^w\omega^{A\overline{w}}v^{\overline{w}}\right)\\
&\quad-\frac{\partial}{\partial z}\left[\epsilon^{\overline{\overline{w}}}\left(\frac{MW_AMW_B}{MW_WR_G\theta^{\overline{\overline{w}}}}\right)\left(\rho^wV^{\overline{\overline{Aw}}}-1\right)\omega^{A\overline{w}}\left(\frac{\hat{D}_{Aw}}{\hat{\tau}}+\hat{\alpha}_L^Tv^{\overline{w}}\right)\frac{\partial p^w}{\partial z}\right]\\
&\quad-\frac{\partial}{\partial z}\left[\epsilon^{\overline{\overline{w}}}\rho^w\left(\frac{\hat{D}_{Aw}}{\hat{\tau}}+\hat{\alpha}_L^Tv^{\overline{w}}\right)\frac{\partial\omega^{A\overline{w}}}{\partial z}\right]\\
&\quad-\frac{\partial}{\partial z}\left[\epsilon^{\overline{\overline{w}}}\rho^w\left(\frac{\omega^{A\overline{w}}}{\hat{\gamma}^{\overline{\overline{Aw}}}}\right)\left(\frac{MW_B}{MW_W}\right)\left(\frac{\hat{D}_{Aw}}{\hat{\tau}}+\hat{\alpha}_L^Tv^{\overline{w}}\right)\frac{\partial\hat{\gamma}^{\overline{\overline{Aw}}}}{\partial z}\right]=0\ .
\end{aligned}\tag{2.14}$$

For ease of notation, the conservation of mass equation for a species may be rewritten in terms of diffusive and dispersive flux terms related to each spatial gradient

$$\frac{\partial\left(\epsilon^{\overline{\overline{w}}}\rho^w\omega^{A\overline{w}}\right)}{\partial t}+\frac{\partial}{\partial z}\left(\epsilon^{\overline{\overline{w}}}\rho^w\omega^{A\overline{w}}v^{\overline{w}}+P_z^D+P_z^{D_m}+\Omega_z^D+\Omega_z^{D_m}+\Gamma_z^D+\Gamma_z^{D_m}\right)=0\ ,\tag{2.15}$$

where the D superscript refers to a dispersive flux and D_m refers to diffusive flux, and P_z, Ω_z and Γ_z represent the terms associated with the pressure, mass fraction and activity gradient, respectively.

2.3.4 Additional Relations

While commonly neglected or set as a constant in the literature, the diffusion coefficient is known to depend on the properties of the species (Bashar and Tellam, 2011; Bird et al., 2007; Gordon, 1937).

For the diffusion coefficient, we used the following form

$$\hat{D}_{Aw} = \hat{D}_0 \frac{\hat{\mu}_0}{\hat{\mu}} \frac{1}{\rho^w V^{\overline{\overline{Bw}}}} \left[1 + m^{\overline{\overline{Aw}}} \frac{d\left(\ln \hat{\gamma}^{\overline{\overline{Aw}}}\right)}{dm^{\overline{\overline{Aw}}}} \right] , \tag{2.16}$$

where $\hat{D}_0$ is the dilute diffusion coefficient, $V^{\overline{\overline{Bw}}}$ is the partial mass volume of species B, $m^{\overline{\overline{Aw}}}$ is the molality of species A, and $\hat{\mu}_0$ is the viscosity of the pure water (Bashar and Tellam, 2011). This form was used for all three models.

The molecular weight of the fluid is calculated as

$$MW_w = \left(\frac{\omega^{A\overline{w}}}{MW_A} + \frac{\omega^{B\overline{w}}}{MW_B} \right)^{-1} . \tag{2.17}$$

The partial mass volume of species A $\left(V^{\overline{\overline{Aw}}}\right)$ is defined as

$$V^{\overline{\overline{Aw}}} = \frac{1}{\rho^w} + \left(1 - \omega^{A\overline{w}}\right) \frac{\partial}{\partial \omega^{A\overline{w}}} \left(\frac{1}{\rho^w} \right) , \tag{2.18}$$

and the partial mass volume of species B $\left(V^{\overline{\overline{Bw}}}\right)$ is

$$V^{\overline{\overline{Bw}}} = \frac{1}{\rho^w} - \omega^{A\overline{w}} \frac{\partial}{\partial \omega^{A\overline{w}}} \left(\frac{1}{\rho^w} \right) . \tag{2.19}$$

2.4 Model Solution

2.4.1 Model Approximation

The governing equations for the models include a conservation of momentum equation for the water phase, and a conservation of mass equation for the water phase and species A in the water phase. The differences among the three models occur in the conservation of mass equation for species A. The conservation of momentum equation is substituted into the two conservation of mass equations, allowing us to solve for the water phase pressure and mass fraction of the salt as the dependent variables.

The numerical approximation method is formulated using a method of lines approach applied to a system of differential algebraic equations (DAE). To derive the desired form of the equations, we assume that the volume fraction of the water phase is invariant with respect to time and apply the chain

rule to Eqn (2.1) yielding

$$\rho^{w'}\epsilon^{\overline{\overline{w}}}\frac{\partial\omega^{A\overline{w}}}{\partial t} = -\frac{\partial}{\partial z}\left(\epsilon^{\overline{\overline{w}}}\rho^{w}v^{\overline{w}}\right) \ , \tag{2.20}$$

where

$$\rho^{w'} = \frac{\partial\rho^{w}}{\partial\omega^{A\overline{w}}} \ . \tag{2.21}$$

Next, we multiply Eqn (2.15) by $\rho^{w'}$, apply the product rule and the chain rule, and rearrange giving

$$\begin{aligned}\rho^{w'}\epsilon^{\overline{\overline{w}}}\frac{\partial\omega^{A\overline{w}}}{\partial t} = \\ -\frac{\rho^{w'}}{\rho^{w}+\rho^{w'}\omega^{A\overline{w}}}\frac{\partial}{\partial z}\left(\epsilon^{\overline{\overline{w}}}\rho^{w}\omega^{A\overline{w}}v^{\overline{w}} + P_z^D + P_z^{D_m} + \Omega_z^D + \Omega_z^{D_m} + \Gamma_z^D + \Gamma_z^{D_m}\right) \ .\end{aligned} \tag{2.22}$$

Eqn (2.20) is subtracted from Eqn (2.22), which eliminates the temporal derivative term and yields

$$\begin{aligned}\frac{\partial}{\partial z}\left(\epsilon^{\overline{\overline{w}}}\rho^{w}v^{\overline{w}}\right) \\ -\frac{\rho^{w'}}{\rho^{w}+\rho^{w'}\omega^{A\overline{w}}}\frac{\partial}{\partial z}\left(\epsilon^{\overline{\overline{w}}}\rho^{w}\omega^{A\overline{w}}v^{\overline{w}} + P_z^D + P_z^{D_m} + \Omega_z^D + \Omega_z^{D_m} + \Gamma_z^D + \Gamma_z^{D_m}\right) = 0 \ .\end{aligned} \tag{2.23}$$

Upon approximation of the spatial derivatives, Eqns (2.20) and (2.23) are a pair of index-1 DAE. The same procedure is performed for the Fickian and nonlinear Fickian models, with the appropriate species conservation of mass equation.

For the initial conditions, the following relations are used

$$\omega^{A\overline{w}} = \omega_{\text{res}}^{A\overline{w}} \ \text{ in } \Omega,\, t = 0 \ , \tag{2.24}$$

$$p^{w} = \rho_{\text{res}}^{w} g^{\overline{w}}\left(L - z\right) \ \text{ in } \Omega,\, t = 0 \ , \tag{2.25}$$

where $\omega_{\text{res}}^{A\overline{w}}$ is the mass fraction of $CaBr_2$ in the resident fluid and ρ_{res}^{w} is the density of the resident fluid.

The following boundary conditions are used to match the experimental conditions

$$\epsilon^{\overline{\overline{w}}}\rho^{w}v^{\overline{w}} = \frac{Q}{A}\rho_{\text{in}}^{w} \quad \text{at } z = 0, \forall t \ , \tag{2.26}$$

$$\epsilon^{\overline{\overline{w}}}\rho^{w}\omega^{A\overline{w}}v^{\overline{w}} + P_z^D + P_z^{D_m} + \Omega_z^D + \Omega_z^{D_m} + \Gamma_z^D + \Gamma_z^{D_m} = \frac{Q}{A}\rho_{\text{in}}^{w}\omega_{\text{in}}^{A\overline{w}} \quad \text{at } z = 0, \forall t \,, \tag{2.27}$$

$$p^{w} = 0 \quad \text{at } z = L, \forall t \,, \tag{2.28}$$

$$\frac{\partial \omega^{A\overline{w}}}{\partial z} = 0 \text{ at } z = L, \forall t \,, \tag{2.29}$$

where Q is the constant flow rate into the column, A is the cross-sectional area of the column, ρ_{in}^{w} is the density of the displacing fluid and $\omega_{\text{in}}^{A\overline{w}}$ is the mass fraction of the $CaBr_2$ in the displacing fluid.

The method of lines approach is used to decouple the spatial and temporal approximations (Miller et al., 2006). This allows for the use of mature DAE integration methods for time integration. A fixed-leading-coefficient backward difference approximation implemented using variable step-size and variable order methods (up to fifth order) was used (Kees and Miller, 1999, 2002). The implicit differential-algebraic solver (IDA) software package from SUNDIALS (version 2.7) was used for time integration, and both the nonlinear and linear algebraic solvers (Hindmarsh et al., 2005). IDA uses a modified Newton iteration where the Jacobian is typically out-of-date. A banded direct linear solver in IDA was used with LAPACK and BLAS support. The time integration algorithm requires the residual function of the differential algebraic equations to equal zero with the given initial conditions. IDA's built-in function was used to calculate the time derivative of the solution variables to ensure that the residual function is zero at the beginning of the simulation.

For the spatial derivatives, a cell-centered finite difference approximation was used. The cell-centered scheme was preferred over the node-centered method as it allowed for a more natural implementation of the flux boundary conditions (Weiser and Wheeler, 1988). Generally speaking, the front sharpens when the brine concentration increases, therefore, the use of a uniform domain discretization can become costly (Hassanizadeh and Leijnse, 1995; Landman et al., 2007a; Li et al., 2007). For the experiments being examined, a single front exists and that front is the only location that needs to be highly resolved. A spatially-adaptive method of lines algorithm (SAMOL) was adapted from Miller et al. (2006) to adaptively refine the spatial discretization around the location of the front while using a coarser grid away from the front. This algorithm greatly reduced the required number of nodes for a grid-independent solution compared to a fixed-length spatial grid.

2.4.2 Parameter Estimation

To determine the unknown parameters, which include $\hat{\alpha}_L$ for all models, $\hat{\beta}$ for the nonlinear Fickian model, and $\hat{\beta}_1^T$, and $\hat{\beta}_2^T$ for the TCAT model, the ℓ_2 error norm of the difference between model simulation and the experimental data was minimized. A variety of algorithms, constraints on the minimum and maximum values of the parameters, and initial guesses were used to ensure the optimal values, and not local minima, were obtained for the parameters. Algorithms that were used include the Method of Moving asymptotes (Svanberg, 1987), which is a local-gradient based technique, the Constrained Optimization by Linear Approximations method (Powell, 1994), and the DIRECT algorithm which is a global optimization approach (Gablonsky and Kelley, 2001), all of which are built-in to the software package NLopt (version 2.4.2) (Johnson, 2014). All three of the algorithms converged to the same solution.

2.4.3 Computational Environment

All numerical simulations were run on a machine operating with Mac OSX 10.12, equipped with two quad-core 2.5 GHz Intel i7 processors, and 16 GB of RAM. All codes were compiled with g++/gcc version 6.3 with -O3 optimization. All code was implemented in C.

2.5 Results and Discussion

To advance understanding of non-dilute species transport we applied the previously detailed experimental methods and modeling approaches. The subsections that follow detail the experimental work performed, compare the models, and show the importance of various physicochemical transport phenomena.

2.5.1 Equations of State

Equations of state for density and viscosity as a function of the mass fraction of $CaBr_2$ at 25°C were determined experimentally. A least squares fit was used to determine the unknown coefficients. The mass density was fit to the following function

$$\rho^w(\omega) = \rho_0 \left(1 + \rho_1 \omega^{A\overline{w}} + \rho_2 \omega^{A\overline{w}^2} + \rho_3 \omega^{A\overline{w}^3}\right), \tag{2.30}$$

where $\rho_0 = 0.9971$ g/cm^3, $\rho_1 = 0.8414$, $\rho_2 = 0.4827$, and $\rho_3 = 0.8640$.

The following equation of state was fit from experimental data for the dynamic viscosity

$$\hat{\mu}\left(\omega\right) = c_{\hat{\mu}} \exp\left(\hat{\mu}_0 + \hat{\mu}_1 \omega^{A\overline{w}} + \hat{\mu}_2 \omega^{A\overline{w}2} + \hat{\mu}_3 \omega^{A\overline{w}3}\right), \tag{2.31}$$

where $c_{\hat{\mu}} = 0.01$ g/(cm-s), $\hat{\mu}_0 = -0.1165$, $\hat{\mu}_1 = 1.318$, $\hat{\mu}_2 = -2.636$, and $\hat{\mu}_3 = 11.49$.

For the activity coefficient, the following form and coefficients presented by Goldberg and Nuttall (1978) were used

$$\hat{\gamma}^{\overline{\overline{Aw}}} = \exp\left[\frac{\left(\gamma_0 I\right)^{1/2}}{1 + \left(\gamma_1 I\right)^{1/2}} + \gamma_2 m^{\overline{\overline{Aw}}} + \left(\gamma_3 m^{\overline{\overline{Aw}}}\right)^2 + \left(\gamma_4 m^{\overline{\overline{Aw}}}\right)^3 + \left(\gamma_5 m^{\overline{\overline{Aw}}}\right)^4 + \left(\gamma_6 m^{\overline{\overline{Aw}}}\right)^5 + \left(\gamma_7 m^{\overline{\overline{Aw}}}\right)^6\right], \tag{2.32}$$

where $m^{\overline{\overline{Aw}}}$ is the molality of species A and $I = 3m^{\overline{\overline{Aw}}}$ is the ionic strength. The coefficients have the following values with units of kg/mol: $\gamma_0 = 5.52$, $\gamma_1 = 3.20$, $\gamma_2 = 0.324$, $\gamma_3 = 0.456$, $\gamma_4 = -0.384$, $\gamma_5 = 332$, $\gamma_6 = -0.264$, and $\gamma_7 = 0.191$.

The dilute molecular diffusion coefficient $\left(\hat{D}_0\right)$ of tritium in water is 2.23×10^{-5} cm^2/s (Mills, 1973) and 1.05×10^{-5} cm^2/s for $CaBr_2$ in water at 25°C (Bashar and Tellam, 2011). The dilute molecular diffusion coefficient for tritium was used for the dilute tracer experiments.

2.5.2 Displacement Experiments

Two series of column experiments were performed, which are referred to as A and B. The same media was used for both of the columns. We differentiate between the two columns, as column B had to be repacked. Variability of the porosity and tortuosity were not considered in this work. For both columns, dilute tracer experiments, as well as a series of non-dilute species transport experiments, were completed. These are discussed below.

Four dilute tracer experiments were performed. Tracer experiments were the first experiments performed for each column. Partially through the non-dilute displacement experiments, an additional tracer experiment was ran for each column to evaluate the extent to which conditions might have

changed during the set of non-dilute displacement experiments. The dilute tracer experiments were used to determine the longitudinal dispersivity ($\hat{\alpha}_L$) for the columns.

Two different types of non-dilute displacement experiments were conducted. For experimental set 1, pure water was the resident fluid and was displaced by solutions containing varying amounts of $CaBr_2$. With experimental set 2, the mass fraction of $CaBr_2$ in the displacing and displaced fluids was varied so that the density difference between the two fluids was the same for each experiment. Experimental sets 1 and 2 were performed in Column A and only experimental set 2 was run in Column B. Table 2.1 shows the fluid properties of the incoming and resident fluids for the experiments. For the tracer and non-dilute displacement experiments, the minimum percent mass recovered was 99.93%, which is consistent with the accuracy of the density meter. The naming convention for the experiments first specifies which column was used, the experimental set, and finally the experiment number. The mass fraction of the $CaBr_2$ of the displacing fluid increased for each experimental number and T represents a tracer study.

Table 2.1: Experimental conditions for displacement experiments showing the difference in the fluid properties between the displacing and displaced fluids.

ID	$\omega_{\text{res}}^{A\overline{w}}$	$\omega_{\text{in}}^{A\overline{w}}$	$\Delta\rho^w$ (g/cm^3)	$\Delta\hat{\mu}$ (g/cm-s)	$\Delta\hat{\bar{\bar{\gamma}}}^{A\overline{w}}$ (-)	ℓ_2 Error Norm
ColA_11	0	0.0125	0.011	2.2×10^{-4}	-0.43	-
ColA_12	0	0.025	0.021	4.2×10^{-4}	-0.48	1.92×10^{-5}
ColA_13	0	0.05	0.043	8.0×10^{-4}	-0.51	-
ColA_14	0	0.1	0.090	15×10^{-4}	-0.49	3.74×10^{-5}
ColA_15	0	0.2	0.19	29×10^{-4}	-0.31	-
ColA_16	0	0.4	0.47	120×10^{-4}	2.4	2.30×10^{-4}
ColA_21	0	0.15	0.14	21×10^{-4}	-0.43	-
ColA_22	0.27	0.37	0.14	53×10^{-4}	1.38	-
ColA_23	0.37	0.45	0.14	106×10^{-4}	5.33	-
ColA_24	0.45	0.53	0.14	276×10^{-4}	27.23	-
ColB_21	0	0.15	0.14	21×10^{-4}	-0.43	1.00×10^{-6}
ColB_22	0.15	0.27	0.14	24×10^{-4}	0.46	3.77×10^{-7}
ColB_23	0.27	0.37	0.14	53×10^{-4}	1.38	6.17×10^{-7}
ColB_24	0.37	0.45	0.14	106×10^{-4}	5.33	6.12×10^{-7}
ColB_25	0.45	0.53	0.14	276×10^{-4}	27.23	2.14×10^{-7}

For experiments where duplicates were run, the ℓ_2 error norms were calculated and are included in Table 2.1. To determine the error norm, the phase error was first removed between the duplicate experiments. At a fixed pumping rate, the normalized mass fraction of $CaBr_2$ was assumed to be equal

to 0.5 when one pore volume of displacing fluid was pumped into the system, where one pore volume is equal to the total volume of water in the column. Due to fluctuations in the pumping rate and errors in the time measurements, this was not observed. To correct the phase error, a time correction parameter was applied to match the assumed condition; these corrections were typically small and well within the expected experimental error. Once the phase error was removed, the outflow mass fraction of $CaBr_2$ was splined for the duplicate experiment so that the data could be compared at identical times. The ℓ_2 error norm was then calculated at each time step and normalized by the number of data points. The error norms for the experiments in Column B were at least an order of magnitude lower for each duplicate experiment than for Column A. The columns were reused for many experiments. The fitted tracer dispersivities for Column A changed more than Column B, which is consistent with the experimental error norms and is a result of minor changes in pore structure with time. No changes in the experimental set-up or procedure changed between the two columns. The error norms for the duplicate experiments provide a bound on the accuracy that would be expected from an ideal model and provides a means to evaluate model error versus experimental error.

The published works on validating non-dilute transport models have focused on the lower end of the non-dilute spectrum. Watson et al. (2002c) examined a displacing fluid with maximum mass fraction of NaCl of 0.177 ($\Delta\rho^w = 0.130$ g/cm^3 and $\Delta\hat{\mu} = 4.46 \times 10^{-3}$ g/cm-s) and a resident fluid of pure water was used for all experiments. Hassanizadeh and Leijnse (1995) also conducted and modeled displacement experiments with the displacing fluid having a maximum mass fraction of 0.235 of NaCl ($\Delta\rho^w = 0.175$ g/cm^3 and $\Delta\hat{\mu} = 7.84 \times 10^{-3}$ g/cm-s), however the resident fluid had dilute levels of NaCl present. Landman et al. (2007a) generated numerical experiments without directly representing a salt species and simulated a maximum density difference of 0.2 g/cm^3, while viscosity variations were neglected and the underlying macroscale model was assumed to be correct. Activity was not calculated or considered in these works, however at the maximum NaCl mass fraction of 0.235, $\Delta\hat{\gamma}^{\overline{\overline{Aw}}} = -0.1$ at 25°C (Hamer and Wu, 1972). For our dataset, the maximum mass fraction of $CaBr_2$ is 0.56, with a maximum density difference of 0.47 g/cm^3, maximum viscosity difference of 27.6 $\times 10^{-3}$ g/cm-s, and activity differences that are both positive and negative, with a maximum activity difference of 27.23.

2.5.3 Dilute Flow and Transport

The laboratory experiments were modeled as a one-dimensional system, therefore, only the longitudinal dispersivity coefficient needed to be fit to the dilute experiments to fully parameterize the dispersion. The dilute flow and transport model was used to determine the longitudinal dispersivity for the four dilute experiments that were performed.

For the parameter estimation, the ℓ_2 error norm between the observed outflow mass fraction from the model and the laboratory experiments was minimized. A time correction parameter was fit to the data to adjust for any phase error, which was previously discussed. Phase error in the experimental results stemmed from time measurement errors, and variations in tubing lengths and flow rates. The optimized longitudinal dispersivity values and time correction factors for the four tracer experiments are included in Table 2.2. The time correction parameters were within expected error bounds and small compared to the duration of the experiments, where 15,400 seconds were required for one pore volume of fluid to pass through column A and 15,200 seconds for column B. For the non-dilute simulations, the optimized longitudinal dispersivity value of the tracer experiment that preceded the experiment was used.

Table 2.2: Fitted Longitudinal Dispersivity

Experiment	$\hat{\alpha}_L$ (cm)	t_{corr} (s)
Col_AT1	0.137	-40.7
Col_AT2	0.155	-42.7
Col_BT1	0.108	-19.1
Col_BT2	0.098	-11.7

A dispersion coefficient $\left(\hat{D}\right)$ was also fit to the non-dilute displacements using the dilute flow and transport model. This was done as a measure of the front sharpening observed in the non-dilute cases. The fitted dispersion coefficients ranged from 0.569 - 9.18×10^{-4} cm/s^2, where the smallest dispersion coefficient was from experiment Col_A16 and the largest from experiment Col_AT2, which was a dilute tracer experiment. Figure 2.1 shows the fitted Fickian model profiles for these two experiments. While the dilute flow and transport model works well for the dilute tracer experiment, for the non-dilute displacement, the dilute model is not able to represent accurately either the leading or the trailing portion of the front. With a constant dispersion coefficient and density, the dilute flow and transport model can only produce a symmetric outflow profile, however, for non-dilute systems the

outflow profile is asymmetric according to our laboratory data. For the sharpest experiment, the fitted dispersion coefficient approaches the effective molecular diffusion coefficient of 0.096×10^{-4} cm/s^2. It can be observed from these two cases that non-dilute transport can result in marked sharpening of a breakthrough curve compared to an ideal dilute tracer.

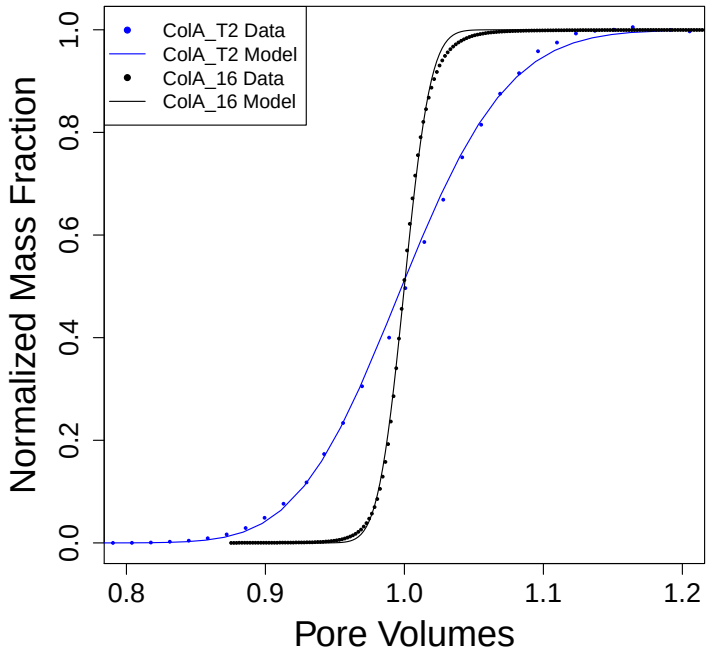

Figure 2.1: Results from fitting the Fickian dispersion coefficient with the dilute flow and transport model for the least and most disperse scenarios. The least disperse experiment had an incoming $CaBr_2$ mass fraction of 0.4 and pure water as the resident fluid.

2.5.4 Non-Dilute Parameter Estimation Results

The unknown parameters in the nonlinear Fickian and TCAT models, as well as time correction parameters, were fit by selecting a subset of the experimental data that was representative of the entire dataset. This was done for both of the columns as the packing of the porous media changed slightly between the two columns.

For Column A, the subset of data selected for the parameter estimation included a low (ColA_12), medium (ColA_21), and high concentration (ColA_16) displacement as well as a case in which the resident fluid was brine (ColA_24). The sum of the ℓ_2 error norms was minimized and the error norms

were normalized by the total number of observations for each experiment so all experiments were weighted the same.

The results of the nonlinear Fickian Model and TCAT model for Column A experiments are shown in Figure 2.2. For the nonlinear Fickian model, the optimized parameter ($\hat{\beta}$) was $5.97 \pm 0.21 \times 10^6$ g/cm^2-s and the sum of the ℓ_2 error norms was 11.3×10^{-4}. This optimized value is the same order of magnitude as reported in other work (Hassanizadeh and Leijnse, 1995; Landman et al., 2007b; Watson et al., 2002c). For the TCAT model, the optimized parameters were $\hat{\beta}_1^T = 2.53 \pm 0.01 \times 10^7$ g/cm^2-s and $\hat{\beta}_2^T = 1.31 \pm 0.05 \times 10^8$ g/cm^2-s and the error measure was 4.43×10^{-4}.

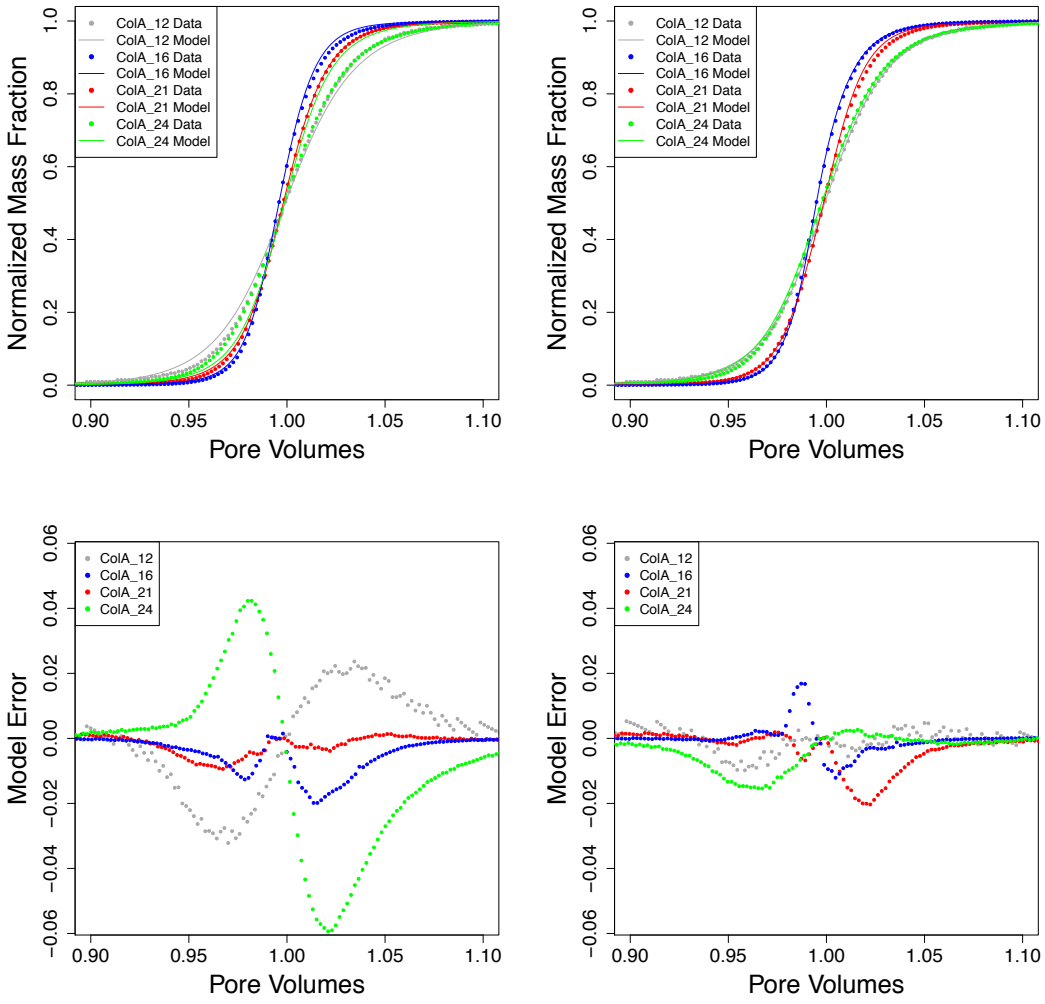

Figure 2.2: Parameter estimation results and error for the nonlinear Fickian Model (left) and the TCAT model (right) for Column A.

From the parameter estimation, we see that the TCAT model produces a better fit for each of the experiments compared to nonlinear Fickian model, with the most noticeable improvements for the low concentration displacement (ColA_12) and the scenario where there is a non-dilute fluid initially in the column (ColA_24). The difference between the resident and displacing fluid properties for these two experiments vary by orders of magnitude, however the experimental results show a similar outflow profile. The literature suggests that as the mass fraction, or density difference, between the displacing and displaced fluids increases, the dispersion should decrease (Landman et al., 2007a; Schotting and Landman, 2004; Watson et al., 2002c). Our experimental results however suggest otherwise as ColA_24 has a mass faction difference between the displacing and resident fluids of 0.08 ($\Delta\rho^w = 0.14$ g/cm^3) while ColA_12 has a mass fraction difference of 0.025 ($\Delta\rho^w = 0.021$ g/cm^3). The nonlinear Fickian model only considers dispersion due to the gradient of the mass fraction, however from the laboratory data it is apparent that the dispersion is not just a function of the gradient of the mass fraction.

The ℓ_2 error norm for ColA_16 for the TCAT model (1.42×10^{-4}) is less than the ℓ_2 error norm for the duplicate laboratory runs (2.30×10^{-4}) and the nonlinear Fickian model error norm for this experiment (2.36×10^{-4}) is approaching this value as well. For ColA_12, both the TCAT model error norm (0.53×10^{-4}) and the nonlinear Fickian model error norm (2.19×10^{-4}) are larger than the error norms for the experiment (0.19×10^{-4}), but the TCAT model is of the same order. No duplicate laboratory experiments were performed for the other two displacements included in the parameter estimation. These results show that for Column A, the error in the TCAT model is on the same order of magnitude as the error in the laboratory experiments.

Only two experiments were used for the fit for Column B and this parameter estimation was done to determine the impacts of the porous media repacking and to examine the scenario where we have a constant density difference between the incoming and resident fluids. The extremes of the dataset (ColB_21 and ColB_25) were used for the parameter estimation.

For the nonlinear Fickian model, the optimized parameter ($\hat{\beta}$) was found to be $5.20 \pm 0.27 \times 10^6$ g/cm^2-s with a error norm of 4.76×10^{-4} and for the TCAT model the optimized parameters were $\hat{\beta}_1^T = 2.01 \pm 0.01 \times 10^7$ g/cm^2-s and $\hat{\beta}_2^T = 2.05 \pm 0.04 \times 10^8$ g/cm^2-s, with an error norm of 3.45×10^{-4}. The optimized parameters for the TCAT model changed relatively more than the parameter for the nonlinear Fickian model from Column A to Column B, and as shown in Figure 2.3, the TCAT model produced better fits to the observed data. The nonlinear Fickian model for Column

B produces a profile that is too sharp for ColB_25 while the exact opposite behavior is observed for the TCAT model for ColB_25, with the TCAT model producing a better fit. The simulated profiles for ColB_21 are similar for both of the models. This demonstrates the need for additional dispersive terms that are included in the TCAT model. The longitudinal dispersivity determined from the dilute tracer experiments were both slightly lower for Column B than Column A, which shows that the packings were similar but not identical in this measure.

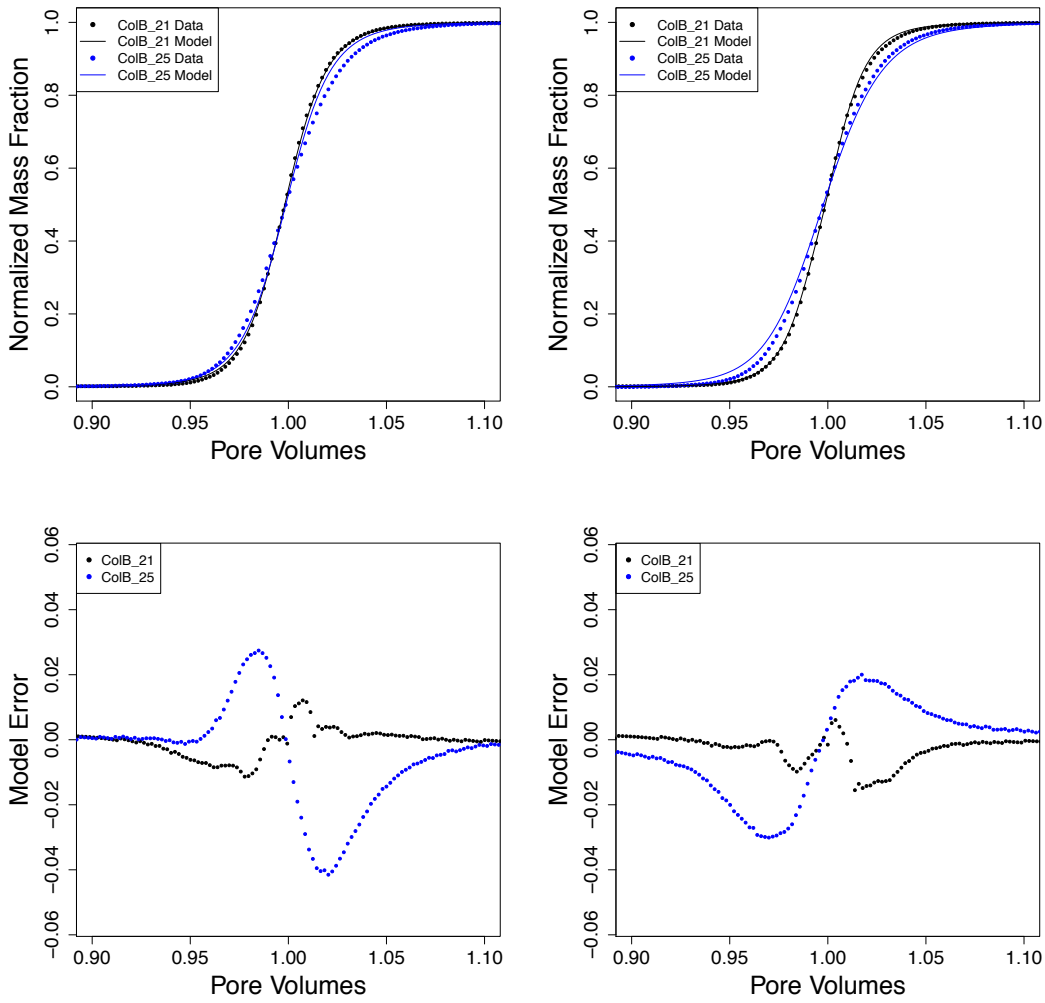

Figure 2.3: Parameter estimation results and error for the nonlinear Fickian model (left) and the TCAT model (right) for Column B.

Unlike the parameter estimation results from Column A, the error norms of both the TCAT model and nonlinear Fickian model were larger than the experimental error norm for Column B. While the

model errors are of the same magnitude for both of the columns, the laboratory errors were less for Column B as compared to Column A.

While the ℓ_2 error norm for the TCAT model is less than that of the nonlinear Fickian model for the two parameter estimations, the TCAT model has three parameters that must be fit to the experimental data ($\alpha_L, \hat{\beta}_1^T, \hat{\beta}_2^T$) while the nonlinear Fickian model has only two parameters ($\alpha_L, \hat{\beta}$). To accurately compare the two models, the Akaike information criteria (AIC) and the Bayesian information criteria (BIC) were calculated (Aho et al., 2014). Both of the measurements account for the number or parameters involved in the model, as well as the accuracy of the model. For both of the measures and for both of the parameter estimations, the TCAT model is the best option. While having an additional parameter, as compared to the nonlinear Fickian model, and having lower ℓ_2 error norms, the TCAT model also includes additional physical phenomena that is not accounted for in these model selection criteria.

2.5.5 Forward Simulation Results

The optimized parameters were used to determine how well each of the models can predict the results of experiments not used in the parameter estimation procedure. Table 2.3 shows the ℓ_2 error norm for each experiment for both the nonlinear Fickian and TCAT models, where the ℓ_2 error norm was averaged when replicate experiments were performed. The average error for the TCAT model is 1.33×10^{-4} and 2.50×10^{-4} for the nonlinear Fickian model. The TCAT model reduces the error by 46% as compared to the nonlinear Fickian model.

Figure 2.4 shows the results for the nonlinear Fickian and TCAT models for experimental Set 1. The TCAT model outperforms the nonlinear Fickian model for all experiments shown except for ColA_15, ColA_21, and Col_B21. with the latter two experiments being used in the parameter estimation. While the nonlinear Fickian model can accurately predict the sharpest displacement shown (ColA_15), the optimized parameters are not capable of simulating the lower concentration displacements as accurately. The accuracy of the TCAT model is nearly independent of the salt concentration of the displacing fluid. The TCAT model is able to more accurately capture the trailing end of the outflow mass fraction profile as opposed to the leading end for the lowest concentration displacement. This may be a result of the uncertainty in the activity function at low mass fractions (Goldberg and Nuttall, 1978).

Table 2.3: Forward Simulation Results for Both Models and Columns

Experiment ID	Nonlinear Fickian Model $\ell_2 \times 10^{-4}$	TCAT Model $\ell_2 \times 10^{-4}$
ColA_11	4.07	1.63
ColA_12*	2.19	0.53
ColA_13	3.82	1.52
ColA_14	1.24	0.89
ColA_15	1.48	1.61
ColA_16*	2.36	1.42
ColA_21*	0.50	0.95
ColA_22	1.68	0.92
ColA_23	4.21	1.58
ColA_24*	6.24	1.53
ColB_21*	1.10	1.26
ColB_22	1.40	1.08
ColB_23	1.02	0.51
ColB_24	2.52	2.42
ColB_25*	3.66	2.19

*Used in parameter estimation

The results for experiment Set 2 are shown in Figure 2.5. Only minor changes are observed in the outflow mass fraction profiles for the nonlinear Fickian model. As mentioned, the literature suggests that the reduction of dispersion is solely a function of the density difference between the two fluids, however the experimental data suggests that dispersion is dependent on other factors. The slight variation in the nonlinear Fickian model breakthrough curves is due to a smaller mass fraction difference that is required to maintain a constant density as the mass fraction increases. This trend can be seen as the nonlinear Fickian model predicts a sharper profile with a larger mass fraction difference between the fluids. The TCAT model, where activity gradients are included, is better at capturing the laboratory data.

For the constant density experiments, the activity and viscosity are the two parameters that are not controlled and both are varying by orders of magnitude and the activity is changing signs. Theoretically, a more viscous fluid would have less dispersion than a less viscous fluid because the velocities in the pore throats do not vary as greatly. We see in the constant density experiments more dispersion despite an increase in the viscosity. This suggest that the activity is the dominating term for dispersion as compared to the viscosity.

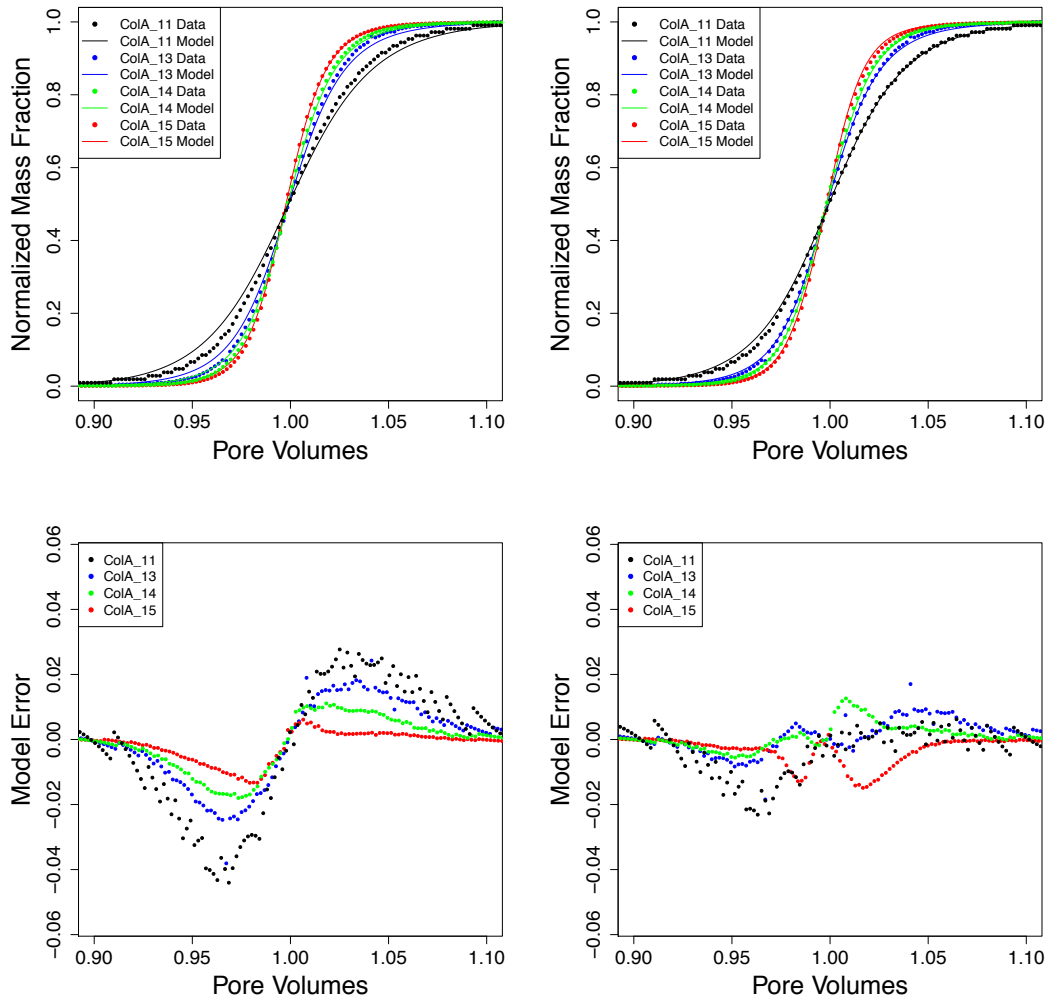

Figure 2.4: Forward simulations results and model error for the nonlinear Fickian model (left) and the TCAT model (right) for experiments when pure water was initially in the column.

2.5.6 Components of Mass Flux

The four components of the dispersive mass flux at two different times for four simulations are shown in Figure 2.6. The four simulations include a low (ColA_11), medium (ColA_15), and high (ColA_16) concentration displacement, as well as a displacement where brine is initially in the column (ColA_24). The terms associated with the gradients of pressure are neglected as the values were so small that no impacts were observed.

Beginning with the low concentration displacement, the dispersive term associated with gradient of the activity (Γ_z^D) is always negative. In the dilute limit, the activity approaches one and as the mass fraction increases, the activity decreases quickly to a minimum value of 0.49 when the mass fraction is

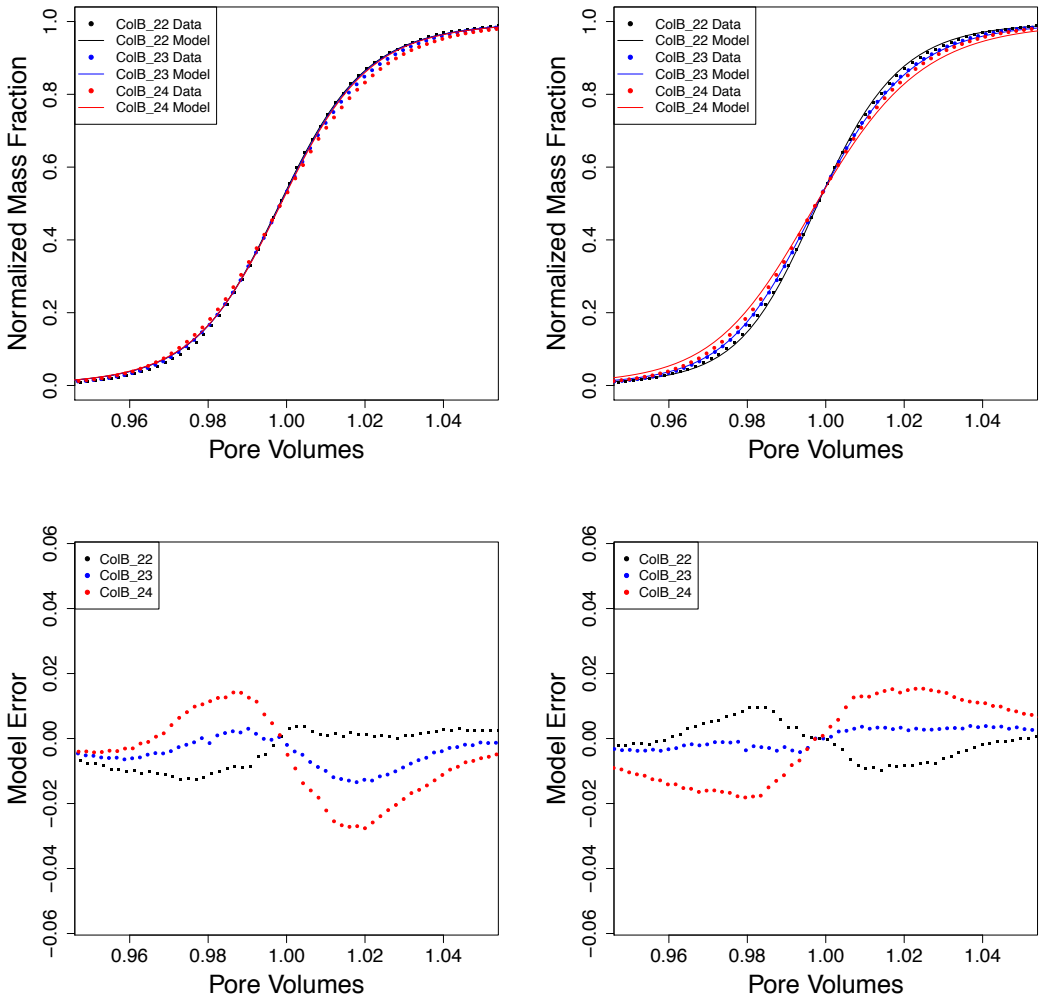

Figure 2.5: Forward simulations results and model error for the nonlinear Fickian model (left) and the TCAT model (right) for experiments when brine was initially in the column.

0.063. As the mass fraction continues to increase past this point, the activity increases exponentially. For the low mass fraction scenario, the gradient of the activity will always have an opposite sign of the gradient of the mass fraction. The dispersive term related to the gradient of the activity reduces the total dispersion in the system. For this experiment, the diffusive terms are negligible.

For the medium and high displacement scenarios, Γ_z^D is both positive and negative. On the leading front, the dispersive activity flux is negative, however once the activity is larger than the inflection point of the activity function, the flux becomes positive. This results in the sum of the fluxes being asymmetric. Comparing the medium and high displacement scenarios, the dominance of the dispersive flux related to the mass fraction (Ω_z^D) reduces for the high concentration displacement, while the other

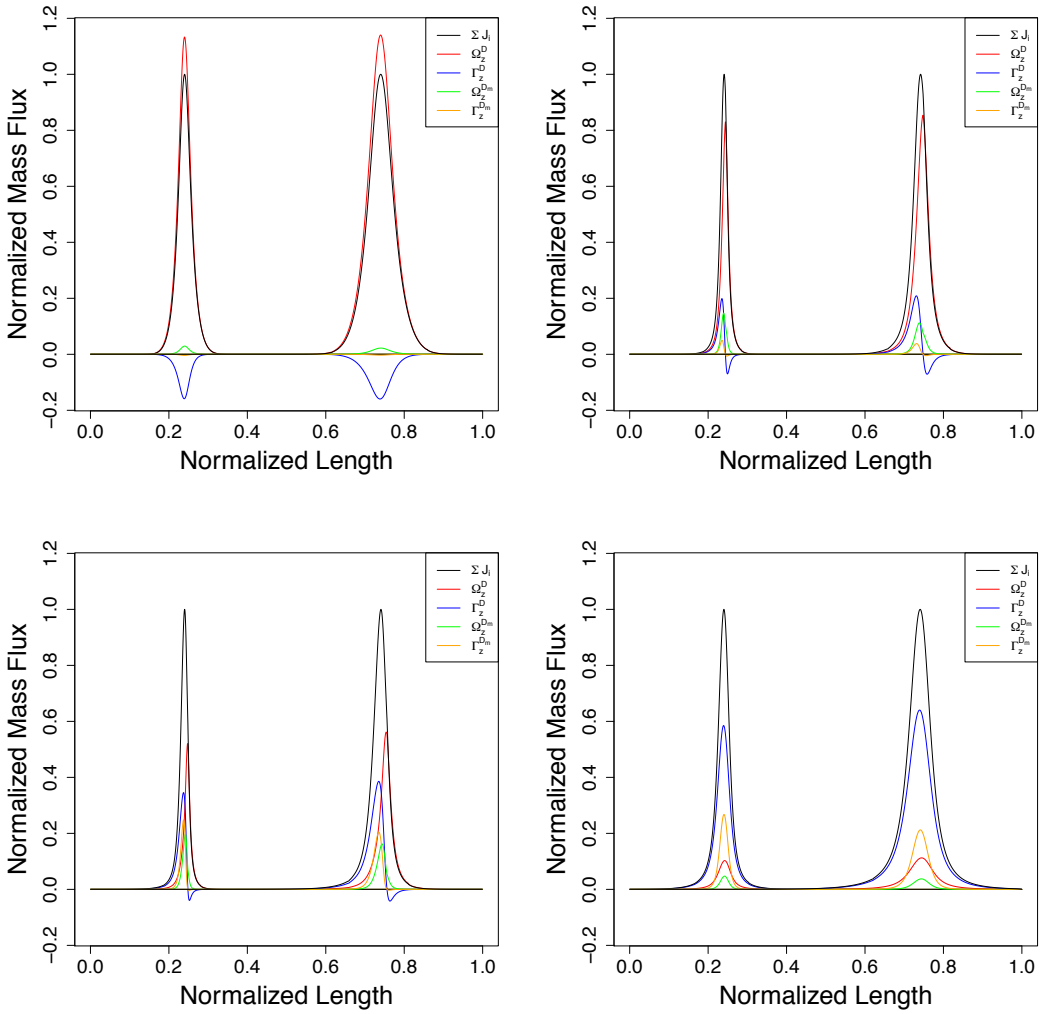

Figure 2.6: The four flux terms and the sum of the fluxes, for a low (top left), medium (top right), high (bottom left) concentration displacement, and a displacement experiment where brine is initially in the column (bottom right).

three flux terms become more significant. Additionally, the diffusive activity flux (Γ_z^{Dm}) is larger than the diffusive mass fraction flux (Ω_z^{Dm}) for the most concentrated displacement. The activity function is exponential after the inflection point, therefore small gradients in the mass fraction for the high concentration displacement result in large gradients in the activity.

For ColA_24, the resident brine has a mass fraction greater than the inflection point of the activity function so Γ_z^D is strictly positive. For this experiment, Γ_z^D and Γ_z^{Dm} are the dominant terms making up $>$80% of the total mass flux. For displacements where the mass fraction of salt in the displacing fluid is large, whether the resident fluid is a brine or not, the diffusive terms become important. Additionally, for experimental Set 2, as the mass fraction increases, Ω_z^D decreases monotonically while Γ_z^D

and $\Gamma_z^{D_m}$ increase monotonically. This shows that the inclusion of the activity in the TCAT model is why the model is able to correctly simulate the constant density difference experiments.

As noted with the mass flux terms, the activity allows for asymmetry in the sum of the mass flux. The dilute flow and transport model is unable to capture the tails of the outflow mass concentration for non-dilute displacements (Figure 2.1). The asymmetry in the mass flux terms allows the TCAT model to correctly model the tails, which is lacking in the more symmetric nonlinear Fickian model. Figure 2.7 shows the skewness of the outflow concentration for the laboratory data, and the nonlinear Fickian and TCAT models for all simulations. The skewness of the TCAT model differs significantly from zero as the difference in the incoming and resident mass fraction increases, which is where laboratory data shows asymmetry. Overall, the TCAT model is able to correctly capture the skewness of the underlying data due to the inclusion of the activity in the model.

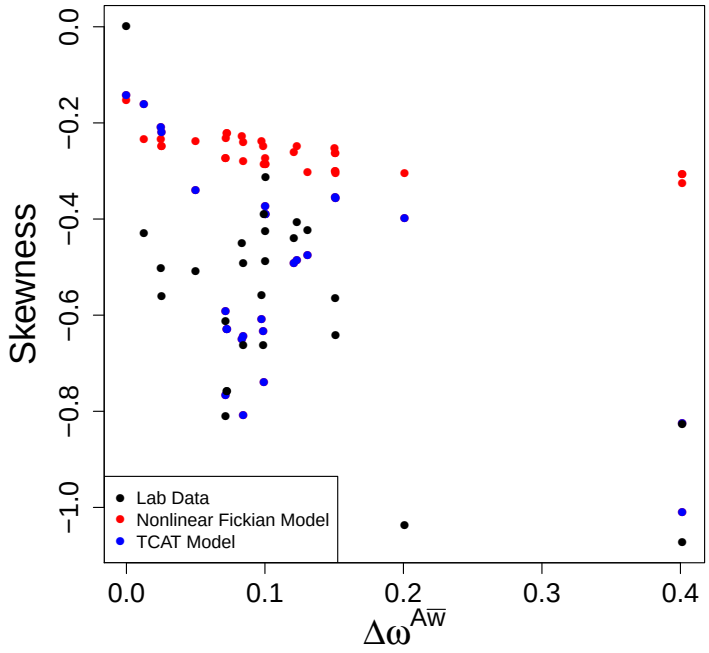

Figure 2.7: The skewness of the outflow concentration for all simulations for the laboratory data and the Nonlinear Fickian and TCAT models.

2.5.7 Model Alternatives

The TCAT model consists of two parameters, one related to the dispersive flux due to the gradient in the mass fraction and the other due to the gradient of the activity. The two parameters ensure that the entropy of the system is always increasing and allows the flexibility to accurately model non-dilute behavior where the gradient of the density is constant but the gradients of the activity and viscosity vary. The optimized parameters are believed to be functions of the Darcy velocity as has been shown with the nonlinear Fickian model (Watson et al., 2002c). At our current level of understanding, however, these parameters are simply model parameterizations that are fit to match the experimental data. Through many attempts, the current form was found. The addition of the terms multiplying the parameters and gradients of the mass fraction and activity yielded better fits. Model attempts included parameters multiplying the gradients of the fluid properties (density, viscosity, mass fraction, and activity) and various combinations thereof, however, no attempted version improved on the current form despite the addition of more parameters.

The species transport equation for the TCAT model includes a gradient of pressure term that is multiplied by the dispersion coefficient that was not discussed. Unlike the dispersive terms involving the gradients of the mass fraction and the activity, the inclusion of this term and an additional parameter in the model did not result in any improvements. Additionally, the diffusive and dispersive terms related to the gradient of the pressure were negligible for every simulation.

2.5.8 Limitations

The laboratory data in this work isolated different physical phenomena and examined higher mass fractions, and density and viscosity differences between the two fluids than the experimental data published to date. However, all of the experiments were performed with one flow rate and one type of media and no internal probes were used. Watson et al. (2002c) developed a dataset that included two types of porous media, different flow rates, constant flow and constant head boundary conditions, as well as including internal probes that measured the pressure and mass fraction of NaCl. From this dataset, additional information was obtained that allowed for the determination of the dependency of the nonlinear Fickian model on different experimental conditions. This dataset however did not include the large differences in the fluid properties examined in this work. Applying the TCAT model to

data with varying media, flow rates, and for cases in which additional model variables were measured would provide an opportunity to further evaluate and validate the TCAT model.

2.6 Summary and Conclusions

The following can be concluded from this analysis:

- A TCAT model was developed to simulate non-dilute flow and species transport in porous media. This model has the advantages of a firm connection between the microscale, or pore scale, and the macroscale; a thermodynamically consistent basis; and the explicit inclusion of a dissipative term that arises from a spatial gradient in chemical activity.

- An experimental dataset was collected that improved understanding of non-dilute flow and transport by examining systems where the mass fraction, density and viscosity differences between the fluids were greater than previously published. A series of experiments was also performed where the density difference between resident and displacing fluids was held constant but the mass fractions of $CaBr_2$ were varied. The experimental data set allowed for the comparison of the existing nonlinear Fickian model and the TCAT model.

- The dispersion for stable displacements is not solely a function of the density gradient or the mass fraction gradient, and activity effects need to be considered for cases in which changes in activity are large.

- The TCAT model outperformed the nonlinear Fickian model. The inclusion of the activity in the TCAT model is the likely reason why this model was better suited at simulating the laboratory data.

- Non-dilute displacements result in an asymmetric mass flux, which can be seen by attempting to fit the dilute flow and transport model to non-dilute experiments and the failure to accurately capture the tails of the breakthrough profile. The mass flux in the TCAT model can be asymmetric, due to the inclusion of the activity.

CHAPTER 3: A PHYSICALLY-BASED ENTROPY PRODUCTION RATE METHOD TO SIMULATE SHARP FRONT TRANSPORT PROBLEMS IN POROUS MEDIA

3.1 Introduction

Sharp-front problems arise routinely in the geosciences. Examples include dilute species transport in fluids that are dominated by advection, non-dilute transport, and biochemically reactive systems (Farthing and Miller, 2000; Smith et al., 1991; Weigand et al., 2018b; Widdowson et al., 1988). These problems arise for both porous media and transport phenomena in surface waters. They are typically described using mechanistic models that in some cases are formally hyperbolic and in many cases involve behavior that may tend toward a hyperbolic limit (LeVeque, 1992).

The numerical approximation of hyperbolic operators in applied mathematics and the geosciences is considered mature (Guermond and Popov, 2017; LeVeque, 2002; Miller et al., 2013). A variety of Godunov-type methods based upon flux-limiting or slope-limiting approaches arising from the solution of a Riemann problem have been developed using finite volume approaches. The maturity of these approaches is manifest in the availability of general-purpose solvers, and the routine use of these approaches in the geosciences (LeVeque, 2002).

The success of mature finite volume methods notwithstanding, unstructured-mesh approaches are often useful for problems in the geosciences due to the occurrence of irregular boundaries of the domain and the irregular distribution of materials with markedly different physical properties within the domain that must be resolved for accurate simulations (Miller et al., 2016). FEMs for sharp-front problems are, however, much less mature than Godunov-type finite volume methods (Guermond and Popov, 2017; Kuzmin, 2006).

The use of entropy has a long history in the theory for hyperbolic PDEs and in numerical methods (Harten et al., 1976, 1997; Lax, 1971; LeVeque, 1992; Osher and Chakravarthy, 1984; Smoller, 1994). Entropy conditions and functions can ensure that weak solutions converge to the physically relevant solution. E-schemes are a class of numerical approaches that ensure entropy inequalities are satisfied (Osher, 1984). Lee and Wheeler (Lee and Wheeler, 2017) and Puppo (Puppo, 2003) use entropy as

a measure for grid refinement and shock tracking, respectively. The entropy viscosity schemes from Guermond et al. (Guermond and Nazarov, 2014; Guermond et al., 2010, 2017, 2014, 2011; Guermond and Popov, 2014, 2017) have received considerable recent attention in the literature as a means to add sufficient dissipation to a FEM solution to suppress the undesirable numerical errors associated with approximating hyperbolic operators using standard conforming FEMs. Entropy-viscosity methods advanced to date have relied upon classical, mathematical entropy-flux pairs to guide the dissipation added to the numerical approximation, which is often referred to as artificial viscosity.

On the other hand, continuum mechanical work over the last 15 years has led to the development of the thermodynamically constrained averaging theory (TCAT) (Gray and Miller, 2014). TCAT is an approach for formulating mechanistic macroscale models that are consistent with microscale physics and thermodynamics. TCAT models assure that the resultant models are consistent with the second law of thermodynamics, which is based upon the formulation of an entropy inequality (EI). The TCAT EI is an expression for the rate of entropy production based upon the operative dissipative processes in a system. Whether a physically-based entropy production rate provides useful information that can be used to formulate a dissipation function that leads to an efficient FEM model for sharp-front problems is an open question. If an EI can serve such a purpose, existing continuum mechanical theory could be leveraged to develop efficient numerical methods to approximate complex multiphase, multicomponent systems that fall outside the range of classical models for which traditional mathematical entropy-flux pairs are well established.

3.2 Objectives

The overall goal of this work is to advance and evaluate a FEM for sharp-front problems based upon the physical rate of entropy production. The specific objectives of this work are: (1) to formulate the entropy production rate for general species transport in a porous medium system; (2) to formulate a scheme where the numerical viscosity is based upon the physical production of entropy; (3) to evaluate the new approach for dilute and non-dilute species transport; and (4) to examine ways in which the method can be extended to other problems.

3.3 Background

The background needed to meet the objectives of this work includes entropy viscosity methods, and the TCAT approach for model formulation and the calculation of a physically-based entropy production. The status of knowledge on these two components are considered in turn.

Standard conforming Galerkin finite elements can produce non-physical oscillations for hyperbolic or advection-dominated problems that are not strictly hyperbolic. To reduce these oscillations, either artificial viscosity (or diffusion) can be added to the solution or the computational mesh can be refined, which lowers the mesh Peclet number (Baliga and Patankar, 1980; Carver and Hinds, 1978). Both of these options have shortcomings. Adding artificial viscosity to a solution will dampen oscillations but will also smear the solution and the amount of artificial viscosity to add is not known *a priori*. For large simulations, refining the underlying computational mesh may not be possible given a constraint on available computational resources.

For the artificial viscosity approach, the amount of required viscosity to eliminate oscillations is dependent on the steepness of the solution relative to a given mesh resolution, with more artificial viscosity needed near large gradients in the dependent variable, which is where non-physical oscillations occur. Naturally, as the mesh is refined, less artificial viscosity is needed to produce a smooth solution. Von Neumann and Richtmyer (VonNeumann and Richtmyer, 1950) introduced this method by including a nonlinear viscosity term with a tuning parameter that was identical to a second-order truncation error.

The original work of Von Neumann and Richtmyer (VonNeumann and Richtmyer, 1950) has seen many improvements and extensions. Tadmor (Tadmor, 1990) examined the use of artificial viscosity in the context of spectral methods and introduced a method where the artificial viscosity is only included for higher frequencies. Inspired by the work of Tamdor, Calhoun-Lopez and Gunzburger (Calhoun-Lopez and Gunzburger, 2006) developed a method for finite elements based on hierarchical basis functions, which allows artificial viscosity to only be added at smaller scales. With that approach, the introduction of the viscosity does not compromise the accuracy of the solution. Xin and Flaherty (Xin and Flaherty, 2006) introduced artificial viscosity at shocks with discontinuous Galerkin finite elements, where the discontinuous Galerkin residual was used to scale the amount of artificial viscosity. Their approach is dependent on a tuning parameter that can be determined *a priori* for some systems.

The entropy viscosity (EV) method proposed by Guermond et al (Guermond and Nazarov, 2014; Guermond et al., 2018, 2010, 2017, 2014, 2011; Guermond and Popov, 2014, 2017) is an approach to parameterize the amount of artificial viscosity needed to produce a non-oscillatory solution based on the entropy production of the system and has seen significant developments in recent years. As originally formulated in (Guermond et al., 2011), the entropy viscosity approach is a higher order approach for continuous finite elements that does not depend on flux or slope limiters. The original formulation used the weak form of the Laplacian, which (Guermond and Nazarov, 2014) does not guarantee the maximum principle is obeyed. The entropy viscosity was dependent on two tuning parameters, the local mesh size, and the entropy, which was normalized by the global entropy average (Guermond et al., 2011). Guermond and Nazarov (Guermond and Nazarov, 2014) improved the EV approach by formulating an explicit second-order, maximum-preserving scheme for arbitrary meshes, any Lipschitz flux, and any spatial dimension. This was accomplished by introducing a graph Laplacian for the viscosity, introducing a correction term to the lumped mass matrix to approximate the inverse of a consistent mass matrix, and using the flux-corrected transport paradigm. The entropy viscosity in this updated approach is no longer dependent on the mesh size and includes an edge-based stabilization term but still includes two tuning parameters (Guermond and Nazarov, 2014).

A recent formulation by Guermond et al. (Guermond et al., 2018) is a second-order, parameter-free, edge-based viscosity approach. This approach first determines a maximum-preserving artificial viscosity by either a local-extremum-diminishing approach or a guaranteed maximum-speed approach. The guaranteed maximum-speed approach is preferred because the local-extremum-diminishing approach can violate the entropy condition for transonic rarefactions (Guermond et al., 2018). An extension to the low-order viscosity was developed where the viscosities are smoothed to mimic the flux-limiting approach, while still maintaining the maximum principle (Guermond and Popov, 2017). The higher order viscosity is constructed by taking the minimum of the low-order viscosity and the nondimensional entropy residual, which is a function of the difference between the current solution and the Galerkin solution (Guermond et al., 2018). The entropy residual, as posited in (Guermond and Popov, 2017), includes the time discretization between the Galerkin and current solution, so a "commutator" approach was proposed in (Guermond et al., 2018) so the choice of time discretization does not impact the entropy residual.

TCAT is an approach that can be used to formulate continuum mechanical models based upon microscale principles at some combination of larger length scales in each spatial dimension, which may be macroscale or megascale (Gray and Miller, 2014). The microscale is the smallest scale at which continuum mechanical approaches are applicable and applied to a given entity (phase, interface, common curve, common point), and the boundaries of juxtaposed entities are fully resolved in space and time. The macroscale is a length scale at which a point represents the centroid of an averaging region that may contain all entities in some measure. At the macroscale, the boundaries of entities are not explicitly resolved, but measures of the average extent of the entities are evolved (volume fractions, specific interfacial areas, etc). The megascale is the system scale and all phenomena are resolved only through transport through the boundaries of the domain; the entire domain is treated in an averaged sense with no spatial resolution in any megascale dimension. Larger scale three-dimensional domains may be modeled with any combination of macroscale and megascale approaches. Larger scale approaches are necessary for essentially all natural porous medium systems, and many engineered and organismic system as well, due to the computationally intractable nature of microscale approaches for such applications.

The TCAT approach has several attractive features (Battiato et al., 2019; Gray and Miller, 2005, 2014; Miller and Gray, 2005; Miller et al., 2017). These features include a uniform microscale basis for all conservation and thermodynamics, a precise upscaling of all quantities from the microscale to larger scales, the inclusion of interfaces, common curves, and common points, the formulation and use of entropy inequalities to constrain closure relations to be consistent with the second law of thermodynamics, the development and use of evolution equations based on averaging theorems to reduce the set of closure relations needed, geometrically based state equations that are hysteretic free (Miller et al., 2019a), and, because of the rigorous connection between scales, the ability to evaluate and validate larger scale models unambiguously with microscale observations or simulations (Gray et al., 2015). While other upscaling approaches are available (Battiato et al., 2019; Gray et al., 2013), no other upscaling method provides the entire desirable set of attributes annotated above for TCAT.

The TCAT approach involves the following steps. Conservation of mass, momentum, and energy equations, balance of entropy equations, thermodynamic equations, and equilibrium conditions are developed at the microscale for each entity in the system. Averaging operators are applied to each equation and multiscale averaging theorems (Gray et al., 1993; Gray and Miller, 2013, 2014; Miller

and Gray, 2008) are applied to transform the larger scale equations into forms containing the fewest number of variables possible; this transformation results in differentials of averaged quantities rather than averages of differential quantities. A larger scale entropy inequality is developed for the system and connected to the dissipative processes that produce entropy, which are specified in the conservation equations. A resultant flux-force form is developed for entropy production, which is in turn used to constrain the permissible form of closure relations that can be used to formulate a closed, solvable model at the larger scale. Evolution equations, derived purely from the averaging theorems (Gray et al., 2015; Gray and Miller, 2010, 2014), and equations of state (Gray et al., 2019; McClure et al., 2018; Miller et al., 2019a) also are used to resolve the closure problem and produce closed, solvable models for which all quantities are described in terms of microscale precursors. The TCAT approach has been used to derive macroscale models for single-fluid flow (Gray and Miller, 2006), single-fluid flow and species transport (Gray and Miller, 2009; Miller and Gray, 2008; Weigand et al., 2018b), two-fluid flow (Jackson et al., 2009), and two-fluid flow and species transport (Rybak et al., 2015), all for porous medium systems. TCAT model hierarchies have also been developed for single fluid flow in a porous medium at the megascale (Gray and Miller, 2009), the transition between a two-fluid-phase porous medium system and a single-fluid system (Jackson et al., 2012), and for sediment transport in turbulent surface waters (Miller et al., 2018a, 2019b).

The TCAT entropy inequality yields an expression for the rate of entropy production resulting from dissipative processes (Gray and Miller, 2014; Miller and Gray, 2005). This physically-based entropy production rate could be of use in formulating artificial dissipation in numerical methods, such as the EV method. Such an approach has not been applied or evaluated.

3.4 TCAT Formulation

3.4.1 Non-Dilute Species Transport Model

To explore the use of the physically-based entropy production rate, we consider a specific TCAT application known to yield sharp-front problems at the macroscale: non-dilute species transport in a single-fluid porous medium system (Gray and Miller, 2009, 2014; Weigand et al., 2018b). Specifically, we consider a TCAT model from a general hierarchy subject to restrictions that include: entity-based conservation of momentum; isothermal conditions; no mass transfer between entities; an incompress-

ible, immobile solid phase; a binary species composition of the fluid phase; a first-order flux-force closure for all fluxes except the stress tensors, which are considered macroscopically inviscid and of zero order; neglect of higher order kinetic energy terms; neglect of inertial effects in the conservation of momentum equations; and a spatially one-dimensional model is considered in which the compositional evolution is gravitationally stable at the macroscale. Further details on the TCAT model development process, restrictions imposed, and approximations made are available in the literature detailing the development of the model hierarchy and the simplification to the specific model instance considered herein (Gray and Miller, 2009, 2014; Weigand et al., 2018b). This non-dilute transport model has been shown to represent observed systems accurately.

The resultant closed model consists of a conservation of mass equation for the water phase given by

$$\frac{\partial\left(\epsilon^{\overline{\overline{w}}}\rho^{w}\right)}{\partial t}=\frac{\partial}{\partial z}\left[\frac{\hat{k}\rho^{w}}{\hat{\mu}}\left(\frac{\partial p^{w}}{\partial z}+\rho^{w}g\right)\right]\ , \tag{3.33}$$

where the conservation of momentum equation reduces to Darcy's law, which has been used to represent the specific discharge, $\epsilon^{\overline{\overline{w}}}v^{\overline{w}}$; t is time, $\epsilon^{\overline{\overline{w}}}$ is the volume fraction, ρ^{w} is the density, $v^{\overline{w}}$ is the velocity, z is the direction of flow oriented opposite to the gravitational acceleration, $\hat{k}$ is the intrinsic permeability of the media, $\hat{\mu}$ is the dynamic viscosity, p^{w} is the pressure, g is the magnitude of the gravitational acceleration, and the superscript w denotes the water phase. Note that $\hat{\mu}$ and ρ^{w} are functions of the composition, which are detailed in the literature (Weigand et al., 2018b).

The non-dilute model also includes a conservation of mass equation for species A in a two-species system, which may be written as

$$\begin{aligned}&\frac{\partial\left(\epsilon^{\overline{\overline{w}}}\rho^{w}\omega^{A\,\overline{w}}\right)}{\partial t}+\frac{\partial}{\partial z}\left(\epsilon^{\overline{\overline{w}}}\rho^{w}\omega^{A\,\overline{w}}v^{\overline{w}}\right)\\&-\frac{\partial}{\partial z}\left[\epsilon^{\overline{\overline{w}}}\rho^{w}\left(\frac{\hat{D}_{Aw}}{\hat{\tau}}+\hat{\alpha}_{L}^{T}v^{\overline{w}}\right)\frac{\partial\omega^{A\,\overline{w}}}{\partial z}\right]\\&-\frac{\partial}{\partial z}\left[\frac{\epsilon^{\overline{\overline{w}}}\rho^{w}\omega^{A\,\overline{w}}MW_{B}}{\hat{\gamma}^{\overline{\overline{AW}}}MW_{W}}\left(\frac{\hat{D}_{Aw}}{\hat{\tau}}+\hat{\alpha}_{L}^{T}v^{\overline{w}}\right)\frac{\partial\hat{\gamma}^{\overline{\overline{Aw}}}}{\partial z}\right]=0\ ,\end{aligned} \tag{3.34}$$

where the non-dilute dispersivity is

$$\hat{\alpha}_L^T = \frac{2\hat{\alpha}_L}{1+\sqrt{1-\epsilon^{\overline{\overline{w}}}\rho^w\hat{\alpha}_L v^{\overline{w}}\frac{\partial\omega^{A\,\overline{w}}}{\partial z}\left(\hat{\beta}_1^T-\hat{\beta}_2^T\frac{\omega^{A\,\overline{w}}MW_B}{\hat{\gamma}^{\overline{\overline{Aw}}}MW_W}\frac{\partial\hat{\gamma}^{\overline{\overline{Aw}}}}{\partial\omega^{A\,\overline{w}}}\right)}} \,, \tag{3.35}$$

the non-dilute molecular diffusion coefficient is

$$\hat{D}_{Aw} = \hat{D}_0\frac{\hat{\mu}_0}{\hat{\mu}}\frac{1}{\rho^w V^{\overline{\overline{Bw}}}}\left(1+m^{\overline{\overline{Aw}}}\frac{\mathrm{d}\ln\hat{\gamma}^{\overline{\overline{Aw}}}}{\mathrm{d}m^{\overline{\overline{Aw}}}}\right) \,, \tag{3.36}$$

the molecular weight of water is

$$MW_W = \left(\frac{\omega^{A\,\overline{w}}}{MW_A}+\frac{\omega^{B\,\overline{w}}}{MW_B}\right)^{-1} \,, \tag{3.37}$$

the partial mass volume of species B is

$$V^{\overline{\overline{Bw}}} = \frac{1}{\rho^w}-\omega^{A\,\overline{w}}\frac{\partial}{\partial\omega^{A\,\overline{w}}}\left(\frac{1}{\rho^w}\right) \,, \tag{3.38}$$

where $\hat{D}_{Aw}$ is the molecular diffusion coefficient, $\hat{\tau}$ is the tortuosity of medium, $\hat{\alpha}_L^T$ is the dispersivity that depends upon composition, $\hat{\alpha}_L$ is the dilute limit dispersivity, $\hat{\gamma}^{\overline{\overline{Aw}}}$ is an activity coefficient, $\hat{\mu}_0$ is the dilute viscosity, MW denotes the molecular weight, A and B are species indexes, $\hat{\beta}_i^T$ are constant model coefficients, and $m^{\overline{\overline{Aw}}}$ is the molality of species A. A term related to a gradient in pressure has been found to be small and dropped (Weigand et al., 2018b).

The auxiliary conditions for the TCAT non-dilute model are

$$\omega^{A\,\overline{w}}(z\in\Omega, t=0) = \omega_{\text{res}}^{A\overline{w}} \,, \tag{3.39}$$

$$p^w(z\in\Omega, t=0) = \rho_{\text{res}}^w g(L-z) \,, \tag{3.40}$$

$$\epsilon^{\overline{\overline{w}}}\rho^w v^{\overline{w}}(z=0, t>0) = \frac{Q\rho_{\text{in}}^w}{A} \,, \tag{3.41}$$

$$F^{\overline{\overline{Aw}}}(z=0, t>0) = \frac{Q}{A}\rho_{\text{in}}^w\omega_{\text{in}}^{A\overline{w}} \,, \tag{3.42}$$

$$p^w(z=L, t>0) = 0 \,, \tag{3.43}$$

and

$$\left.\frac{\partial \omega^{A\,\overline{w}}}{\partial z}\right|_{z=L,t>0} = 0 \ , \tag{3.44}$$

where the spatial domain is $\Omega = [0, L]$, the subscript res denotes a constant resident value, the subscript in denotes a constant value of the displacing fluid, Q is a volumetric flow rate coming into the domain, which has cross-sectional area A, and $F^{\overline{\overline{Aw}}}$ is the total advective and dispersive flux, which is equivalent to the sum of the terms that are differentiated with respect to z in Eqn (3.34)—the advective term within the parenthesis on line 1, and the two dispersive terms within brackets on lines 2 and 3.

3.4.2 Dilute Species Transport Model

As the species concentration becomes vanishingly small, the density, viscosity, and activity are no longer dependent on the species concentration. In this limit, the conservation of mass equation for the water phase becomes

$$\frac{\partial}{\partial z}\left[\frac{\hat{k}\rho^{w}}{\hat{\mu}}\left(\frac{\partial p^{w}}{\partial z}+\rho^{w}g\right)\right] = 0 \ , \tag{3.45}$$

and the conservation of mass equation for species A becomes

$$\frac{\partial\left(\epsilon^{\overline{\overline{w}}}\omega^{A\,\overline{w}}\right)}{\partial t}+\frac{\partial}{\partial z}\left(\epsilon^{\overline{\overline{w}}}\omega^{A\,\overline{w}}v^{\overline{w}}\right)-\frac{\partial}{\partial z}\left[\epsilon^{\overline{\overline{w}}}\left(\frac{\hat{D}_0}{\hat{\tau}}+\hat{\alpha}_L v^{\overline{w}}\right)\frac{\partial\omega^{A\,\overline{w}}}{\partial z}\right] = 0 \ , \tag{3.46}$$

where the dissipative term related to the gradient of the activity is zero, the diffusion coefficient is constant, and the dispersivity is the dilute dispersivity. The dilute form of the species transport equation has a constant, linear diffusion coefficient as opposed to the nonlinear non-dilute form. The conservation of mass for the water phase is no longer a function of the species concentration, thus the flow and transport equations are uncoupled.

3.4.3 Entropy Production Rates

The entropy density production rate is formulated to guide model closure in the TCAT approach, and this inequality is used to ensure the derived closure relations are consistent with the second law of thermodynamics. The non-dilute TCAT entropy production rate is (Weigand et al., 2018b)

$$\Lambda = \frac{1}{\theta^{\overline{\overline{w}}}}\frac{\hat{\mu}}{\hat{k}}\left(\epsilon^{\overline{\overline{w}}}v^{w}\right)^{2}+\frac{\epsilon^{\overline{\overline{w}}}\rho^{w}R_G}{\omega^{A\,\overline{w}}\omega^{B\,\overline{w}}}\left(\frac{\hat{D}_{Aw}}{\hat{\tau}}+\hat{\alpha}_L^{T}v^{\overline{w}}\right)\times$$

$$\left(\frac{MW_B}{MW_A MW_W}\right)\left(\frac{MW_W}{MW_B}\frac{\partial \omega^{A\,\overline{w}}}{\partial z}+\frac{\omega^{A\,\overline{z}}}{\hat{\gamma}^{\overline{\overline{Aw}}}}\frac{\partial \hat{\gamma}^{\overline{\overline{Aw}}}}{\partial z}\right)^2 , \tag{3.47}$$

where Λ is the entropy density production rate, $\theta^{\overline{\overline{w}}}$ is the temperature, assumed constant in this work, and R_G is the universal gas constant. The entropy density production rate has an advective and dispersive component, which must each be greater than or equal to zero. Note that this entropy density production rate is only valid under the assumptions made within this model formulation.

In the dilute limit, the entropy density production rate simplifies to

$$\Lambda=\frac{1}{\theta^{\overline{\overline{w}}}}\frac{\hat{\mu}}{\hat{k}}\left(\epsilon^{\overline{\overline{w}}}v^{w}\right)^2+\frac{\epsilon^{\overline{\overline{w}}}\rho^{w}R_G}{\omega^{A\,\overline{w}}\omega^{B\,\overline{w}}MW_A}\left(\frac{\hat{D}_0}{\hat{\tau}}+\hat{\alpha}_L v^{\overline{w}}\right)\left(\frac{\partial \omega^{A\,\overline{w}}}{\partial z}\right)^2 . \tag{3.48}$$

3.5 Solution Approach

3.5.1 Finite Element Formulation

For the weak formulation of the governing equations, we define $V \equiv H^1(\Omega)$, where $H^1(\Omega)$ is the standard Sobolev space defined over the spatial domain Ω. Showing the formulation for the more complex TCAT non-dilute model, we multiply the governing equations (Equations A.132 and 3.34) by the test functions, integrate over the domain, and impose the boundary conditions. We then seek a solution of determining $\left(p^{w},\omega^{A\,\overline{w}}\right)\in V\times V$

$$\begin{aligned}\left(\frac{\partial\left(\epsilon^{\overline{\overline{w}}}\rho^{w}\right)}{\partial t},v\right)_{\Omega}-\left(\frac{\hat{k}\rho^{w}}{\hat{\mu}}\left(\frac{\partial p^{w}}{\partial z}+\rho^{w}g\right),\frac{\partial v}{\partial z}\right)_{\Omega}\\ =\left\langle\frac{Q}{A}\rho^{w}_{\text{in}},v\right\rangle_{\Gamma_0}\quad\forall v\in V\end{aligned} \tag{3.49}$$

$$\begin{aligned}&\left(\frac{\partial\left(\epsilon^{\overline{\overline{w}}}\rho^{w}\omega^{A\,\overline{w}}\right)}{\partial t},v\right)_{\Omega}+\left(\epsilon^{\overline{\overline{w}}}\rho^{w}\omega^{A\,\overline{w}}v^{\overline{w}}-\epsilon^{\overline{\overline{w}}}\rho^{w}D,\frac{\partial v}{\partial z}\right)_{\Omega}\\ &=\left\langle\frac{Q}{A}\rho_{\text{in}}\omega_{\text{in}},v\right\rangle_{\Gamma_0}+\left\langle\frac{Q}{A}\rho_{\text{in}},v\right\rangle_{\Gamma_0}\quad\forall v\in V ,\end{aligned} \tag{3.50}$$

where $(\ ,\ )_\Omega$ and $\langle\ ,\ \rangle$ represent the standard inner products over $L_2(\Omega)$, and Γ_0, respectively. In our case, the inflow boundary, Γ_0 is simply the point $z = 0$ and

$$D = \left(\frac{\hat{D}_{Aw}}{\hat{\tau}} + \hat{\alpha}_L^T v^{\overline{w}}\right)\frac{\partial \omega^{A\,\overline{w}}}{\partial z} + \left(\frac{\omega^{A\,\overline{w}}}{\hat{\gamma}^{\overline{\overline{AW}}}}\right)\left(\frac{MW_B}{MW_W}\right)\left(\frac{\hat{D}_{Aw}}{\hat{\tau}} + \hat{\alpha}_L^T v^{\overline{w}}\right)\frac{\partial \hat{\gamma}^{\overline{\overline{Aw}}}}{\partial z}\ . \tag{3.51}$$

For our finite element discretization, we first define a computational mesh $\mathcal{M}_h = \{\Omega_k\}$, where $\Omega = \cup_{k=1}^{N_h}\Omega_k$. We use conforming piecewise linear Galerkin spaces defined as

$$V_h = \left\{v_h \in V \cap C^0(\Omega) : v_h|_{\Omega_k} \in P^1(\Omega_k)\right\}\ . \tag{3.52}$$

where $P^1(\Omega_k)$ denotes first order Lagrange polynomials, and seek the solution of $(\hat{p}, \hat{\omega}) \in V_h \times V_h$. The two governing equations are solved as decoupled PDEs. The velocity is determined through Equation A.132, however the mass fraction for the velocity calculation is always taken from the previous timestep, so the velocity is not a function of the mass fraction when solving the species transport equation. For the non-dilute model, spurious currents can form as result of using similar basis functions for the pressure and species mass fraction as only the gradient of the pressure appears in the the conservation of mass equation for the phase. To combat this, the approach by (Knabner and Frolkovic, 1996) is used to ensure a consistent velocity.

3.5.2 TCAT Viscosity Method

To utilize the TCAT SEI, we first convert the species transport equation to a hyperbolic form, which we do by way of operator splitting. Our splitting approaches are detailed in sections 3.5.3 and 3.5.4. With operator splitting, the advective portion of the equation becomes

$$\frac{\partial\left(\epsilon^{\overline{\overline{w}}}\rho^w\omega^{A\,\overline{w}}\right)}{\partial t} + \frac{\partial}{\partial z}\left(\epsilon^{\overline{\overline{w}}}\rho^w\omega^{A\,\overline{w}}v^{\overline{w}}\right) = 0\ . \tag{3.53}$$

To deal with the nonlinear form of the density, we utilize the conservation of mass equation for the water phase to transform the equation to the following non-conservative form

$$\epsilon^{\overline{\overline{w}}}\rho^{w}\frac{\partial\omega^{A\,\overline{w}}}{\partial t}+\epsilon^{\overline{\overline{w}}}\rho^{w}v^{\overline{w}}\frac{\partial\omega^{A\,\overline{w}}}{\partial z}=0\ . \tag{3.54}$$

As our governing equation is not in a conservative form nor is it a truly hyperbolic equation, the EV approach is not strictly suitable. However, we use some of the key features for our scheme.

To lay out our discrete approximation, we define ϕ_i, $i=1,\ldots,N_{dof}$ as our global basis functions for the space V_h. We label the support of ϕ_i as S_i and $S_{ij}=S_i\cap S_j$. The indices of shape functions that are non-zero over a region S are defined as $I\left(S\right)$. We also define an approximation of $\omega^{A\,\overline{w}}\approx\omega_h=\sum_{i\in N_{dof}}\phi_i\omega_i$. We seek to find $\omega_h\in V_h$ such that

$$m_i\frac{\partial\omega_h}{\partial t}+\sum_{j\in I(S_i)}K_{ij}^{I}\omega_j^{n}+\int_{\Gamma_0}\frac{Q}{A}\rho_{\text{in}}\omega_{\text{in}}\phi_i\,\mathrm{d}z=0;\forall i\in I\left(S_i\right)\ , \tag{3.55}$$

with

$$m_i=\int_{S_i}\epsilon^{\overline{\overline{w}}}\rho^{w}\phi_i\,\mathrm{d}z\ , \tag{3.56}$$

$$K_{ij}^{I}=-\int_{S_{ij}}\epsilon^{\overline{\overline{w}}}\rho^{w}v^{\overline{w}}\phi_j\frac{\partial\phi_i}{\partial z}\,\mathrm{d}z\ . \tag{3.57}$$

As with the EV scheme (Guermond et al., 2018), we introduce a low-order viscosity approximation

$$m_i\frac{\partial\omega_h}{\partial t}+\sum_{j\in I(S_i)}\left(K_{ij}^{I}+d_{ij}^{L,n}\right)\omega_j^{n}+\int_{\Gamma_0}\frac{Q}{A}\rho_{\text{in}}\omega_{\text{in}}\phi_i\,\mathrm{d}z=0;\forall i\in I\left(S_i\right)\ , \tag{3.58}$$

where

$$d_{ij}^{L,n}=\max\left(\left|K_{ij}^{I}\right|,\left|K_{ji}^{I}\right|\right)\ . \tag{3.59}$$

This low order viscosity approximation is a local extrema diminishing (LED) scheme (Kuzmin and Turek, 2002). While this form does reduce oscillations and is the equivalent of first-order upwinding in some cases, it is not strictly maximum principle preserving (Guermond et al., 2018). Accuracy is often lost with the introduction of the dissipative operator due to the addition of too much artificial viscosity.

To achieve higher rates of convergence, a higher order viscosity can be formulated based on an entropy residual. As a point of reference, we briefly consider the generic hyperbolic equation

$$\frac{\partial \omega}{\partial t} + \frac{\partial f(\omega)}{\partial z} = 0 \ . \tag{3.60}$$

To define an entropy-residual based viscosity using the scheme presented by (Guermond and Popov, 2017), first define the Galerkin solution at time step $n+1$, ω_g^{n+1}, as the solution to the following problem

$$\int_\Omega \left[\frac{\omega_g^{n+1} - \omega_h^n}{\Delta t} + \frac{\partial f\left(\omega_h^n\right)}{\partial z} \right] v \, \mathrm{d}\mathfrak{r} \quad \forall v \in V \ , \tag{3.61}$$

where ω_h^n is the solution from time step n. The entropy residual (R) for Equation 3.60, given an entropy pair (η, F), is defined as

$$R(u) = \frac{\partial \eta(\omega)}{\partial t} + \frac{\partial F(\omega)}{\partial z} \leq 0 \ , \tag{3.62}$$

where η is a convex entropy function and $F\left(\omega\right) = \int_0^s \eta'\left(s\right) f'\left(s\right) \mathrm{d}s$. The entropy residual at the nodal values (R_i^n) can be approximated as

$$R_i^n = \frac{2}{\Delta \eta_i} \int_\Omega \left(\frac{\omega_g^n - \omega_h^n}{\Delta t} + f'\left(\omega_h^n\right) \frac{\partial \omega_h^n}{\partial z} \right) \eta'\left(\omega_h^n\right) \phi_i \, \mathrm{d}\mathfrak{r} \ , \tag{3.63}$$

with $\Delta \eta_i = \eta_i^{\max} - \eta_i^{\min}$ and

$$\eta_i^{\max} = \max_{j \in I(i)} \left| \eta\left(\omega_i^n\right) \right| \ , \tag{3.64}$$

$$\eta_i^{\min} = \min_{j \in I(i)} \left| \eta\left(\omega_i^n\right) \right| \ . \tag{3.65}$$

The entropy-residual based viscosity is then defined as

$$d_{ij}^{EV,n} = \max\left(\left| R_i^n \right|, \left| R_j^n \right| \right) \ . \tag{3.66}$$

For the TCAT viscosity approach, we instead formulate the entropy residual directly from the TCAT entropy production rate,

$$\hat{R}_i^n = c_E \frac{h_e}{\Delta t} \frac{\Lambda_i^n}{\Delta \Lambda^n} \tag{3.67}$$

where $\Delta\Lambda^n = \Lambda^n_{\max} - \Lambda^n_{\min}$ and $\Lambda^n_{\max} = \max_i \Lambda^n$ and $\Lambda^n_{\min} = \min_i \Lambda^n$, h_e is the grid spacing, and c_E is a dimensionless scaling parameter. The TCAT entropy viscosity dissipative operator is defined as as the maximum of the nodal TCAT entropy residual $\hat{R}^n_i$

$$\hat{d}^{EV,n}_{ij} = \max\left(\left|\hat{R}^n_i\right|, \left|\hat{R}^n_j\right|\right) \ . \tag{3.68}$$

Our higher order viscosity approximation is then formulated as

$$\sum_{j\in I(S_i)} M_{ij}\frac{\partial \omega_j}{\partial t} = \sum_{j\in I(S_i)} \left(K^I_{ij} + d^{H,n}_{ij}\right)\omega^n_j + \int_{\Gamma_0} \frac{Q}{A}\rho_{\text{in}}\omega_{\text{in}}\phi_i \,\mathrm{d}z = 0; \forall i \in I\left(S_i\right) \ , \tag{3.69}$$

where we use the consistent mass matrix defined as

$$M_{ij} = \int_\Omega \epsilon^{\overline{\overline{w}}}\rho^w \phi_i\phi_j \,\mathrm{d}z \ , \tag{3.70}$$

and

$$d^{H,n}_{ij} = \min\left(d^{L,n}_{ij}, \hat{d}^{EV,n}_{ij}\right) \ . \tag{3.71}$$

For the EV formulation presented by (Guermond and Popov, 2017), the higher order viscosity approximation selects from $d^{EV,n}_{ij}$, as opposed to the TCAT entropy viscosity dissipative operator $\hat{d}^{EV,n}_{ij}$. The higher order artificial dissipative operator selects the minimum of the low-order dissipative operator or the entropy viscosity dissipative operator. The entropy viscosity dissipative operator is motivated by the fact that that entropy production increases at sharp fronts and shocks in hyperbolic problems.

3.5.3 Dilute Model

For this work, the incoming mass flow rate and permeability of the porous medium are constant. For the dilute case, the result is a constant velocity of the water phase for all time and space. To solve the species transport equation, we take three different decoupling/operator splitting approaches, all of which decouple the flow and transport equations. Additionally, the flow equation is only solved once as it is not a function of the salt mass fraction.

The first approach solves the species transport equation with standard Galerkin finite elements without any stabilzation or numerical viscosity. We refer to this model as unsplit. With the next two approaches we use operator splitting to separate the advective and dispersive operators of the transport equation. This allows us to tailor the numerical approximation to the operator. For sake of notation, we present Equation 3.46 in operator form as

$$\frac{\partial\left(\epsilon^{\overline{\overline{w}}}\omega^{A\,\overline{w}}\right)}{\partial t} = A_D(\omega^{A\,\overline{w}}) + D_D(\omega^{A\,\overline{w}}) \;, \tag{3.72}$$

where A_D represent the dilute advective operator and D_D the dilute dispersive operator. For the second approach, we use the sequential split operator approach, which has a splitting error $\mathcal{O}\left(\Delta t\right)$, requires two solves for each time step, and each operator uses the previous solution as its initial conditions (Kanney et al., 2002). This takes the form of

$$\begin{aligned}
&1.\;\; \frac{\partial(\epsilon\tilde{\omega})}{\partial t} = A_D(\tilde{\omega}) \text{ for } t \in [t, t+\Delta t] \\
&\qquad\qquad \text{where } \tilde{\omega} = \omega(z,t) \qquad (3.73) \\
&2.\;\; \frac{\partial(\epsilon\omega)}{\partial t} = D_D(\omega) \text{ for } t \in [t, t+\Delta t] \\
&\qquad\qquad \text{where } \omega = \tilde{\omega}(z, t+\Delta t) \;, \qquad (3.74)
\end{aligned}$$

where this is repeated for every time step and we use Equation 3.39 as initial conditions.

For the third and final formulation we use the alternating split operator approach, which has splitting error that is $\mathcal{O}\left(\Delta t^2\right)$ and requires three solves for each time step (Kanney et al., 2002). For each time step we solve the transport equation as

$$\begin{aligned}
&1.\;\; \frac{\partial(\epsilon\tilde{\omega})}{\partial t} = A_D(\tilde{\omega}) \text{ for } t \in [t, t+\Delta t/2] \\
&\qquad\qquad \text{where } \tilde{\omega} = \omega(z,t) \qquad (3.75) \\
&2.\;\; \frac{\partial(\epsilon\hat{\omega})}{\partial t} = D_D(\hat{\omega}) \text{ for } t \in [t, t+\Delta t] \\
&\qquad\qquad \text{where } \hat{\omega} = \tilde{\omega}(z, t+\Delta t/2) \qquad (3.76) \\
&3.\;\; \frac{\partial(\epsilon\omega)}{\partial t} = A_D(\omega) \text{ for } t \in [t+\Delta t/2, t+\Delta t] \\
&\qquad\qquad \text{where } \omega = \hat{\omega}(z, t+\Delta t) \;. \qquad (3.77)
\end{aligned}$$

Using the split operator approach, we can choose our numerical approximation to suit each operator. For the advection solve, we can use higher order techniques, such as the methods described above, to improve the accuracy of our solutions.

3.5.4 Non-Dilute Model

For the dilute flow and transport model, we decoupled the flow and transport equations. For the non-dilute flow and transport equations, we are unable to do so as the density and viscosity both appear in the conservation of mass equation for the water phase and are functions of the salt mass fraction. As with the dilute model, we examine three different operator splitting approaches. We first define a new operator for Equation A.132 as

$$\frac{\partial\left(\epsilon^{\overline{\overline{w}}}\rho^{w}\right)}{\partial t} = F_T(p^w, \omega^{A\,\overline{w}}) \tag{3.78}$$

and for Equation 3.35, where we consider the non-conservative form

$$\epsilon^{\overline{\overline{w}}}\rho^{w}\frac{\partial\omega^{A\,\overline{w}}}{\partial t} = A_T(p^w, \omega^{A\,\overline{w}}) + D_T(p^w, \omega^{A\,\overline{w}}) \ , \tag{3.79}$$

where D_T consists of the flux terms related to both the mass fraction and activity and A_T is the advective term. Note that the three operators are nonlinear functions of both the pressure and the salt mass fraction, our two dependent variables.

In the first approach, we decouple the flow and transport equations and solve them sequentially using standard Galerkin finite elements. We refer to this as the unsplit approach and again note that the flow and transport equations are decoupled for all three implementations. For the second approach, we use use a sequential split operator for the transport equation. For every time step, we solve the equations in the following order

$$\begin{aligned} &1.\ \frac{\partial(\epsilon\rho)}{\partial t} = F_T(p,\omega) \text{ for } t \in [t, t+\Delta t] \\ &\qquad \text{where } p = p(z,t) \text{ and } \omega = \omega(z,t) \end{aligned} \tag{3.80}$$

$$\begin{aligned} &2.\ \epsilon\rho\frac{\partial\tilde{\omega}}{\partial t} = A_T(p,\tilde{\omega}) \text{ for } t \in [t, t+\Delta t] \\ &\qquad \text{where } p = p(z,t+\Delta t) \text{ and } \tilde{\omega} = \omega(z,t) \end{aligned} \tag{3.81}$$

3. $\epsilon\rho\dfrac{\partial\omega}{\partial t} = D_T(p,\omega)$ for $t \in [t, t+\Delta t]$

$$\text{where } p = p(z, t+\Delta t) \text{ and } \omega = \tilde{\omega}(z, t+\Delta t)\ , \tag{3.82}$$

where Equations 3.39 and 3.40 are used for the initial conditions for $p(z,0)$ and $\omega(z,0)$.

For the final approach, we use a variation of the alternating split-operator approach with the following form, that is solved for every time step

1. $\dfrac{\partial(\epsilon\rho)}{\partial t} = F_T(\tilde{p},\omega)$for $t \in [t, t+\Delta t/2]$

$$\text{where } \tilde{p} = p(z,t) \text{ and } \omega = \omega(z,t) \tag{3.83}$$

2. $\epsilon\rho\dfrac{\partial\tilde{\omega}}{\partial t} = A_T(\tilde{p},\tilde{\omega})$for $t \in [t, t+\Delta t/2]$

$$\text{where } \tilde{p} = \tilde{p}(z, t+\Delta t/2) \text{ and } \tilde{\omega} = \omega(z,t) \tag{3.84}$$

3. $\epsilon\rho\dfrac{\partial\hat{\omega}}{\partial t} = D_T(\tilde{p},\hat{\omega})$for $t \in [t, t+\Delta t]$

$$\text{where } \tilde{p} = \tilde{p}(z, t+\Delta t/2) \text{ and } \hat{\omega} = \tilde{\omega}(z, t+\Delta t/2) \tag{3.85}$$

4. $\epsilon\rho\dfrac{\partial\omega}{\partial t} = A_T(\tilde{p},\omega)$for $t \in [t+\Delta t/2, t+\Delta t]$

$$\text{where } \tilde{p} = \tilde{p}(z, t+\Delta t/2) \text{ and } \omega = \hat{\omega}(z, t+\Delta t) \tag{3.86}$$

5. $\dfrac{\partial(\epsilon\rho)}{\partial t} = F_T(p,\omega)$for $t \in [t+\Delta t/2, t+\Delta t]$

$$\text{where } p = \tilde{p}(z, t+\Delta t/2) \text{ and } \omega = \omega(z, t+\Delta t)\ . \tag{3.87}$$

In this approach, the splitting of the transport equation solves is identical to the dilute transport solve with the difference being that the pressure and in turn the velocity is solved over a half time step. The flow equation is also split but steps 1 and 5 can be combined into a single step after the first solve.

3.5.5 Implementation Details

All of the models were implemented in the open source finite element software package Proteus (https://proteustoolkit.org). Linear basis functions were used for both the pressure and species mass fraction for all versions. Newton's method was used as the nonlinear solver and LU decomposition as the linear solver, to eliminate any errors due to the linear solver choice. Implicit Euler was used for

time integration for the flow equation and for the dispersion solves when operator splitting was used. No stabilization schemes were used for these two operators.

For the advective operator, a standard Galerkin approach (CG), a local extremum diminishing approach for artificial viscosity (AV), and the TCAT entropy-based viscosity approach were examined. For comparison in some cases, we consider the EV scheme by treating the advection equation as a nonlinear scalar PDE without reference to the other components of the full transport system. The entropy function considered with this approach was the power function, the most common in the literature, which can be written as

$$\eta(\omega^{A\,\overline{w}}) = \frac{1}{2}\omega^{A\,\overline{w}2} \; . \tag{3.88}$$

Explicit Euler time integration was used for the advective operator solves. The time step was controlled by the CFL number for all three operators. The max CFL number was 0.125 for the dilute model and 0.25 for the non-dilute model.

Dense grid solutions were found for both the dilute and non-dilute code with an existing spatially adaptive cell-centered finite difference code (Weigand et al., 2018b). This code was also compared to the analytical solution for the dilute model and was in agreement. All parameters found in (Weigand et al., 2018b) were used and for the non-dilute model, $\hat{\beta}_1^T = 2.53 \times 10^7$ and $\hat{\beta}_2^T = 1.31 \times 10^8$.

3.6 Results and Discussion

3.6.1 Dilute Species Transport

Four different Peclet numbers (Pe $= vL/D$) were examined by adjusting the longitudinal dispersivity producing a range of Pe from 66–2.1$\times 10^4$. For the TCAT viscosity approach, the tuning parameter c_E in Equation 3.67 was found by performing an optimization for each discretization that minimized the ℓ_2 error norm that was normalized by the degrees of freedom. The Nelder-Mead algorithm in the SciPy software package was used for the optimization (Virtanen et al., 2019).

Table 3.4 shows the average convergence rate for each approach examined. The alternating split-operator approach with the TCAT viscosity had the highest rate of convergence. An example of the error norms can be seen in Figure 3.8, which shows the error norm vs degrees of freedoms (DOFs)

for the highest Pe number for the alternating split operator approach. The convergence rate increases for the alternating split TCAT method as the Pe number increases, however the ℓ_2 error norm also increases as the Pe increases (Figure 3.9). The AV method added too much artificial viscosity to the solution and was always too diffuse as compared to the dense grid solution, while the CG approach had non-physical oscillations as no stabilization was used and the Pe_m ($\text{Pe}_m = vL/(D\Delta z)$) was greater than unity for all simulations except the most refined with the lowest Pe.

Table 3.4: Average Convergence Rate for the Dilute Simulations

	Unsplit	CG	AV	Power	TCAT
Sequential Rate	1.76	2.16	1.28	1.98	2.16
Alternating Rate		2.07	1.27	2.45	2.43

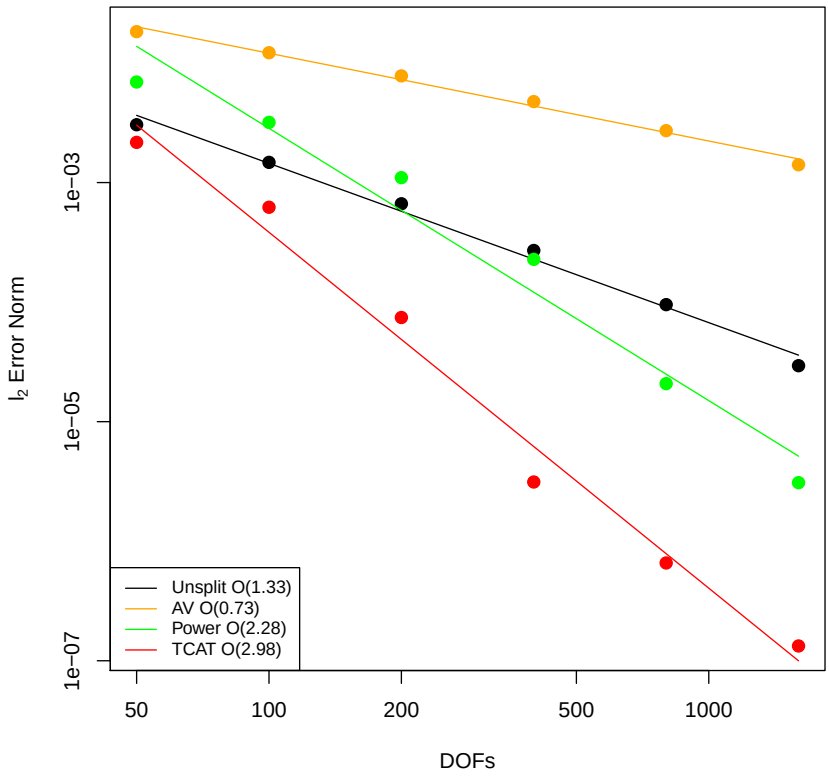

Figure 3.8: Convergence for the largest Pe and the alternating split-operator algorithm for the dilute model.

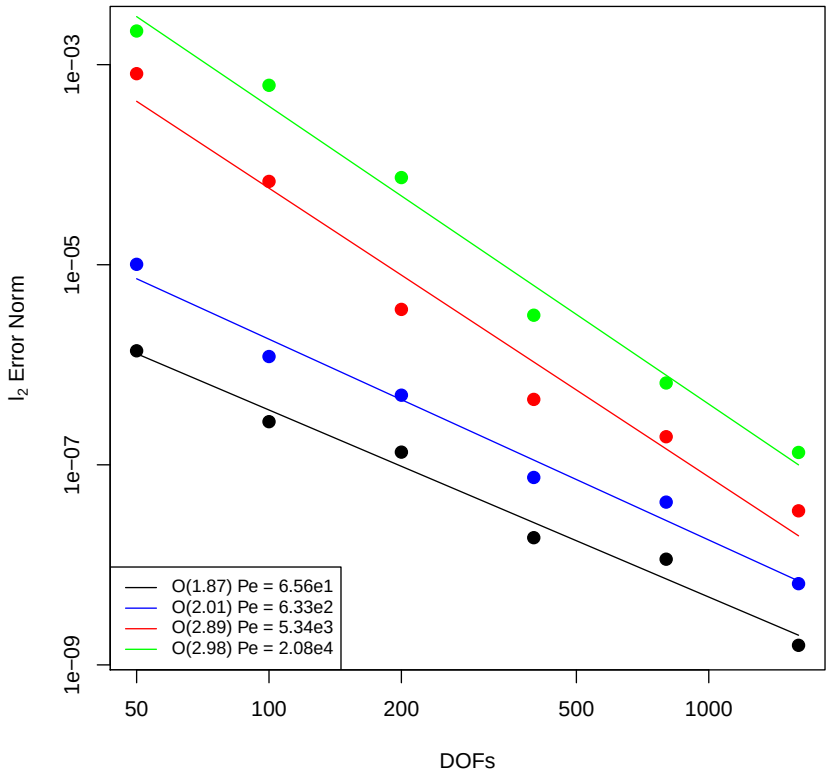

Figure 3.9: Convergence for the TCAT alternating split operator-approach for each Pe Number for the dilute model.

While the TCAT method produced the lowest errors and highest rates of convergence, the results are dependent on an optimized parameter. Figure 3.10 shows the optimized c_E parameter vs the Pe_m. For the higher Pe numbers, we see that the optimized c_E decreases as the mesh becomes more refined (and the Pe$_m$ decreases) meaning that less artificial viscosity is needed for an accurate solution. For the lowest Pe number simulation, the optimized c_E parameter increases as Pe$_m$ decreases. This result is counter intuitive but can be explained by examining the sensitivity of the solution on the c_E parameter.

To test the sensitivity of the solution on the c_E parameter, a simple naive average of the optimized values was found and the simulations were re-run using the average value (Figure 3.11). The two highest Pe number simulations are the most sensitive to the c_E parameter. The two lowest Pe number simulations are less sensitive to the c_E parameter as the solutions are fairly disperse and do not require much stabilization as the solution tends to not oscillate. For the optimizations, the initial guess for c_E

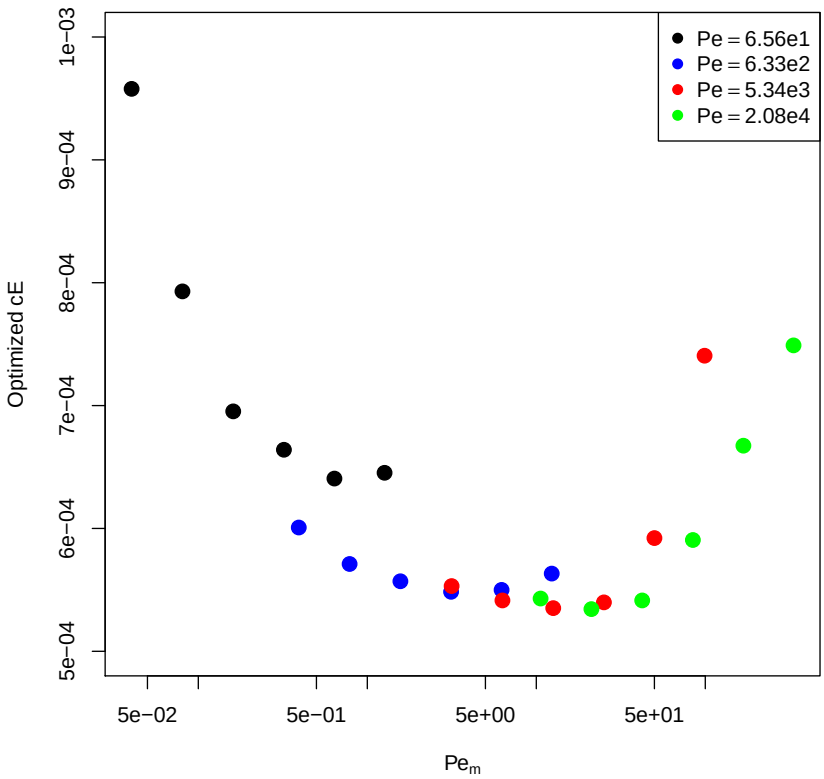

Figure 3.10: Optimized c_E for the TCAT alternating split-operator approach for the dilute model.

was 1.0×10^{-3}. Since the solutions for the low Pe numbers and low Pe_m simulations are relatively insensitive to c_E, the optimization quickly converges to a value close to the initial guess. To determine an optimal c_E for all simulations, the simulations with a higher Pe_m and higher Pe should be more heavily weighted to achieve even better agreement with the true solutions.

Noting, that for the dilute case, our transport model essentially reduces to conservative advective-diffusive transport, we next compare the TCAT entropy-based stabilization to an EV approximation (Guermond and Popov, 2017), in order to better understand its performance. Specifically, the nodal entropy residual (R) for both functions is examined (Figure 3.12). Loosely speaking, the objective with the use of entropy-based stabilization is to have non-zero contributions around sharp fronts, i.e. where the gradient of the solution is large, with values decreasing as the gradient's magnitude decreases. This is so that more artificial viscosity can be added near the sharp gradients to prevent oscillatory behavior while minimizing non-physical smearing away from the front. The TCAT approach's nodal entropy

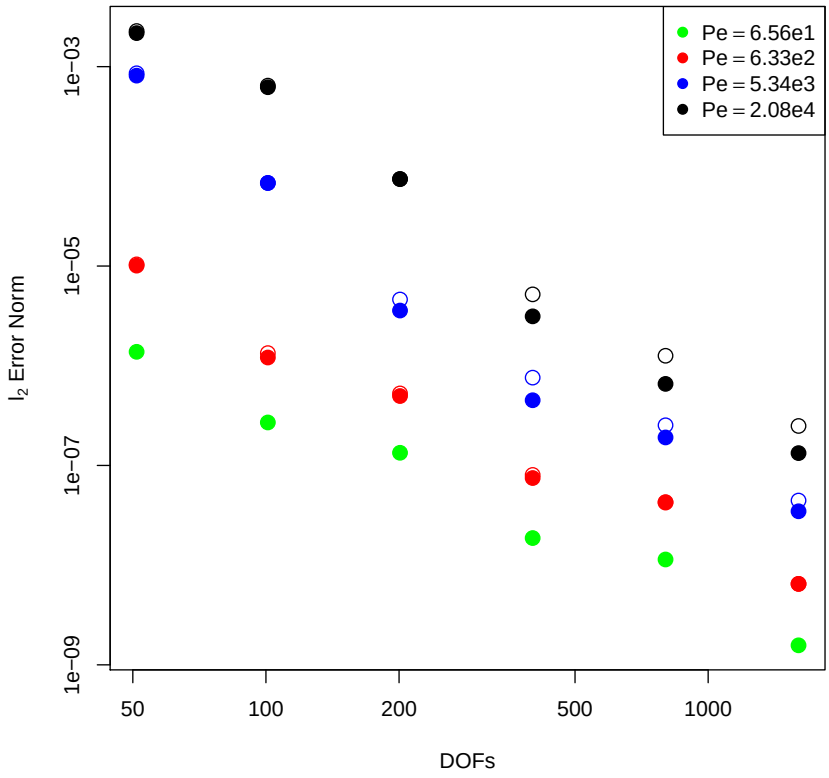

Figure 3.11: Error for the dilute TCAT approach with the alternating split-operator approach for optimized (filled circles) and averaged (non-filled circles) values of the c_E parameter vs the mesh Pe number.

residual has its maximum value at the inflection point of the mass fraction curve and decreases symmetrically away from this point. For the power function, the solution is too disperse, asymmetric, and the nodal entropy residual actually decreases near the inflection point. With the power function, the leading edge of the solution contains too much artificial viscosity and it appears that not enough artificial viscosity is being added to the trailing edge. Additionally, the less refined mesh has phase error with the power function that vanishes as the grid becomes more refined.

The key is that the TCAT entropy production rate is a function of the species mass fraction gradient, while the power entropy function is only dependent on the mass fraction and are not capable of describing the behavior of the species mass fraction gradient. In both approaches the nodal entropy residual decreases as the grid becomes more refined. For these simulations, the nodal entropy residual

is always less than the low order viscosity (d_{ij}^L) so the higher order viscosity approximation is always the minimum of the nodal entropy residual.

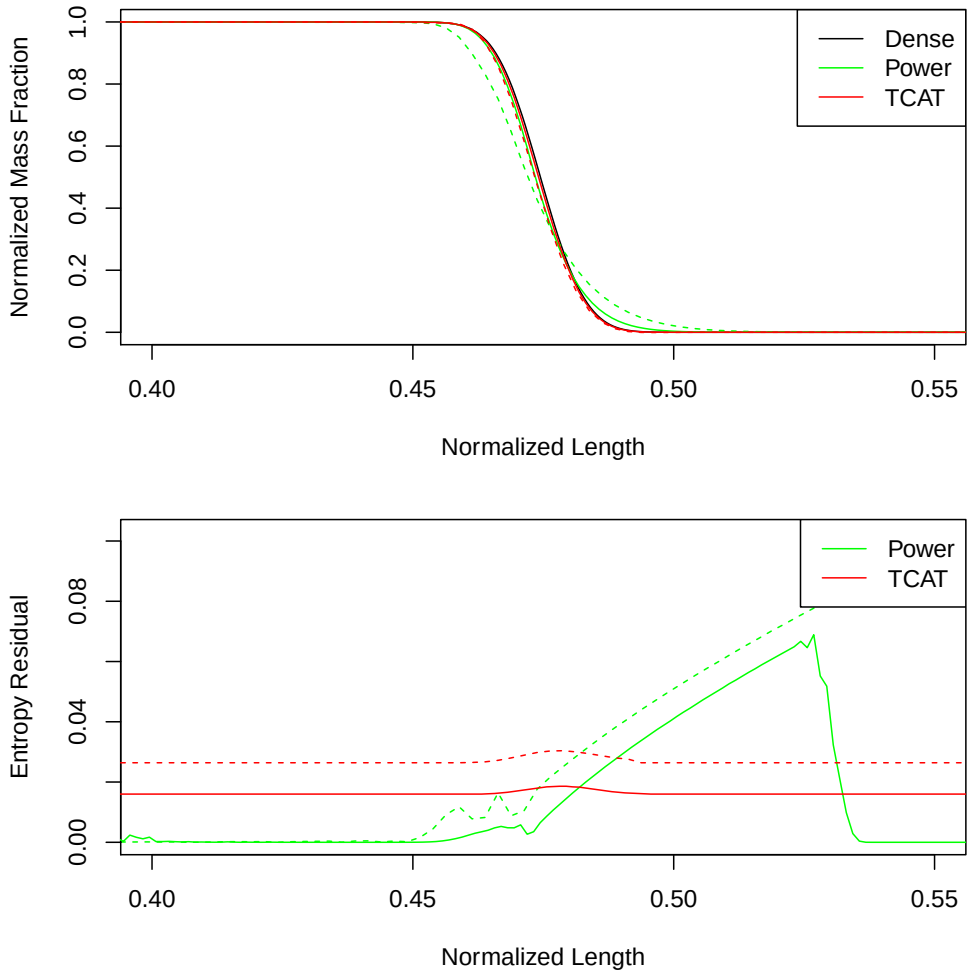

Figure 3.12: Solution and entropy residual (R) for the dilute model for the largest Pe using the alternating split-operator approach with 400 DOFs (dashed) and 800 DOFs (solid).

3.6.2 Non-Dilute Species Transport

For the TCAT non-dilute flow and transport model, six different experiments were considered and the dense grid solutions are shown in Figure 3.13. For the experiments with no salt initially present, the salt front sharpens as the incoming salt mass fraction increases. For the two experiments with a nonzero salt mass fraction initially present, the front is more disperse with the higher mass fractions. Additionally, the average velocity is slightly dependent on the incoming and resident mass fractions as the mass fraction profile curves do not all intersect at a normalized mass fraction of 0.5.

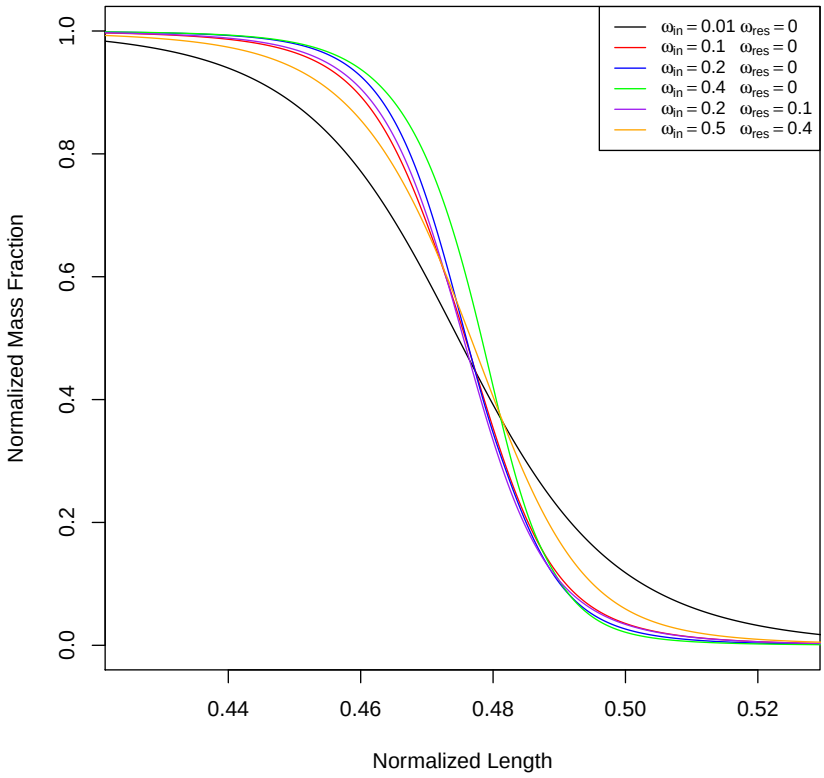

Figure 3.13: Dense grid solutions for the experiments considered for the TCAT non-dilute flow and transport model.

Average convergence rates for the non-dilute experiments are shown in Table 3.5 for all approaches considered. As with the dilute model, the TCAT viscosity approach has the highest rate of convergence as well as the lowest ℓ_2 error norms. While the sequential split-operator implementation for the TCAT viscosity had a slightly higher rate of convergence than the alternating split-operator approach, the alternating split-operator approach had lower ℓ_2 error norms. The CG methods rate of convergence is misleading as oscillations were present in the solution for multiple discretizations and this resulted in a higher convergence rate.

The convergence rates are a function of the non-linearity of the simulation. Figure 3.14 shows the ℓ_2 error norm vs DOFs for the alternating split TCAT viscosity approach. For the simulations with no salt initially present, the convergence rate decreases as the incoming salt mass fraction increase. While the experiment with $\omega_{\text{in}} = 0.5$ and $\omega_{\text{res}} = 0.4$, is the second most disperse experiment, the density, viscosity, and activity functions are highly nonlinear and this is reflected in the convergence rate. This

same trend can be seen with the sequential split-operator, TCAT-viscosity approach so it appears to not be a function of operator splitting.

Table 3.5: Average Convergence Rate for the Non-Dilute Simulations

	Unsplit	CG	AV	Power	TCAT
Sequential Rate	1.12	1.37	0.99	1.27	1.71
Alternating Rate		1.31	0.98	1.33	1.68

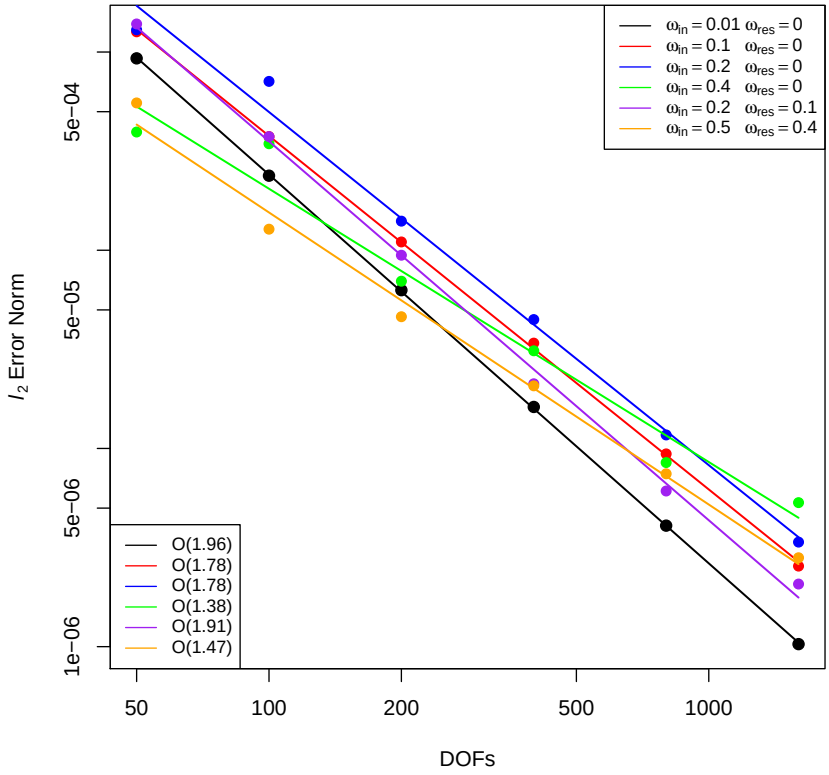

Figure 3.14: Convergence of the alternating split-operator, TCAT-viscosity approach for the non-dilute model.

As with the dilute model, the c_E parameter was optimized by minimizing the ℓ_2 error norm at each discretization and for every experiment. The same optimization scheme was used for the non-dilute case as with the dilute case. Figure 3.15 shows the optimized c_E for the alternating split-operator, TCAT-viscosity implementation. The general trend is that the value of c_E increases as the number of DOFs increases. This is counter intuitive. As the computational mesh becomes more re-

fined, less artificial viscosity should be needed. We see this trend however, because, the TCAT viscosity method is causing an over-sharpening of the solution and more artificial viscosity is adding more dispersion to the solution and thus is in better agreement with the dense-grid solutions.

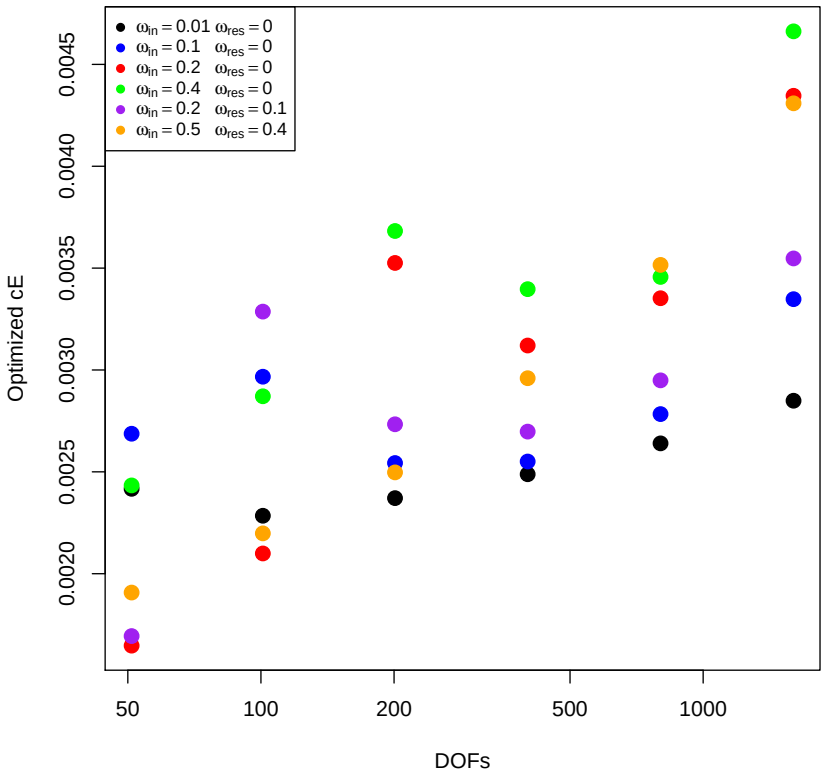

Figure 3.15: Optimized c_E for the alternating split-operator, TCAT-viscosity approach for the non-dilute model.

As was done previously, a simple average of the c_E parameter was calculated and used to re-run the simulations (Figure 3.16). The TCAT-viscosity approach is more dependent on the c_E value at fewer DOFs. Additionally, the sharper the front, the more dependent the solution is on the tuning parameter. In other words, the ℓ_2 error norm is greater for the sharper front experiments when the averaged c_E value is used. This is particularly noticeable at the most refined cases. As mentioned, the TCAT viscosity approach tends to over-sharpen the front and needs more artificial viscosity as the grid is refined and the average c_E value is less than the optimized values for these specific discretizations and experiments.

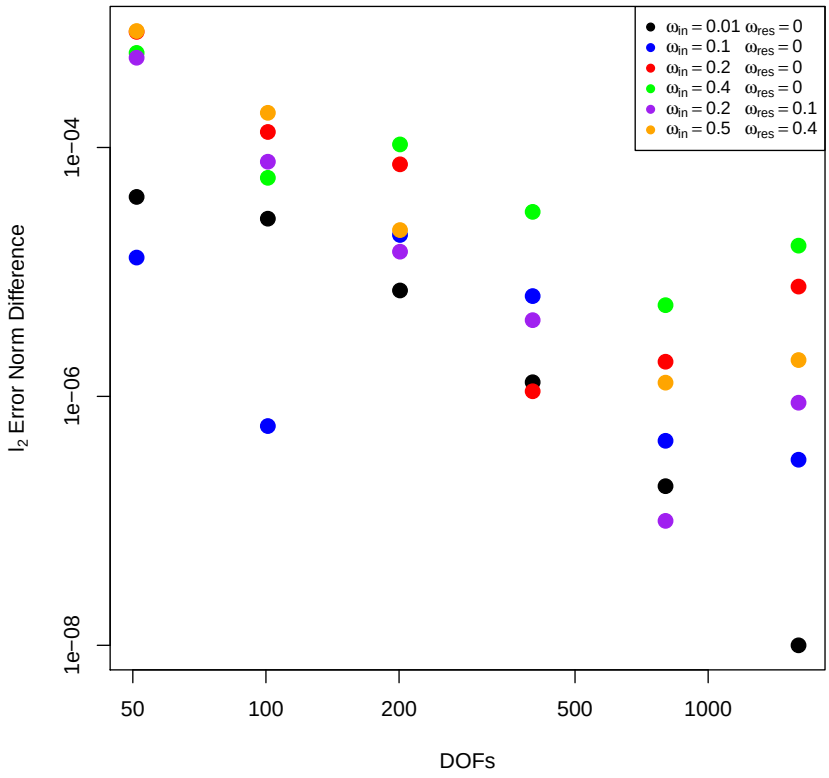

Figure 3.16: Difference between ℓ_2 error norms for optimized and averaged c_E for the alternating split-operator, TCAT-viscosity approach.

Figure 3.17 shows the solutions for each of the non-dilute displacements for the alternating split-operator case with 400 DOFs for the power function and the TCAT-viscosity approach. The power entropy function produces results that are too disperse and as the salt mass fraction increases the solutions becomes even more disperse, which is the opposite behavior that occurs with the actual solution. For the non-dilute experiments, we are not solving the conservative form of the advection equation, therefore there is no reasonable expectation for this formulation to be able to accurately simulate the dense grid solutions. For the TCAT viscosity, the solution is slightly sharper for every simulation except for the case when $\omega_{\text{in}} = 0.5$ and $\omega_{\text{res}} = 0.4$, but the results are in general agreement with the dense-grid solutions. Adding more artificial viscosity to the solution makes the TCAT-viscosity solutions more disperse, which occurs when c_E is increased, slight phase error is introduced. This produces a higher ℓ_2 error norm as opposed to an overly sharp solution that has no phase error, which is why the optimization yielded a sharper solution.

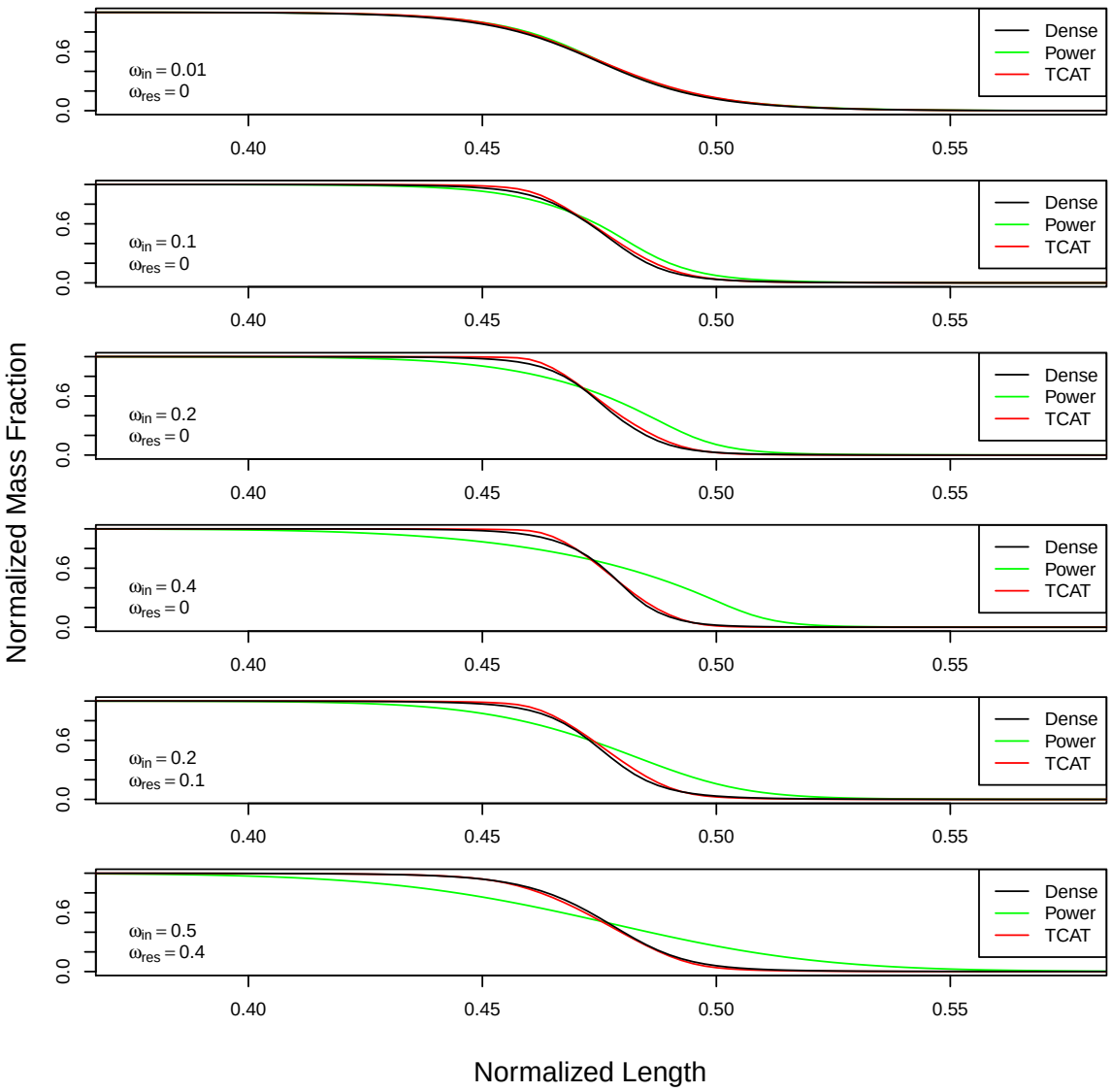

Figure 3.17: Solutions obtained using the alternating split-operator algorithm for both EV approaches with 400 DOFs.

To further determine the underlying behavior of the different entropy formulations, the nodal entropy residual (R) was examined (Figure 3.18). The power function does not do a good job of resolving the large gradient region. More artificial diffusion is added to the trailing portion of the front as opposed to the leading edge and this produces an asymmetric profile that does not match the dense grid solution.

The TCAT entropy function is a function of the gradient of the salt mass fraction, which is an advantage for the problems considered herein. For the TCAT approach, the entropy production rate is normalized by the maximum and minimum production rate through the entire system and not just locally. The non-dilute flow and transport model is known to produce asymmetric salt fronts (Weigand et al., 2018b), and the TCAT entropy production rate is also asymmetric where the leading edge has more entropy production than the trailing edge. Thus, less artificial viscosity is added to the trailing edge and we see over-sharpening. While only one experiment is shown for the entropy and residual, the same trend exists for all other experiments considered.

For these simulations, the maximum of the nodal entropy residual ($\hat{R}$) for the TCAT viscosity approach over the support of each element was always smaller than the lower order artificial viscosity (d^L), therefore the TCAT viscosity was always used for the higher order viscosity. The artificial viscosity was found to be of the same order of magnitude as the actual physical dispersion in the system. The relationship between the artificial viscosity and physical dispersion is inversely related. As the physical dispersion decreases, the artificial viscosity increase as the front becomes sharper.

Since TCAT has been used to formulate entropy production rates for several model hierarchies, it is reasonable to speculate that the advantages of using a physically based entropy production rate to guide artificial dissipation observed in this work could apply to other problems as well. The sort of problems where we envision this to be the case include species transport in multiphase flow and heat transport in single and two-fluid flow.

3.7 Conclusions

The following can be concluded from this analysis:

- The physically-based entropy production rate that comes from the TCAT approach for model development can be used to improve the accuracy of numerical approximations of the formulated model.

- The TCAT entropy viscosity approach for dilute flow and transport shows higher rates of convergence and lower ℓ_2 error norms as compared to the entropy viscosity approach.

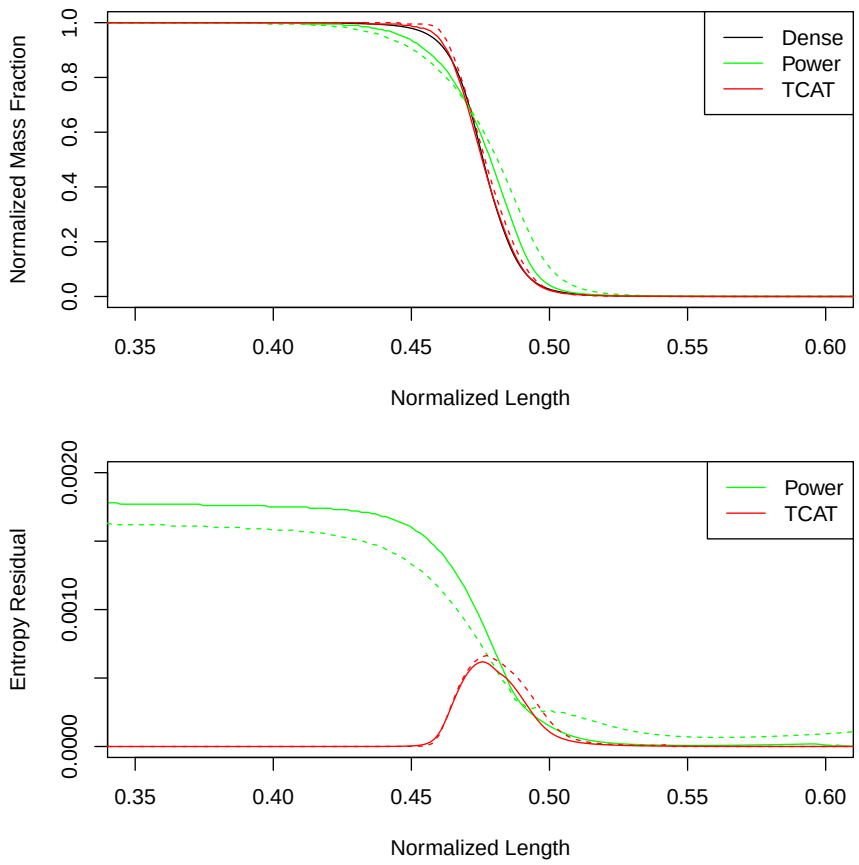

Figure 3.18: Solution and nodal entropy residual for an incoming mass fraction of 0.2 and pure water resident fluid for the alternating split-operator approach with 400 DOFs (dashed) and 800 DOFs (solid).

- For the non-dilute flow and transport model, the TCAT entropy viscosity approach also has higher convergence rates and lower error norms than unstabilized finite elements and a non-conservative form of the entropy viscosity method.
- The TCAT entropy viscosity method utilizing the physically-based entropy production rate is dependent on a fitted parameter, however, this value can be fit to a subset of the data and yield reasonable results for the rest of the dataset.
- The general framework of the TCAT viscosity approach can be applied to other models derived within the TCAT framework.

CHAPTER 4: MICROSCALE MODELING OF NON-DILUTE FLOW AND TRANSPORT

4.1 Introduction

Non-dilute solutions occur in a variety of porous medium physics applications, such as salt water intrusion, leachate transport, and density-motivated remediation strategies (Hill et al., 2001; Johnson et al., 2004; Miller et al., 2000). Species transport in such systems differs markedly from common dilute system. Macroscale mathematical models are used to represent the behavior of such systems in an averaged sense over a representative regions of the porous structure.

Laboratory experiments for non-dilute flow and transport in porous media are complicated and time consuming. Experimental work has consisted of column experiments where various fluids and salts are used to adjust density, viscosity, chemical activity, fluid velocities, and pore morphology and topology characteristics (Brigham et al., 1961; Slobod, 1964; Watson et al., 2002c; Weigand et al., 2018a). While these experiments provide insight on observed displacement patterns and solute profiles, it is difficult to extract a mechanistic understanding from the results due to the scale of the experiments and the complex and competing physical phenomena that are operative in such systems. An additional downside to such experimental work is the inability to isolate different physical phenomena, since such systems are constrained by the properties of the solutions investigated.

Attempts to model gravitationally-stable non-dilute flow and transport in porous media have represented limited sets of laboratory data (Watson et al., 2002c; Weigand et al., 2018a). However, these models are dependent on fitting parameters that are not firmly tied to underlying physical phenomena that impact the transport phenomena observed (Landman et al., 2007b; Watson et al., 2002c). Because our mechanistic understanding is lacking, extant modeling approaches are not rigorously predictive.

The use of highly resolved microscale, or pore scale, computational experiments is one approach at overcoming the drawbacks of traditional laboratory experiments and obtaining mechanistic insight (Gray and Miller, 2014). Microscale modeling can be used to simulate complex systems at a scale at which continuum mechanical models can be formulated rigorously and consistently with well-

understood physics. The results from such simulations can in turn be used to gain fundamental insight needed to advance, evaluate, and validate macroscale models that are needed for the size of typical applications of concern. Additionally, microscale computational approaches enable a fuller exploration of potential physical phenomena because individual model parameters can be isolated and controlled. Despite the apparent benefits of microscale modeling to advance understanding of non-dilute species transport in porous medium systems, such approaches have not been reported in the literature. A fundamental understanding of non-dilute flow and transport in porous media at all spatial scales is lacking, and the predictive capabilities of macroscale models for non-dilute transport are limited as a result.

4.2 Objectives

The goal of this to work is to advance mechanistic understanding of non-dilute flow and transport in porous medium systems. The specific objectives are: (1) to formulate and approximate a microscale non-dilute flow and transport model for porous media; (2) to examine microscale simulation results qualitatively and quantitatively to aid mechanistic understanding; (3) to upscale microscale simulation results and compare to extant experimental observations; and (4) to examine the effect of a set of physical phenomena on observed macroscale solute dispersion.

4.3 Background

The spatial scale of a mechanistic model is one of its defining features and determines the phenomena that need to be considered (Gray and Miller, 2014). For a porous medium system, the microscale (also known as the pore scale) is where the boundaries of all phases and interfaces are known in both space and time. The macroscale is defined as the scale at which a point is represented by an average over a region of the system that contains all phases present. The minimum size of such an averaging region, such that averaged quantities are insensitive with respect to changes in the size of the region, is termed a representative elementary volume (REV) (Bear, 1972). At the macroscale, variables such as porosity and volume fraction exist, both of which are ill-defined at the microscale. As a macroscale point is an average of the microscale behavior, the distribution of the underlying variable is lost. Due to the loss of information, underlying microscale transport phenomena may need to be parameterized in larger scale models. An example of this is the inclusion of mechanical dispersion in macroscale

species transport models to account for the varied movement of the species due to the microscale fluid phase velocity distribution (Bear, 1972).

Dilute microscale and macroscale fluid flow and species transport in porous media has been studied extensively and the use of microscale computational experiments is commonplace (Aramideh et al., 2018; Bijeljic and Blunt, 2007; Bijeljic et al., 2011, 2004, 2013; Crevacore et al., 2016; Icardi et al., 2014). Microscale simulations are frequently used to evaluate existing macroscale relationships for species transport (Bijeljic et al., 2004; Icardi et al., 2014), to investigate non-Fickian transport for various types of porous media (Aramideh et al., 2018; Bijeljic et al., 2013), or to improve understanding of subscale effects on observed macroscale behavior (Boccardo et al., 2014). Microscale simulations are preferred over laboratory experiments because the microscale flow field can be analyzed to better understand macroscale behavior. For example, the work of Aramideh et al. (2018) found flow conditions needed for the existence of recirculation zones for media comprised of overlapping spheres. These zones resulted in regions of negative velocities relative to the mean direction of flow and explained the observed non-Fickian behavior. Much of the research for microscale dilute flow and transport has focused on examining microscale velocity distributions and correlations to describe macroscale behavior (Aramideh et al., 2018; Bijeljic et al., 2013; Siena et al., 2014).

As compared to dilute flow and transport, microscale non-dilute flow and transport studies have been limited to the membrane literature (Gruber et al., 2011, 2016). Gruber et al. (2016) implemented a microscale model to assess impacts of concentration polarization on reverse osmosis and forward osmosis performance. The slightly compressible version of the Navier-Stokes equation were used to solve for the velocity field and the microscale transport equation was used to model the salt species. The impacts of non-dilute behavior, including the resulting velocity field distribution, were not discussed or analyzed.

The thermodynamically constrained averaging theory (TCAT) is a continuum mechanical approach for deriving mechanistic macroscale models by directly averaging microscale conservation and thermodynamic equations and closing the macroscale models using an entropy inequality (Gray and Miller, 2009, 2014). All variables, conservation equations, and thermodynamic laws are first written at the microscale and formal averaging approaches are used to derive the macroscale equations and variables. A constrained entropy inequality is formulated and used to guide model closure and ensure the resulting model obeys the second law of thermodynamics. TCAT models for single phase flow and

transport in porous media (Gray and Miller, 2006; Miller and Gray, 2008), non-dilute flow and transport in porous media (Gray and Miller, 2009; Weigand et al., 2018a) and two phase flow and transport in porous media have been developed (Jackson et al., 2009; Rybak et al., 2015). The TCAT approach also uses specific notation to discern between scales and types of averages. For this work, we follow the TCAT notation and note only that variables adorned with subscripts are microscale variables and macroscale variables are adorned with superscripts.

With the TCAT approach, variables across all possible scales are consistent, well-defined, and connected. Due to this, microscale simulations can be performed and the results may be averaged to examine larger scale variables and phenomena. This is known as subscale modeling and is an approach to validate models where experiments at the scale of the model are not required. The benefit of this approach is that the physics at the microscale are typically well-defined and understood and variables that can be difficult to analyze and isolate experimentally are more easily quantified. This approach has seen success in other application including two-fluid-phase flow in porous media (Bruning and Miller, 2019; Dye et al., 2016; McClure et al., 2017; Miller et al., 2019a).

The most successful attempts at modeling macroscale non-dilute flow and transport have extended Fick's law such that dispersion is a function of the composition (Demidov, 2006; Egorov et al., 2005; Gray and Miller, 2009; Hassanizadeh, 1990; Landman et al., 2007b; Watson et al., 2002c; Weigand et al., 2018a). Hassanizadeh (1990) first developed the nonlinear Fickian model, which is a Taylor expansion of Fick's law and includes a fitting parameter to account for non-dilute behavior. Weigand et al. (2018a) expanded on the nonlinear Fickian model by including activity impacts as well as an additional fitting parameter. This model was formulated with TCAT and outperformed the nonlinear Fickian model for the one dataset considered. However, the major drawback with these models is the lack of understanding of the mechanistic factors affecting the fitting parameters. The parameter in the nonlinear Fickian model has an exponential relation to the Darcy velocity but no fundamental mechanistic basis has been advanced to support the empirical form (Landman et al., 2007b; Schotting et al., 1999; Watson et al., 2002c). Applying the TCAT model to the same dataset used by Watson et al. (2002c) found a similar relationship where the fitting parameters were functions of the Darcy velocity (Weigand et al., 2017).

Mechanistic insight into macroscale non-dilute flow and transport is limited and has been provided solely from laboratory experiments with a limited number of salt species considered. Computational

experiments have also been performed but are fundamentally flawed as they solve the governing equations at the macroscale (Landman et al., 2007a; Welty and Gelhar, 1991). Furthermore, to simulate transport, the dilute form of Fick's law has been used despite attempting to gain insight on non-dilute flow and transport at the macroscale, where Fick's law has been shown to be invalid (Konz et al., 2009; Starr and Parlange, 1976; Watson et al., 2002c; Weigand et al., 2018a; Wright et al., 2009). From the laboratory experiments, we know that the salt species front tends to sharpen as compared to a dilute tracer under the same operating conditions. The sharpness of the salt mass fraction front, in response to a step change in salt mass fraction at the inflow boundary, has been shown to increase as the incoming mass fraction of the salt species increases. However, if a salt species is initially present in the porous medium, the difference between the displacing and displaced mass fraction affects the sharpness of the front (Weigand et al., 2018a). For a laboratory data set that used $CaBr_2$, chemical activity effects were found to be significant for constant density difference experiments (Weigand et al., 2018a). Additionally, laboratory experiments show that non-dilute displacements produce skewed breakthrough curves and they become more asymmetric as the mass fraction difference between the resident and displacing fluids increases (Weigand et al., 2018a). Mechanistic understanding of these macroscale experimental observations is lacking.

4.4 Model Formulation, Approximation, and Application

4.4.1 Microscale Model

Fluid flow was modeled at the microscale using the compressible Navier-Stokes equations (Gray and Miller, 2014). These equations consist of a conservation of mass equation and conservation of momentum equations both of which are written for the fluid phase. The conservation of mass equation is

$$\frac{\partial \rho_w}{\partial t} + \nabla \cdot (\rho_w \mathbf{v}_w) = 0 \ , \tag{4.89}$$

where ρ_w is the density, t is time, and $\mathbf{v}_w$ is the fluid phase velocity vector. The conservation of momentum equations for a compressible fluid with variable density and dynamic viscosity are

$$\frac{\partial}{\partial t} (\rho_w \mathbf{v}_w) + \nabla \cdot (\rho_w \mathbf{v}_w \mathbf{v}_w) - \nabla \cdot \left[\hat{\mu}_w \left(\nabla \mathbf{v}_w + \nabla \mathbf{v}_w^T - \frac{2}{3} (\nabla \cdot \mathbf{v}_w) \mathbf{I} \right) \right]$$

$$+\nabla p_{w,rgh} + \mathbf{g}_w \cdot \mathbf{h} \nabla \rho_w = 0 \ , \tag{4.90}$$

where $p_{w,rgh} = p_w - \rho_w \mathbf{g}_w \cdot \mathbf{h}$, p_w is the pressure of the fluid phase, $\mathbf{h}$ is a position vector of the water surface oriented opposite to the direction of the gravitational vector, $\mathbf{g}^{\overline{w}}$ is the gravitational acceleration vector, $\hat{\mu}_w$ is the dynamic viscosity of the fluid phase, and the superscript T is the transpose operator. Both ρ_w and $\hat{\mu}_w$ are functions of the solution composition for the non-dilute case considered. The system is assumed to be isothermal, and the solid phase is immobile.

The microscale species conservation of mass equation is

$$\frac{\partial}{\partial t}\left(\rho_w \omega_{Aw}\right) + \nabla \cdot \left(\rho_w \mathbf{v}_w \omega_{Aw}\right) - \nabla \cdot \left(\rho_w D_{Aw} \nabla \omega_{Aw}\right) = 0 \ , \tag{4.91}$$

where the qualifier A refers the the salt species, ω_{Aw} is the mass fraction, and D_{Aw} is the diffusion coefficient of species A in the fluid phase. The non-dilute diffusion coefficient is approximated as (Bashar and Tellam, 2011; Gordon, 1937)

$$D_{Aw} = D_0 \frac{\hat{\mu}_0}{\hat{\mu}_w} \frac{1}{\rho_w V_{Bw}} \left[1 + m_{Aw} \frac{d\left(\ln \hat{\gamma}_{Aw}\right)}{dm_{Aw}}\right] \ , \tag{4.92}$$

where D_0 is the dilute diffusion coefficient, $\hat{\mu}_0$ is the viscosity of pure water, V_{Bw} is the partial mass volume of the water (species B), m_{Aw} is the molality, and $\hat{\gamma}_{Aw}$ is the activity coefficient. The dependence of ρ_w, $\hat{\mu}_w$, and $\hat{\gamma}_{Aw}$ on composition for $CaBr_2$-water solutions were taken from the literature (Weigand et al., 2018a).

4.4.2 Non-dimensional Microscale Model

The non-dimensional form of the governing microscale equations can provide additional insight on the relative importance of each term. Defining the following non-dimensional variables

$$t^* = \frac{v_{\mathbf{in}}^w}{d_{50}} t; \quad \mathbf{x}^* = \frac{\mathbf{x}}{d_{50}}; \quad \mathbf{v}_w^* = \frac{\mathbf{v}_w}{v_{\mathbf{in}}^w}; \quad \mathbf{g}_w^* = \frac{\mathbf{g}_w}{G}; \quad \mathbf{h}^* = \frac{\mathbf{h}}{d_{50}}; \quad \nabla^* = d_{50} \nabla;$$
$$\hat{\mu}_w^* = \frac{\hat{\mu}_w}{\hat{\mu}_0}; \quad \rho_w^* = \frac{\rho_w}{\rho_0}; \quad p_{w,rgh}^* = \frac{p_{w,rgh}}{d_{50} \rho_0 G}; \quad D_{Aw}^* = \frac{D_{Aw}}{D_0} \ , \tag{4.93}$$

where the $*$ superscript refers to a non-dimensional quantity, v_{in}^{w} is the macroscale inlet velocity, d_{50} is the mean grain diameter and G is the magnitude of the gravity vector. The non-dimensional conservation of mass equation for the phase is

$$\frac{\partial \rho_w^*}{\partial t^*} + \nabla^* \cdot (\rho_w^* \mathbf{v}_w^*) = 0 \ , \tag{4.94}$$

the non-dimensional phase momentum equation is

$$\begin{aligned} \frac{\partial}{\partial t^*} (\rho_w^* \mathbf{v}_w^*) + \nabla^* \cdot (\rho_w^* \mathbf{v}_w^* \mathbf{v}_w^*) - \frac{1}{\text{Re}_0} \nabla^* \cdot \left[\hat{\mu}^* \left(\nabla^* \mathbf{v}_w^* + \nabla^* \mathbf{v}_w^{*T} - \frac{2}{3} (\nabla^* \cdot \mathbf{v}_w^*) \mathbf{I} \right) \right] \\ + \frac{1}{\text{Fr}^2} \left(\nabla^* p_{w,rgh}^* + \mathbf{g}^* \cdot \mathbf{h}^* \nabla^* \rho_w^* \right) = 0 \ , \end{aligned} \tag{4.95}$$

where

$$\text{Re}_0 = \frac{\rho_0 d_{50} v_{\text{in}}^{w}}{\hat{\mu}_0} \quad \text{and} \quad \text{Fr} = \frac{v_{\text{in}}^{w}}{\sqrt{d_{50} G}} \ . \tag{4.96}$$

The non-dimensional species mass conservation equation is

$$\frac{\partial}{\partial t^*} (\rho_w^* \omega_{Aw}) + \nabla^* \cdot (\rho_w^* \mathbf{v}_w^* \omega_{Aw}) - \frac{1}{\text{Pe}_0} \nabla^* \cdot (\rho_w^* D_{Aw}^* \nabla^* \omega_{Aw}) = 0 \ , \tag{4.97}$$

where

$$\text{Pe}_0 = \frac{d_{50} v_{\text{in}}^{w}}{D_0} \ . \tag{4.98}$$

4.4.3 Macroscale Model

In this work, we are using microscale simulations to investigate dilute and non-dilute flow and transport at both the micro- and macroscale. For dilute flow and transport at the macroscale, well-established models have been developed and consist of macroscale conservation of mass and momentum equations. We assume that the dilute microscale simulations can be modeled as macroscopically one-dimensional systems. For the definition of the macroscale variables refer to (Gray and Miller, 2009, 2014).

We summarize the Fickian solute transport model for an immobile and incompressible solid phase for macroscale flow and transport in one spatial dimension, which we denote as z. The macroscale

conservation of mass equation for the fluid phase is

$$\frac{\partial\left(\epsilon^{\overline{\overline{w}}}\rho^{w}\right)}{\partial t}=-\frac{\partial}{\partial z}\left(\epsilon^{\overline{\overline{w}}}\rho^{w}v^{\overline{w}}\right)\ ; \tag{4.99}$$

an approximate momentum conservation in the form of Darcy's law is

$$\epsilon^{\overline{\overline{w}}}v^{\overline{w}}=\frac{\hat{k}}{\hat{\mu}_{w}}\left(\frac{\partial p^{w}}{\partial z}+\rho^{w}g^{\overline{w}}\right)\ ; \tag{4.100}$$

and a species conservation of mass equation for the fluid phase is

$$\frac{\partial\left(\epsilon^{\overline{\overline{w}}}\rho^{w}\omega^{A\,\overline{w}}\right)}{\partial t}=-\frac{\partial}{\partial z}\left(\epsilon^{\overline{\overline{w}}}\rho^{w}\omega^{A\,\overline{w}}v^{\overline{w}}\right)-\frac{\partial}{\partial z}\left(\epsilon^{\overline{\overline{w}}}\rho^{w}\omega^{A\,\overline{w}}u^{\overline{\overline{A\omega}}}\right)\ , \tag{4.101}$$

where z is positive upwards, $\epsilon^{\overline{\overline{w}}}$ is the porosity, $v^{\overline{w}}$ is the density averaged macroscale fluid velocity in the z direction, $\hat{k}$ is the intrinsic permeability, p^{w} is the macroscale pressure of the water phase, ρ^{w} is the macroscale density, which for our work is constant as we are only applying these equations to the dilute simulations, $g^{\overline{w}}$ is the magnitude of the gravitational acceleration, $\omega^{A\,\overline{w}}$ is the macroscale mass fraction of species A (salt in this work) in the water phase, and $u^{\overline{\overline{Aw}}}$ is the macroscale deviation velocity for species A in the water phase.

The deviation velocity for dilute transport is generally parametrized by using a Fickian approximation for the mass flux which can be written as (Bear, 1979)

$$J^{\overline{\overline{Aw}}}=\epsilon^{\overline{\overline{w}}}\rho^{w}\omega^{A\,\overline{w}}u^{\overline{\overline{A\omega}}}=-\epsilon^{\overline{\overline{w}}}\rho^{w}\hat{D}\frac{\partial\omega^{A\,\overline{w}}}{\partial z}\ , \tag{4.102}$$

where $J^{\overline{\overline{Aw}}}$ is defined as the mass flux of species A and $\hat{D}$ is the hydrodynamic dispersion for porous media systems. The most commonly used form, in one-dimension, is

$$\hat{D}=\frac{\hat{D}_{Aw}}{\hat{\tau}}+\hat{\alpha}_{L}v^{\overline{w}}\ , \tag{4.103}$$

where $\hat{\tau}$ is the tortuosity of the porous medium, which is defined as the average microscale distance traveled by a species per unit macroscale length of the medium and is greater than or equal to one; and

$\hat{\alpha}_L$ is the longitudinal dispersivity (Bear, 1979). It should be noted that this macroscale model is only valid for and applied to the dilute simulations.

4.4.4 Model Approximations

To solve the microscale model for non-dilute flow and transport, a solver was created within the OpenFOAM framework (v1712) (Weller et al., 1998). OpenFOAM is an open-source, finite volume method, computational fluid dynamics software package that allows for easy parallelization and is packaged with mesh generation software (www.openfoam.com). The existing compressible Navier-Stokes solvers were not suitable for solving our model as they either couple the density and viscosity through an energy equation as opposed to a species transport equation, lack the necessary gravitational terms, and/or assume constant viscosity.

The governing equations were solved using an implementation of the PIMPLE algorithm (Greenshields, 2019). This algorithm is a combination of the Semi-Implicit Method for Pressure-Linked Equations (SIMPLE) algorithm (Ferziger and Perić, 2002) used for steady-state simulations and the Pressure Implicit with Splitting of Operators (PISO) algorithm (Issa, 1986; Kaslusky and Udell, 2002). The PIMPLE implementation allows for larger time steps, than generally allowed by the CFL condition, by iteratively solving the equations and applying under-relaxation. The OpenFOAM solver `rhoPimpleFoam` was used as a template for our model, where we replaced the energy equation with the species transport equation, included the gravitational terms and allowed the density and viscosity to be functions of the salt species mass fraction. To isolate the impacts that the density, viscosity, and activity have on non-dilute transport, solvers were also created for models where each of the three functions were forced to equal their dilute value.

To solve the macroscale dilute flow and transport equations, a cell-centered finite difference code was used (Weigand et al., 2018a). To determine the permeability and longitudinal dispersivity, the method of moving asymptotes algorithm in the software package NLopt (version 2.4.2) (Johnson, 2014) was used to minimize the ℓ_2 error norm between the solution to the macroscale equations results and the averaged microscale simulation results.

4.4.5 Microscale Domain Generation

For the microscale simulations, 12/20 Accusand was used for the media to be consistent with the experimental work of Weigand et al. (2018a). The sphere packing code of Baranau and Tallarek (2014) was used to generate the media. With this code, the mean grain diameter ($d_{50} = 0.11$ cm), the standard deviation ($\sigma_{d_{50}} = 0.2$ cm) of the grain diameter, and the porosity ($\epsilon^{\overline{\overline{w}}} = 0.35$) were matched to the literature values by sampling from a lognormal distribution (Hauswirth, 2019). The parameters used for the 12/20 Accusand are in agreement with other studies (Schroth et al., 1996).

We examined both a representative elementary volume (REV) scale and a sub-REV-scale. The sub-REV-scale was examined to allow for storage and visualization of the microscale results. Only macroscale variables could be saved for the REV-scale simulations due to memory limitations. For the sub-REV simulations, 180 spheres were packed in a cube, with each side equal to 0.514 cm. For the REV simulations, more than 7,400 spheres were packed in a rectangular column, where the height to cross-sectional area had a ratio of 6:1 and the dimensions were 6.54 cm $\times$ 1.09 cm $\times$ 1.09 cm. This aspect ratio was used to allow for more averaging regions along the direction of flow while still having a large enough cross section to ensure a REV.

The distributions and packed media are shown in Figures 4.19 and 4.20 for the REV-scale and sub-REV-scale, respectively. The porosity for both of the domains was 0.35. The tortuosity was calculated for the sub-REV domain using (Duda et al., 2011; Koponen et al., 1996)

$$\tau = \frac{\int |\mathbf{v}_w| \, \mathrm{d}x}{\int v_z \, \mathrm{d}x} \, , \tag{4.104}$$

where v_z is the velocity in the main direction of flow.

4.4.6 Model Implementation

The sphere-packing code provided sphere centroids and radii that were discretized in OpenFOAM using `snappyHexMesh`. The work of Icardi et al. (2014) found a near grain refinement level of 2 in `snappyHexMesh` was sufficient to produce a solution that was grid independent, however only the flow field was examined and not species transport. To confirm their conclusions and ensure the salt species was also independent of the grid for our simulations, a grid independence study was performed

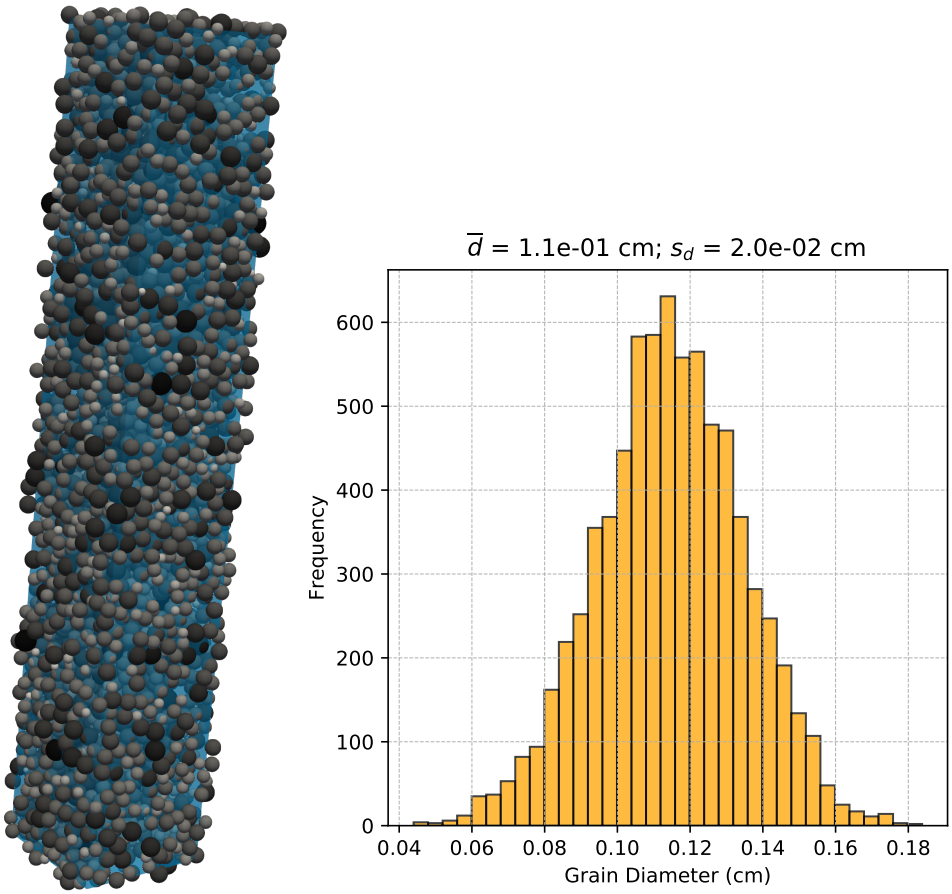

(a) (b)

Figure 4.19: Sphere packing results (a) and grain diameter distribution (b) for the REV-scale domain. The direction of flow for all simulations was upwards and the blue box represents the domain that was simulated.

on the sub-REV domains. We found a strong dependency on the grid that must be supplied before the mesh is refined around the solid grains but a near grain refinement level of 2 was sufficient.

For the microscale simulations, wall boundary conditions were assumed for the sides of the packed column, where the sides are specified as the direction orthogonal to gravity. At the top of the column, outflow boundary conditions were specified, which fixed the pressure to atmospheric pressure and forced a zero gradient for the velocity and salt mass fraction. For the inlet boundary condition, a fixed mass flow rate was enforced for all simulations, and the incoming salt mass fraction was constant. By using a fixed mass flow rate, the volumetric flow rate, and in turn the macroscale velocity, varied because the density of the incoming fluid depended upon salt mass fraction.

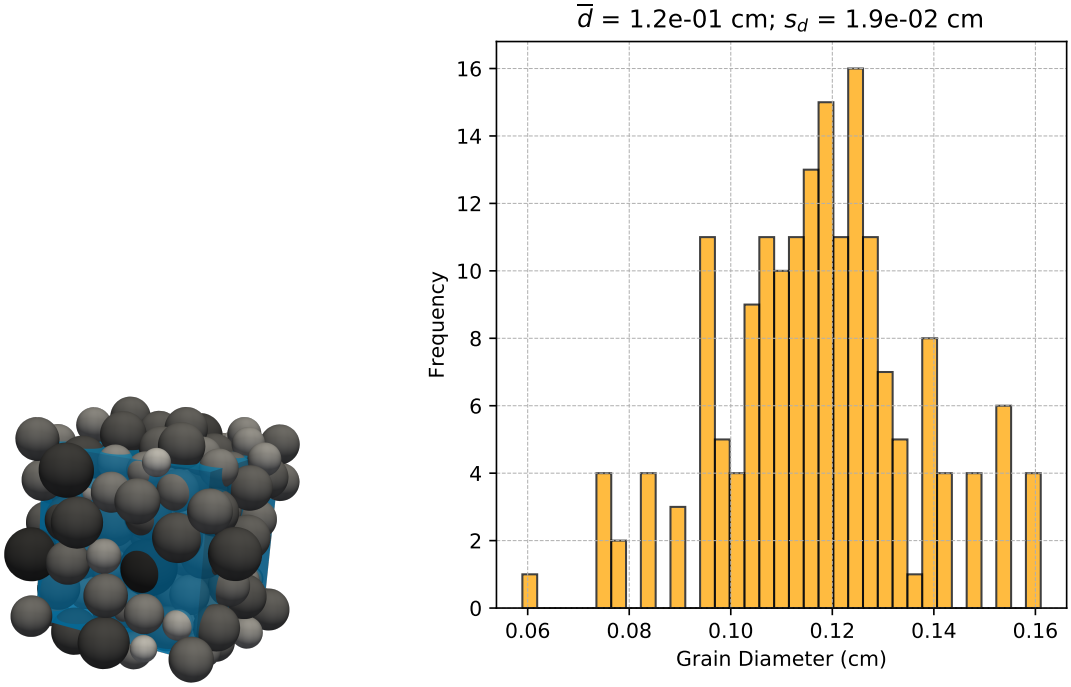

Figure 4.20: Sphere packing results (a) and grain diameter distribution (b) for the sub-REV-scale domain. The blue box represents the domain that was simulated.

The simulations performed consisted of varying the incoming salt mass fraction (ω_{in}), the salt mass fraction initially present in the column (ω_{res}), and the incoming mass flow rate. For the initial conditions, the steady-state incompressible Navier-Stokes equations were solved based on the resident fluid properties and the resulting pressure and velocity fields were used as the initial conditions for the transient simulations. This was done so that the system began with a fully developed flow field.

Macroscale averages were calculated on the fly for the REV-scale simulations as the microscale data could not be stored due to memory limitations. The macroscale averages were calculated according to (Gray and Miller, 2009, 2014). The domain was split into seven different overlapping REVs and macroscale average values were calculated in each volume. Each REV contained the entire cross-section of the domain and had a height in the direction of flow of 3.27 cm. The REVs overlapped by 0.545 cm. Additionally, averaged microscale values were calculated at seven different cross sections along the height of the column separated by a distance of 1.09 cm. For the sub-REV simulations, all data could be stored however microscale averages were also calculated for five different volumes and at eight different cross sections.

For the salt species, calcium bromide ($CaBr_2$) was selected due to the complex nature of its activity coefficient and its use in previous studies. The density, viscosity, and activity coefficients from Weigand et al. (2018a) were used. The dilute diffusion coefficient (D_0) was set to 1.05×10^{-5} cm/s^2.

The REV scale simulations were run with OpenFoam v1712 on UNC Research Computings Dogwood cluster with 2,107 processors. OpenFOAM's implementation of Scotch was used for domain decomposition (Pellegrini, 2008). For the sub-REV scale simulations, the number of processors changed to four.

4.5 Results and Discussion

4.5.1 Dilute Simulations

4.5.1.1 Dilute REV-Scale Simulations

Dilute experiments at three different mass flow rates ($\dot{m}^w_{\text{in}}$) were first performed so that a baseline could be established to allow for comparisons between dilute and non-dilute flow and transport. The dilute experiments also allowed us to characterize the porous media to ensure that the model produces expected values for the media being simulated.

The microscale simulation results were averaged and the resulting macroscale breakthrough curve was used to determine the longitudinal dispersivity ($\hat{\alpha}_L$). This was accomplished by performing a parameter estimation where the dilute macroscale flow and transport equation was fit to the averaged microscale results at a cross-section by optimizing the longitudinal dispersivity, as shown in Figure 4.21. The first two averaging regions were excluded from the fits to avoid any entrance effects. To determine the intrinsic permeability of the porous media ($\hat{k}$), Eqn (4.100) was used with the averaged microscale results for fluid pressure at the inlet and outlet of the domain. The sub-REV-scale domain dilute simulation results were used with Eqn (4.104) to estimate a value of the tortuosity of 1.22, which agrees with the literature (Aramideh et al., 2018; Icardi et al., 2014). This value was used for the dilute macroscale transport equation.

The conditions and resulting estimated parameters for three dilute simulations performed at an REV-scale are reported in Table 4.6. The $\hat{\alpha}_T$ reported by Weigand et al. (2018a) for a similar medium ranged from 0.098–0.16 cm and were based on laboratory experiments. The increase of the dispersivity for the highest Pe_0 agrees with the literature (Icardi et al., 2014); the Re_0 also increases and offers

Table 4.6: Experimental values and optimized macroscale parameters for the REV-scale dilute simulations.

$\dot{m}^w_{\text{in}}$ (g/s)	Re_0	Pe_0	$\hat{\alpha}_L$ (cm)	$\hat{k}$ (cm^2)
10^{-6}	3.1×10^{-5}	0.026	0.049	7.4×10^{-6}
10^{-4}	3.1×10^{-3}	2.6	0.035	7.4×10^{-6}
10^{-2}	3.1×10^{-1}	260	0.15	7.4×10^{-6}

a mechanistic rationale for this observation. Schroth et al. (1996) report an intrinsic permeability of 4.6×10^{-6} cm^2 for 12/20 Accusand, which is slightly lower than our estimated value, however they also report different mean grain diameters and porosities than used in this work, and spheres are an idealized representation of Accusand.

4.5.1.2 Dilute Sub-REV-Scale Simulations

To assess how the microscale velocity distribution impacts macroscale dispersion, sub-REV-scale dilute simulations were performed for set of Re_0 that matched the REV-scale simulations. Complete microscale simulation details were stored and analyzed for the sub-REV-scale simulations. The sub-REV-scale velocities were sampled along cross-sections orthogonal to the direction of flow near the outflow boundary.

Figure 4.22 shows the distribution of the microscale velocity components for the lowest and highest Re_0 for the sub-REV domain. For all three simulations, the means of the velocities in direction orthogonal to the flow (v_x and v_y) are approximately zero. For the velocity in the direction of flow, the mean is equal to the superficial face velocity. This agrees with Aramideh et al. (2018), however Icardi et al. (2014) stated that the bin with the highest frequency corresponded to their superficial velocity. This suggests an error in their results as the density weighted mean of the velocity in the direction of flow must equal the superficial velocity. Additionally, the mean and standard deviation for the velocity in the z-direction are equal. Aramideh et al. (2018) showed that the microscale velocity distribution at low porosities are nearly exponentially distributed. To test this, the velocity in the z-direction was fit to an exponential distribution but failed both the Kolmogorov-Smirnov and Andersen-Darling goodness-of-fit tests (Evans et al., 2008).

The microscale velocities in the mean direction of flow are all positive for every flow rate considered. Icardi et al. (2014) observed negative velocities at similar Re_0 but there porous media con-

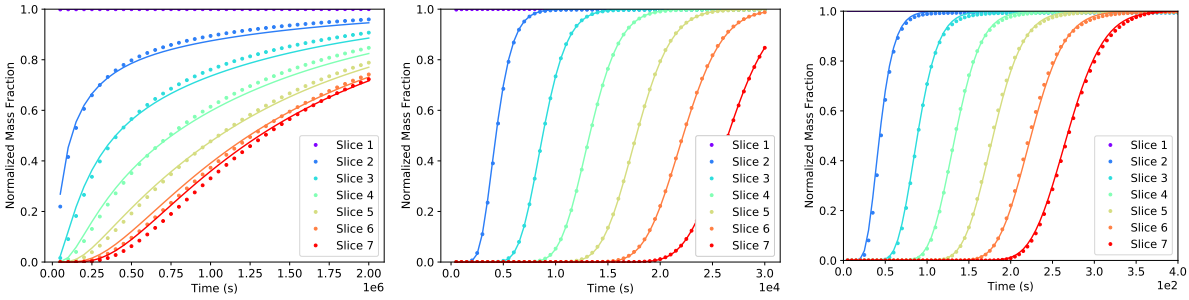

(a) (b) (c)

Figure 4.21: Results of fitting the dilute macroscale model (lines) to REV-scale cross-section averaged microscale data (points) for Pe = 0.026 (a), 2.6 (b), and 260 (c).

sisted of irregular and polydisperse objects that contained local blockages that resulted in the negative velocities in the mean direction of flow. The work of Aramideh et al. (2018) examined mono- and polydisperse spheres and while they observed negative velocities at similar Re_0, they considered it to be negligible. For non-dilute flow and transport, negative velocities in the mean direction of flow can develop due to gravity stabilization, however for dilute flow and transport they represent recirculation zones. Since we did not observe any negative velocities in our dilute simulations, if we observe negative velocities in the mean direction of flow in our non-dilute simulations they can be attributed to gravity stabilization effects. The velocity distributions and ranges for the three experiments are nearly identical but scaled. This shows that, with the Re_0 considered, no new flow pathways are forming (Andrade et al., 1997).

4.5.2 Non-Dilute

4.5.2.1 Non-Dilute REV-Scale Simulations

The laboratory work by Weigand et al. (2018a) consisted of a single incoming flow rate that had a Re_0 of 0.07. While we did not directly match that Reynolds number, Figure 4.23 shows the macroscale mass fraction breakthrough curves for our most similar set of experiments ($\mathrm{Re}_0 \approx 10^{-1}$). The length of the column in the laboratory experiments was more than ten times longer than the REV-size domains for the microscale experiments. We observe that the averaged microscale results follow the same trend as the experimental data. The dilute model produces the most disperse solution and the breakthrough curve sharpens as the incoming mass fraction increases, while the resident initial condition fluid mass fraction remains zero. For the experiment with a non-zero resident initial condition

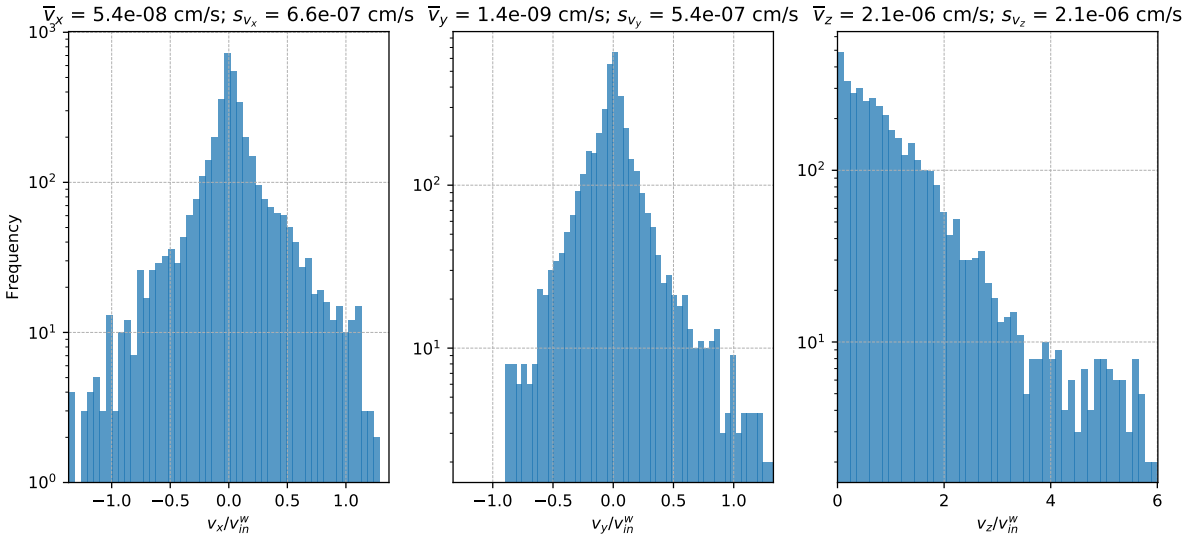

(a)

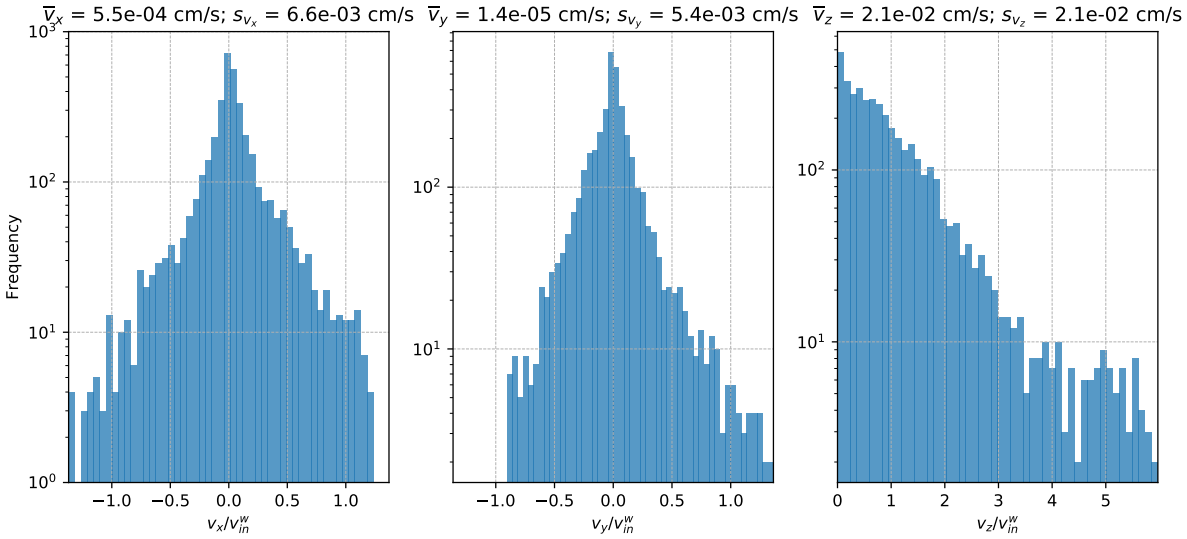

(b)

Figure 4.22: Dilute microscale sub-REV velocity distributions for $\mathrm{Re}_0 = 3.1\times10^{-5}$ (a) and $\mathrm{Re}_0 = 0.31$ (b). The means and standard deviations of the velocity are included. The distributions were sampled at a cross-section orthogonal to the mean direction of flow.

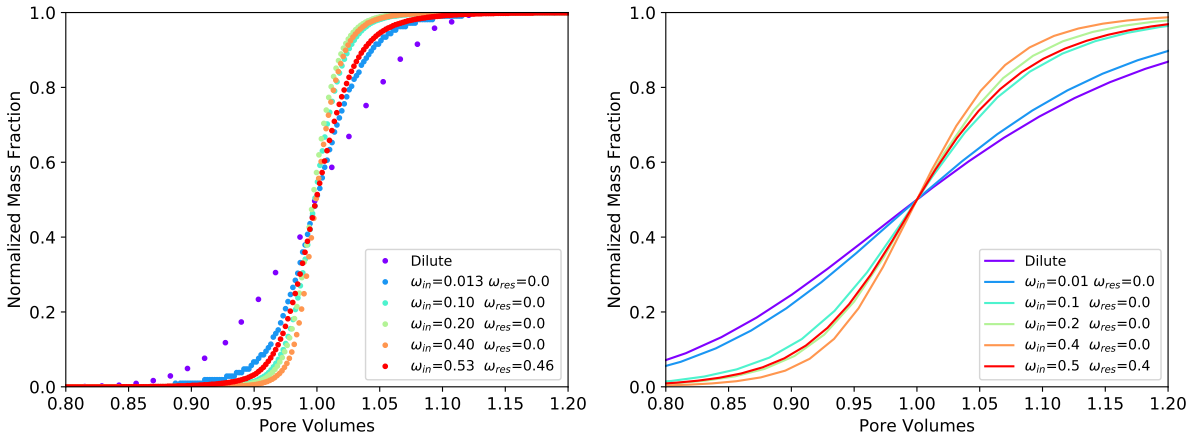

(a) (b)

Figure 4.23: Laboratory experiments (a) from (Weigand et al., 2018a) and averaged REV-scale microscale simulations (b). Both the laboratory experiments and simulations use $CaBr_2$ as the salt species but the results shown are at different Re and the column lengths differ.

salt mass fraction, the averaged microscale simulation results also show breakthrough curve profiles similar to those previously reported based upon laboratory studies despite the different mass fractions used.

The REV-scale non-dilute simulations were performed at the same three mass flow rates that were used with the dilute microscale simulations and five different combinations of initial mass fractions and displacing mass fractions for the salt species were examined for each flow rate. For the non-dilute simulations, the Re and Pe vary throughout the domain as the densities, viscosities and diffusion coefficient are functions of the mass fraction. We define these numbers, and an additional non-dimensional gravity number, N_g, to aid interpretation of the simulated results as

$$\mathrm{Re} = \frac{\rho_{\mathrm{in}} d_{50} v_{\mathrm{in}}^w}{\hat{\mu}_{\mathrm{in}}} \qquad \mathrm{Pe} = \frac{d_{50} v_{\mathrm{in}}^w}{D_{Aw,\mathrm{in}}} \qquad N_g = \frac{\left(\rho_{\mathrm{in}} - \rho_{\mathrm{res}}\right) \hat{k} G}{\hat{\mu}_{\mathrm{in}} v_{\mathrm{in}}^w} \,. \tag{4.105}$$

N_g is a measure of the ratio of gravitational forces to advective forces. For large N_g, gravity stabilization becomes dominant compared to advective transport. Table 4.7 shows the Re, Pe and N_g for the two highest mass flow rate experiments. The decrease in the Re and Pe as the incoming mass fractions increase is due to a decrease in the inlet velocity.

The breakthrough curves for Re $\approx 10^{-3}$ experiments are shown in Figure 4.24. The breakthrough curves for Re $\approx 10^{-5}$ (not shown) only differ in that the solutions are more diffuse and the displace-

Table 4.7: Non-dilute REV-scale simulation parameters for the two highest mass flow rates considered. The two highest flow rate experiments have Re $\approx 10^{-3}$ and Re $\approx 10^{-1}$, respectively.

ω_{in}	$\dot{m}^w_{\text{in}} = 10^{-4}$ g/s			$\dot{m}^w_{\text{in}} = 10^{-2}$ g/s		
	Re (10^{-3})	Pe	N_g	Re	Pe	N_g
Dilute	3.1	2.6	0	0.31	260	0
0.01	3.0	3.1	81	0.30	310	0.81
0.1	2.7	2.3	840	0.27	239	8.4
0.2	2.4	1.6	1800	0.24	160	18
0.4	1.3	0.99	2900	0.17	99	29
0.5	0.73	0.99	2500	0.073	99	25

ment experiment where $\omega_{\text{in}} = 0.1$ is more diffuse than the dilute displacement at the lowest flow rate. These experiments depict behavior that is in contrast to the current understanding of macroscopic non-dilute transport. The front is thought to sharpen as the incoming mass fraction increases but we observe the opposite behavior at these Pe (Broeke and Krishna, 1995; Jiao and Hötzl, 2004; Konz et al., 2009; Landman et al., 2007a,b; Noordman and Wesselingh, 2002; Starr and Parlange, 1976; Watson et al., 2002c). The molecular diffusion coefficient as a function of mass fraction is shown in Figure 4.25. The sharpness of the non-dilute fronts is correlated to the diffusion coefficient with one exception. For the case where $\omega_{\text{in}} = 0.1$, the diffusion coefficient is slightly larger (2%) than the dilute diffusion coefficient and the Pe is slightly lower than the dilute displacement, however, the non-dilute displacement breakthrough is sharper than the dilute breakthrough curve. This demonstrates that we are observing non-dilute behavior for these displacement experiments as a higher diffusion coefficient and lower Pe should produce a more diffuse breakthrough curve for a dilute displacement experiment.

The macroscale breakthrough curves for Re $\approx 10^{-1}$ are shown in Figure 4.23b. This set of experiments is in good agreement with existing experimental work and the current understanding of non-dilute behavior (Hassanizadeh and Leijnse, 1988; Landman et al., 2007b; Watson et al., 2002c; Weigand et al., 2018a). The curves sharpen as the incoming mass fraction increases and when the resident fluid has a non-zero salt concentration, the difference between the fluid properties controls behavior. At this high of a Pe number, the non-dilute behavior is a result of the non-dilute effects on the flow field. While molecular diffusion will still impact the solution, it becomes a higher order effect as can be seen with the $\omega_{\text{in}} = 0.4$ experiment having the highest molecular diffusion coefficient but also having the sharpest breakthrough curve at this flow rate.

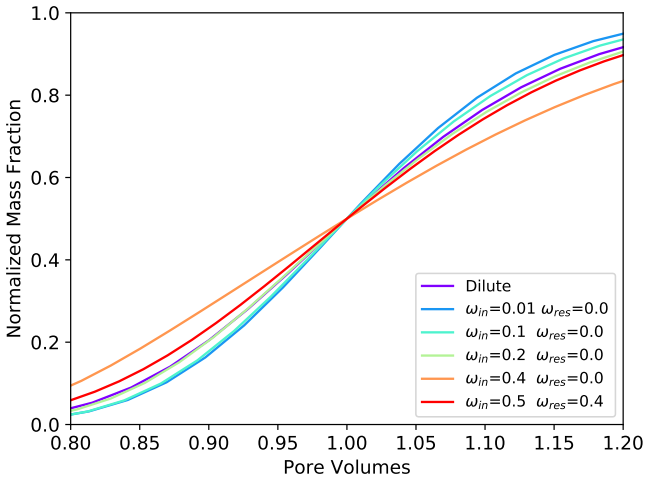

Figure 4.24: Averaged REV-scale non-dilute breakthrough curves for Re $\approx 10^{-3}$.

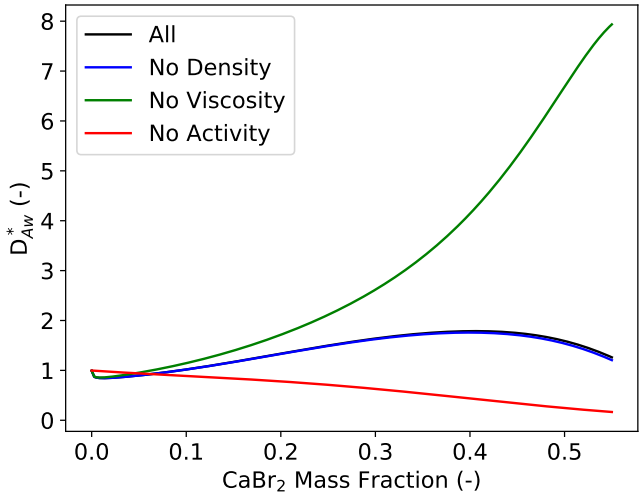

Figure 4.25: Molecular diffusion sensitivity to density, viscosity, and activity (see Eqn (4.92)).

4.5.2.2 Non-Dilute Sub-REV Simulations

As was done with the dilute experiments, sub-REV simulations were performed to examine microscale behavior. Figure 4.26 shows the normalized microscale mass fractions at a cross-section along the mean flow direction for the dilute tracer and for the $\omega_{\text{in}} = 0.4$ displacement experiment at Re $\approx 10^{-3}$, where flow is moving upwards. The higher incoming salt mass fraction displacements experiments were more disperse than the dilute simulation at this Re.

By examining the microscale mass fractions, we can see the effects of gravity stabilization. For the dilute case, the salt concentration varies significantly as we move across the domain orthogonal to the direction of flow. This is due to mechanical dispersion. For the non-dilute simulation, there is less variation in the mass fraction as we move along a cross section. When a denser fluid is above a less dense fluid, which can be caused by the tortuous path of a porous media, gravity will force the denser fluid downwards. By examining the non-dimensional form of the compressible Navier-Stokes equation (Equation 4.95), we can see the relative importance of each term. For the non-dilute displacement with $\omega_{\text{in}} = 0.4$, Re^{-1} is 7.6×10^2 and Fr^{-2} is 4.2×10^8, therefore the dominant term in Eqn (4.95) is the term with the Fr. Ignoring all other terms, the gradient of the pressure-like term ($p^*_{w,rgh}$) and the density must equal, as gravity is assumed constant in this work, but have opposite signs. When a more dense fluid is above a less dense fluid, the gradients of the pressure and density have the same sign. This can produce either negative velocities in the direction of gravity or slow down the velocities in the mean direction of flow. This stabilization restricts the movement of the salt species and produces a more uniform microscale mass fraction field along a given cross-section orthogonal to gravity.

To further ensure that we were observing gravity stabilization, the microscale velocities and mass fractions were sampled at a cross-section orthogonal to the gravitational vector (Figure 4.27). For our dilute microscale simulations, no negative velocities in the direction of gravity were observed at the Reynolds numbers considered. For our non-dilute simulations, we observe negative velocities that are a result of gravity stabilization. The velocity distribution in the mean direction of flow becomes increasingly more skewed to the left as the incoming salt mass fraction increases, resulting in larger negative velocities. The variance of the velocity components orthogonal to gravity increases as the salt front passes through as compared to the dilute simulations. Gravity stabilization not only impacts

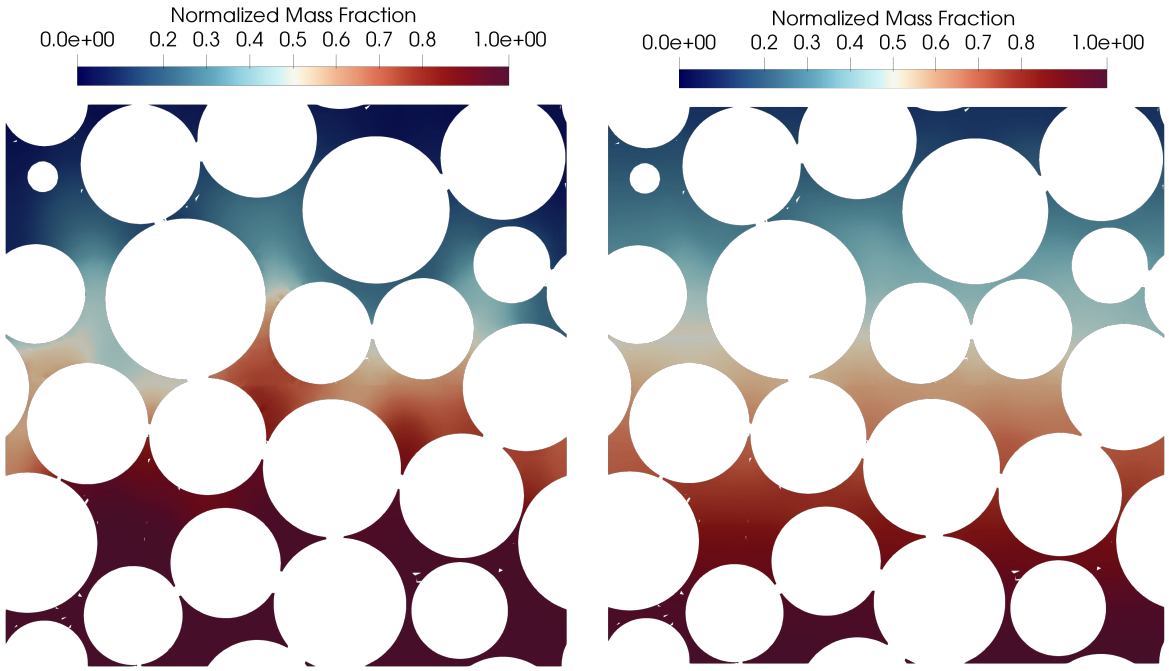

(a) (b)

Figure 4.26: Normalized microscale mass fraction for the dilute (a) and $\omega_{\text{in}} = 0.4$ and $\omega_{\text{res}} = 0$ (b) experiments at Re $\approx 10^{-3}$. The direction of flow is upwards.

the velocities in the direction of gravity but also the velocities orthogonal to gravity as gravity acts to stabilize the front.

The same sub-REV analysis was performed for the experiments with Re $\approx 10^{-1}$ and the normalized microscale mass fractions for the dilute and $\omega_{\text{in}} = 0.4$ displacement experiment are shown in Figure 4.28. As with the lower Re experiments, the non-dilute displacement is smoother than the dilute tracer when moving along a cross-section orthogonal to the mean direction of flow. Additionally, the length of the mixing zone from the bottom to the top of the figure is much thinner for the non-dilute experiment compared to the dilute tracer, which produces a sharper macroscale breakthrough curve for the non-dilute system. At this larger Re however, we observe locations where a higher density fluid is above a lower density fluid which was not observed at the lower Re experiments. Comparing the gravity numbers for the $\omega_{\text{in}} = 0.4$ displacement experiments at the two different Re shows that at the larger Re simulation, gravity does not have as much time to stabilize the front and we observe locations were instabilities remain. For this simulation, $\text{Re}^{-1} = 7.6$ and $\text{Fr}^{-2} = 4.2 \times 10^5$, which means the Fr term is still dominating behavior. Since we are observing denser fluid above less dense fluid, gravity stabilization is causing reduced velocities in the direction of flow as opposed to negative velocities. At

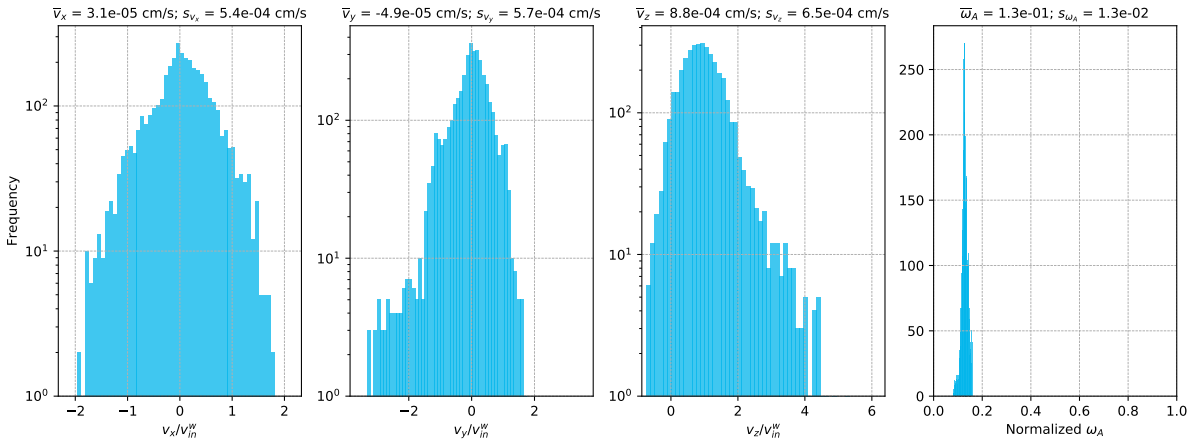

(a)

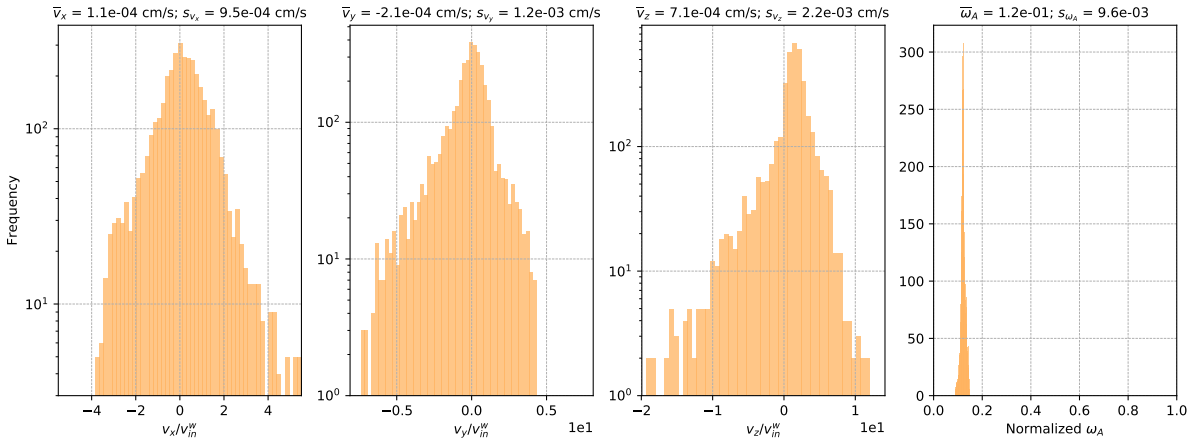

(b)

Figure 4.27: Velocity and mass fraction distributions for $\omega_{\text{in}} = 0.1$ (a) and $\omega_{\text{in}} = 0.4$ (b) at Re $\approx 10^{-3}$. The fields were sampled at a cross-section orthogonal to the mean direction of flow.

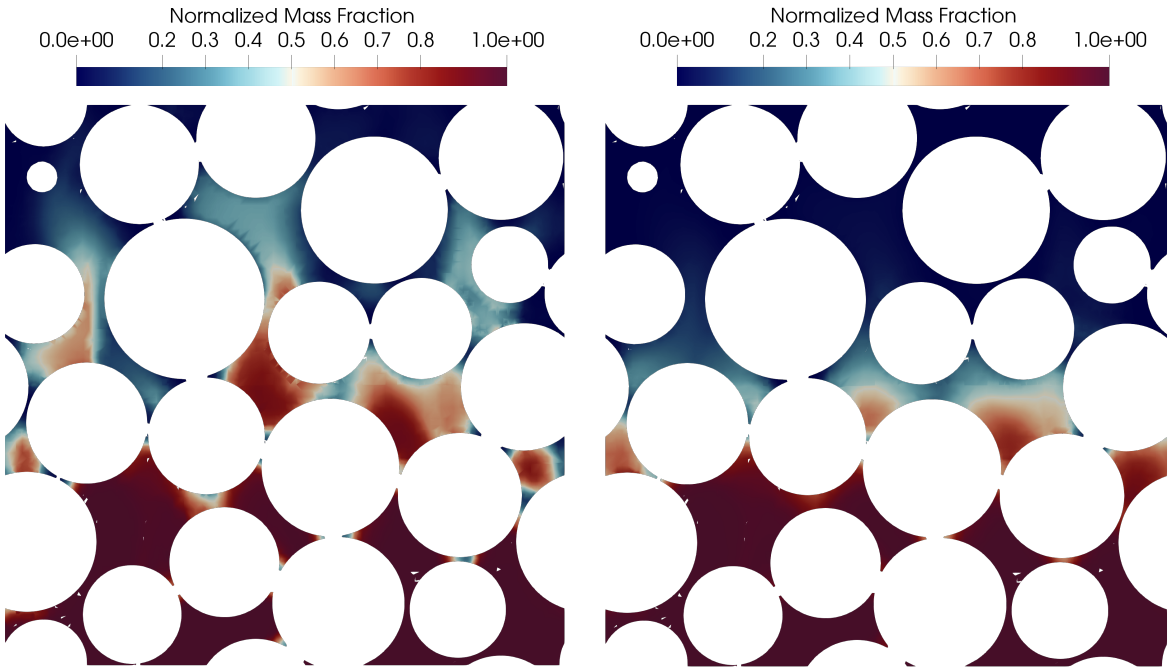

(a) (b)

Figure 4.28: Normalized microscale mass fraction for the dilute (a) and $\omega_{\text{in}} = 0.4$ (b) experiments at Re $\approx 10^{-1}$. For the non-dilute displacement, higher density fluids can be seen above lower density fluids where grains of sand touch.

this Re and Pe number, the gradient of the pressure term must always have a larger magnitude than the magnitude of the density gradient.

To confirm these observations, the microscale velocity distributions for the non-dilute experiment at the largest Re are shown in Figure 4.29. No negative velocities are observed in the direction of gravity for the non-dilute displacements at this Re. However, the variance in the velocity decreases and we no longer observe the large positive velocities. For the non-dilute displacement with $\omega_{\text{in}} = 0.4$, the initial standard deviation in the z-direction is 0.063 cm/s and is reduced to a minimum value of 0.043 cm/s and occurs when the front is approximately halfway through the domain. For the lower Re experiments, the standard deviation of the z-component velocity increased as the front moved through. For the lower Re experiments, where the gravity numbers are two orders of magnitude larger, there is enough time for the fluid to re-arrange to a gravitational-stable distribution before the front fully moves through, which is not the case at higher Re.

The distribution of the mass fraction at the higher Re simulations is also skewed, which from a macroscale perspective produces a breakthrough curve that is asymmetric. This macroscale behavior

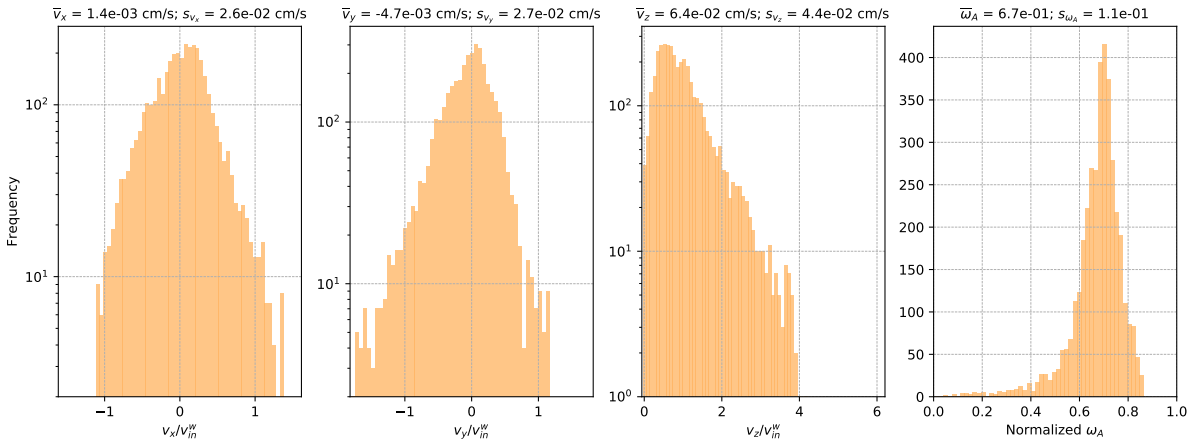

Figure 4.29: Velocity and mass fraction distributions for $\omega_{\text{in}} = 0.4$ ate Re $\approx 10^{-1}$. The velocity field was sampled at a cross-section orthogonal to the mean direction of flow.

has been observed by Weigand et al. (2018a) and was attributed to activity effects but this does not seem to be true as the lower Re simulations would also have a skewed or asymmetric distribution at the microscale. We attribute the asymmetry to the nonlinear density function. As the mass fraction increases so does the density gradient. Therefore, gravitational stabilization affects higher mass fractions more than lower mass fractions, which can be seen from the gravity number. This explains the skewness in the mass fraction histogram as well as the observed increase in size of negative velocities as the mass fraction increases at lower Re.

4.5.3 Isolation of Phenomena

One of the benefits of computational experiments over laboratory experiments is the ability to isolate different phenomena. Figure 4.30 shows the REV-scale macroscale breakthrough curves for Re $\approx 10^{-3}$ where we independently set the activity, density, and viscosity such that they are no longer functions of the salt species and are equal to their dilute values. Figure 4.31 depicts the same experiment set but at the sub-REV scale and at Re $\approx 10^{-1}$. For the simulations where the resident fluid had a non-zero salt mass fraction, we fixed the density and viscosity to the values that correspond to the resident salt mass fraction.

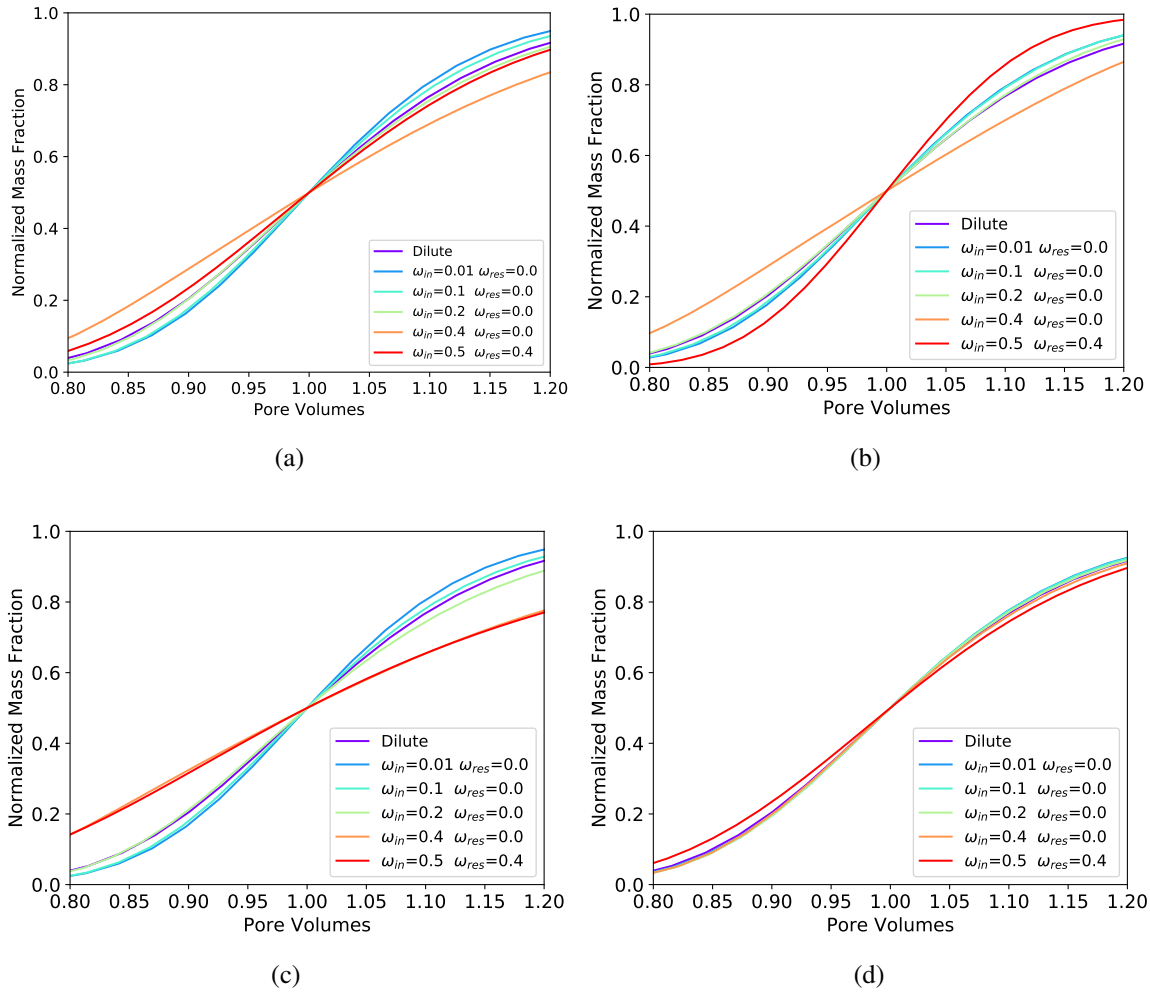

Figure 4.30: REV-scale macroscale breakthrough curves for Re $\approx$ 10^{-3} (a) and the breakthrough curves where the activity (b), viscosity (c), and density (d) are switched to their dilute values.

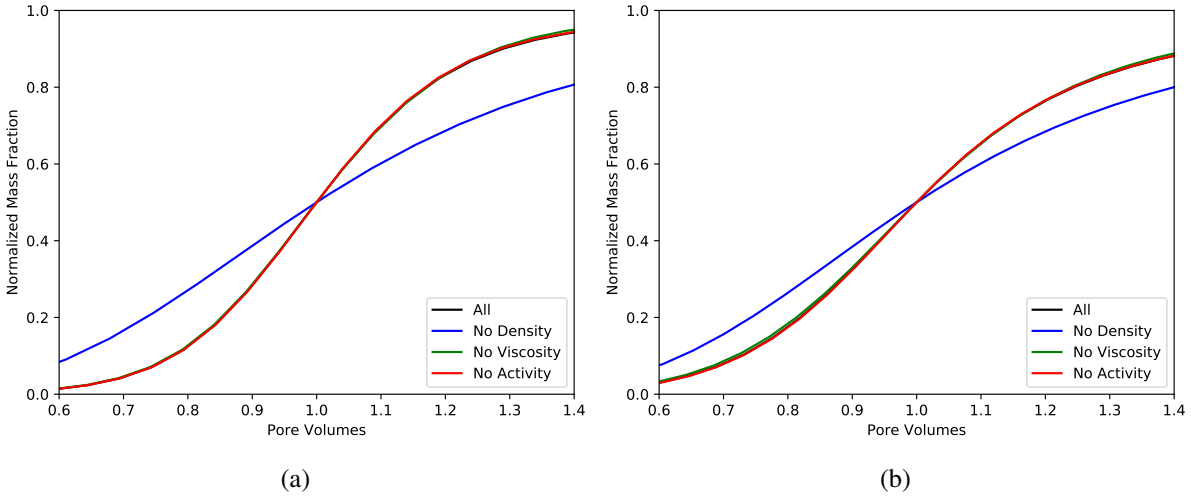

Figure 4.31: Sub-REV-scale breakthrough curve sensitivity for $\omega_{\text{in}} = 0.4$ (a) and $\omega_{\text{in}} = 0.5$ (b) with $\omega_{\text{res}} = 0.4$ with Re $\approx 10^{-1}$.

4.5.3.1 Activity

Activity only appears in the molecular diffusion coefficient and when we neglect activity effects, the molecular diffusion coefficient monotonically decreases as the mass fraction increases (Figure 4.25). For the non-dilute experiments with Re $\approx 10^{-3}$, the macroscale breakthrough curves were correlated to the diffusion coefficient with the exception of the experiment with $\omega_{\text{in}} = 0.1$, which was sharper than could be described by just examining the diffusion coefficient and Pe. Additionally, by examining the microscale flow field, we observed gravitational stabilization effects that produced negative velocities for the non-dilute simulations at this flow rate.

When the activity is turned off for the experiments with Re $\approx 10^{-3}$, we observe a different trend in the data. The displacement experiment with $\omega_{\text{in}} = 0.4$ is still the most diffuse. This indicates that the activity is not the cause for the diffuse profile, because the diffusion coefficient is the lowest as this mass fraction as compared to the other experiments that have $\omega_{\text{res}} = 0$. All other breakthrough curves are sharper than the dilute curve when we ignore activity, with the experiment with $\omega_{\text{in}} = 0.5$ and $\omega_{\text{res}} = 0.4$ switching from the second most diffuse to the sharpest breakthrough curve. This is caused by the reduced diffusion coefficient and gravity stabilization effects. At this mass flow rate and corresponding Re and Pe, activity effects must be considered.

For the higher Re experiments (Figure 4.31), turning the activity off does not cause any change in macroscale behavior. The breakthrough curves lie on top of the curves where activity was included in the experiments. This shows that at higher Re and Pe numbers the activity is a higher order phenomena for macroscale non-dilute transport.

4.5.3.2 Viscosity

Not only does the viscosity appear in the microscale conservation of momentum equation, but it also appears in the molecular diffusion coefficient. With the viscosity turned off, the molecular diffusion coefficients increases as the mass fraction increases (Figure 4.25). If we examine the non-dimensional form of the Navier-Stokes equation, we see that the viscosity appears in a term that is multiplied by the Re^{-1}. From our previous analysis, we expect viscosity to be a higher order effect as the term associated with Fr^{-2} is dominant. The viscosity is also in the denominator in the gravity

number. A decrease in the viscosity, increases the gravity number and allows more time for gravity to stabilize the front.

For the lower Re simulations, the $\omega_{\text{in}} = 0.4$ breakthrough curve and the $\omega_{\text{in}} = 0.5$ with $\omega_{\text{res}} = 0.4$ breakthrough curve are nearly identical with the viscosity fixed to a constant value (Figure 4.30c), but with the variable viscosity simulations, the experiment with $\omega_{\text{in}} = 0.5$ and $\omega_{\text{res}} = 0.4$ had a sharper breakthrough curve (Figure 4.30a). The viscosity function for $CaBr_2$ is an exponential function so it is expected to see the most dramatic impacts at the higher mass fractions. Moreover, the diffusion coefficient for the higher mass fractions with a fixed viscosity is approximately twice as large than with a variable viscosity, resulting in more diffuse breakthrough curves at higher mass fractions. With the other displacement experiments, the differences are minor and the same trends are observed for a constant viscosity as when the viscosity is variable. From this, viscosity impacts on macroscale dispersion seem to be a higher order effect except at very high salt concentrations.

For the highest Re experiments, the viscosity impacts on the macroscale breakthrough curve are negligible. The microscale velocity distribution with fixed viscosity is nearly identical to the microscale velocity distribution with a variable viscosity, which is consistent with the observation of limited viscosity effects for this case. Pe for these simulations are large enough that diffusion is small compared to mechanical dispersion. The flow profile is relatively insensitive to the viscosity due to the choice of a fixed incoming mass flow rate boundary condition. The pressure increases when the viscosity is variable and minor changes in the velocities are observed in the pore throats but they do not change enough to impact macroscale transport. Alternative boundary conditions are required to determine the effects that viscosity has on macroscale non-dilute transport.

The work of Landman et al. (2007a) agree with this and concluded that viscosity impacts are only important at lower gravity numbers and larger flow rates. In their work, they found viscosity to be important at a gravity number of 0.2 but unimportant at a number of 1.64. In this work, the lowest gravity number for a non-dilute displacement is 0.81.

4.5.3.3 Density

As with the viscosity, the density appears in the conservation of momentum equation and diffusion coefficient. When the density is fixed, the governing microscale equations reduce to the incompressible form of the Navier-Stokes equations and gravity stabilization cannot occur. This can also be seen

from the gravity number. Additionally, as the choice of boundary conditions masques viscosity effects, only the diffusion coefficient will differentiate the dilute and non-dilute displacement experiments when the density is fixed.

From Figure 4.30, we see that without density, we lose all non-dilute behavior as the breakthrough curve for every displacement experiment becomes similar to the dilute breakthrough curve. The molecular diffusion, activity, and viscosity are still variable in these simulations and contribute to the minor differences in the breakthrough curves. The same conclusions can be drawn from the breakthrough curves for the higher Re experiments (Figure 4.31). The non-dilute breakthrough curves collapse down to the dilute breakthrough curve. This shows that the density gradient is of leading order importance.

4.5.4 Macroscale Models

Recent attempts at modeling macroscale non-dilute flow and transport have used a Taylor series expansion of Fick's law to include at least one new parameter to account for non-dilute behavior (Watson et al., 2002c; Weigand et al., 2018a). For both of these macroscale models, the new parameters have been shown to be functions of the macroscale velocity, where the parameter decreases exponentially as the velocity increases (Watson et al., 2002c; Weigand et al., 2017). From this work, we observed that as the flow rate increases for the non-dilute displacements, the microscale flow field in the direction opposite to the gravity vector transitions from a distribution with negative velocities and a large variance to an exponential like distribution with a reduced variance as compared to dilute simulations. This is in agreement with the findings that dispersion decreases as the macroscale velocity increases and explains why the non-dilute model parameters are functions of the macroscale velocity.

Macroscale dispersion is however not solely a function of the macroscale velocity and a fitting parameter. The gravity number should also be included in macroscale models because it quantifies the amount of gravity stabilization that occurs for a given macroscale velocity and includes the density differences. Ergorov (Landman et al., 2007a) developed a model that was parameter free and included the gravity number but the model was unable to correctly describe macroscale non-dilute transport. The continued use of microscale simulations to increase our understanding of non-dilute behavior will be necessary for the development of high-fidelity macroscale models where the parameters are tied to the microscale physics.

4.6 Conclusions

This work is the first step in obtaining a fundamental understanding of microscale non-dilute flow and transport that can lead to improved and parameterized closure relations for macroscale models. From this work, we conclude that

- Microscale modeling is an efficient and effective tool for advancing a fundamental understanding of complex non-dilute behavior. Microscale modeling approaches are the preferred route for obtaining a mechanistic understanding as compared to macroscale laboratory experiments.
- Non-dilute behavior can produce macroscale breakthrough curves that can be more or less disperse than dilute breakthrough curves at the same operating conditions. Additionally, an increase in the incoming salt mass fraction does not necessarily result in a sharper macroscale breakthrough curve.
- Density gradients are of leading order importance for non-dilute flow and transport. At low Reynolds and Peclet numbers, the chemical activity and viscosity can also affect macroscale breakthrough curves.
- Gravity stabilization can result in negative microscale velocities in the mean direction of flow or a reduced variance in the mean direction of flow dependent on operating conditions.
- Asymmetric non-dilute macroscale breakthrough curves are due to non-linear density functions and not a result of chemical activity.
- The importance of viscosity needs to be further analyzed.

CHAPTER 5: CONCLUSIONS

5.1 Conclusions

The research presented herein focused on improving the understanding of non-dilute flow and transport at both the micro- and macroscale, as well as developing a more computationally efficient numerical method to solve models that simulate non-dilute flow and transport at the macroscale. The macroscale model was formulated using the TCAT approach and thus has all the benefits of a TCAT model such as a connection between all spatial scales, explicit assumptions, and an entropy production rate that was used to derive closure relations. The entropy production rate was also used to develop a new numerical approach that improved computational efficiency as compared to the low-order methods that are commonly used to solve macroscale models for non-dilute flow and transport. This approach connects physical behavior to the numerical approximation to obtain a more accurate solution. Microscale simulations were performed to provide mechanistic insight into non-dilute flow and transport in porous media. Simulation results were used to explain observed experimental results in light of underlying mechanisms.

When the macroscale TCAT model was developed, no microscale simulations had been performed for non-dilute flow and transport in porous media and the closure coefficients were based on empirical observations. Developing parameterized closure coefficients for high-fidelity macroscale models, regardless of the methodology used to develop that model, is more successful when a microscale understanding and quantification of microscale behavior is available. Closure relations based on macroscale empirical evidence can limit the utility of the model as the model must be verified for every application and system.

The TCAT approach for model formulation has many attractive features that can be seen in this work. While the ultimate goal of TCAT is to develop improved larger scale models, the benefits of the approach, specifically the entropy production rate and firm connection between spatial scales, can also be used to improve numerical methods and allow for subscale modeling. With the traditional approach

to model formulation, where equations are posed directly at the scale of interest and thermodynamics are ignored, only larger scales equations are derived and the opportunities such as improved numerical approximations based on entropy production and an approach to obtain a mechanistic understanding from microscale simulations are unavailable.

5.2 Future Work

Improved parameterizations of the closure coefficients are needed for the macroscale model and should be based on the insight gained from microscale modeling work. This includes the applicability of Darcy's law for non-dilute flow at the macroscale. The literature suggests that Darcy's law is valid and is used in all existing closed macroscale models (Watson et al., 2002a), however, the methods used to determine the validity of Darcy's law are questionable as the work was conducted at the macroscale and assumed a sharp interface. Once the closure coefficients are better parameterized, the macroscale model should be extended for multiple dimensions.

Microscale simulations are preferred over any additional laboratory experiments to gain insight on non-dilute behavior. Laboratory experiments can be used to further validate the macroscale models but they are more prone to error than averaged microscale simulations. Additional microscale work should include simulations with different porous media types, larger Reynolds and Peclet numbers as well as lower gravity number experiments. Dilute microscale work has shown non-Fickian behavior for different porous media types and higher Reynolds numbers than considered in this work, where we only observed Fickian behavior. How non-dilute flow and transport would change for a porous media where dilute non-Fickian transport can occur is unknown and should be examined. Different density, viscosity, and molecular diffusion relations should also be explored as well as alternative boundary conditions. The effects of viscosity were found to be unimportant in this work for non-dilute transport, but this was due to the choice of boundary conditions. The nonlinear density function caused asymmetric breakthrough curves that may not exist for other density functions and this should be examined.

Extensions for the TCAT viscosity approach include using the conservative form of the transport equation. This allows for a more direct comparison of the TCAT viscosity approach to the EV approach. While the fitting parameter in the TCAT viscosity method was found to not vary between

experiments, additional tests cases should be performed. Ideally, an alternative formulation could be developed where the numerical approach is no longer dependent on a fitting parameter. The use of the TCAT viscosity approach for a different TCAT model and entropy production function would effectively test the robustness of the numerical scheme.

APPENDIX 1: DETAILED TCAT NON-DILUTE MODEL FORMULATION

The model formulation is based on the macroscale model derived by Gray and Miller (2009) using an entity-based momentum approach where the fluid phase, w, consists of a binary system containing two constituents, A and B, where A is defined as the salt and the water as constituent B. Following the formulation based on TCAT (Gray and Miller, 2005, 2014), we obtain the following simplified entropy inequality (SEI)

$$\begin{aligned}
&\frac{1}{\theta^{\overline{\overline{w}}}}\left(\epsilon^{\overline{\overline{w}}}p^{w}\mathbf{I}+\epsilon^{\overline{\overline{w}}}\mathbf{t}^{\overline{\overline{w}}}\right):\mathbf{d}^{\overline{\overline{w}}}-\frac{1}{\theta^{\overline{\overline{w}}}}\epsilon^{\overline{\overline{w}}}\rho^{w}\omega^{A\overline{w}}\mathbf{u}^{\overline{\overline{Aw}}}\cdot\nabla\left(\mu^{\overline{Aw}}+\psi^{\overline{Aw}}-\mu^{\overline{Bw}}-\psi^{\overline{Bw}}\right)\\
&\quad-\left\{\sum_{i\in\mathcal{I}_s}\left[\epsilon^{\overline{\overline{w}}}\rho^{w}\omega^{i\overline{w}}\nabla\left(\mu^{\overline{iw}}+\psi^{\overline{iw}}\right)+\epsilon^{\overline{\overline{w}}}\rho^{w}\omega^{i\overline{w}}\mathbf{g}^{\overline{iw}}\right]-\nabla\left(\epsilon^{\overline{\overline{w}}}p^{w}\right)+\overset{ws\rightarrow w}{\mathbf{T}}\right\}\cdot\frac{\mathbf{v}^{\overline{w},\overline{s}}}{\theta^{\overline{\overline{w}}}}\\
&\quad=\Lambda\geq 0\ ,
\end{aligned}\tag{A.106}$$

where the identity

$$\omega^{A\overline{w}}\mathbf{u}^{\overline{\overline{Aw}}}+\omega^{B\overline{w}}\mathbf{u}^{\overline{\overline{Bw}}}=0\tag{A.107}$$

has been used to derive Eqn (A.106) for this binary species system and $\theta^{\overline{\overline{w}}}$ is the temperature, $\mathbf{I}$ is the identity tensor, $\mathbf{d}^{\overline{\overline{w}}}$ is the rate of strain tensor, $\mathbf{t}^{\overline{\overline{w}}}$ is the stress tensor, $\mathbf{u}^{\overline{\overline{Aw}}}$ is the dispersion vector of species A, $\mu^{\overline{Aw}}$ is the chemical potential of species A, $\psi^{\overline{Aw}}$ is the gravitational potential of species A, $\mathcal{I}_s$ is the index set of species, $\mathbf{g}^{\overline{iw}}$ is the body force potential acting on species i, $\overset{ws\rightarrow w}{\mathbf{T}}$ is the momentum transfer from species i to the water phase, $\mathbf{v}^{\overline{w},\overline{s}}$ is the velocity of the water phase relative to the solid phase, and Λ is the entropy production rate density.

Closure relations can be posited directly from the given form of the SEI, however, chemical potentials are not convenient quantities to use for this work. The chemical potentials can be transformed to more convenient quantities using the macroscale Gibbs-Duhem equation as well as other relations for a binary species system. The macroscale Gibbs-Duhem equation for the w phase can be written for the isothermal case as

$$\sum_{i\in\mathcal{I}_s}\rho^{w}\omega^{i\overline{w}}\nabla\mu^{\overline{iw}}-\nabla p^{w}+\left\langle\sum_{i\in\mathcal{I}_s}\rho_{w}\omega_{iw}\nabla\left(\mu_{iw}-\mu^{\overline{iw}}\right)-\nabla\left(p_{w}-p^{w}\right)\right\rangle_{\Omega_w,\Omega_w}=0\ ,\tag{A.108}$$

and for a body force due to gravity we have

$$\sum_{i\in\mathcal{I}_s}\rho^w\omega^{i\overline{w}}\nabla\psi^{\overline{iw}}+\rho^w\mathbf{g}^{\overline{w}}+\left\langle\sum_{i\in\mathcal{I}_s}\rho_w\omega_{iw}\nabla\left(\psi_{iw}-\psi^{\overline{iw}}\right)\right\rangle_{\Omega_w,\Omega_w}=0\ . \tag{A.109}$$

The angled brackets, as well the subscripts after the brackets, shown Equations A.108 and A.109 represent a formula for an average of microscale quantities. The definition of the formal average can be found in Gray and Miller (2014).

The summation of these two relations yields

$$\begin{aligned}&\sum_{i\in\mathcal{I}_s}\rho^w\omega^{i\overline{w}}\nabla\left(\mu^{\overline{iw}}+\psi^{\overline{iw}}\right)-\nabla p^w+\rho^w\mathbf{g}^{\overline{w}}\\&\quad+\left\langle\sum_{i\in\mathcal{I}_s}\rho_w\omega_{iw}\nabla\left(\mu_{iw}-\mu^{\overline{iw}}+\psi_{iw}-\psi^{\overline{iw}}\right)-\nabla\left(p_w-p^w\right)\right\rangle_{\Omega_w,\Omega_w}=0\end{aligned} \tag{A.110}$$

As an initial approximation, we will assume that the deviations between the microscale and macroscale potentials are negligible. The pressure deviation term in Eqn (A.110) can be approximated as

$$\left\langle\nabla\left(p_w-p^w\right)\right\rangle_{\Omega_w,\Omega_w}\approx\hat{R}^p\nabla\epsilon^{\overline{\overline{w}}}\ . \tag{A.111}$$

The SEI then becomes

$$\begin{aligned}&\frac{1}{\theta^{\overline{\overline{w}}}}\left(\epsilon^{\overline{\overline{w}}}p^w\mathbf{I}+\epsilon^{\overline{\overline{w}}}\mathbf{t}^{\overline{\overline{w}}}\right):\mathbf{d}^{\overline{\overline{w}}}-\frac{1}{\theta^{\overline{\overline{w}}}}\epsilon^{\overline{\overline{w}}}\rho^w\omega^{A\overline{w}}\mathbf{u}^{\overline{\overline{Aw}}}\cdot\nabla\left(\mu^{\overline{Aw}}+\psi^{\overline{Aw}}-\mu^{\overline{Bw}}-\psi^{\overline{Bw}}\right)\\&\quad-\left\{\sum_{i\in\mathcal{I}_s}\epsilon^{\overline{\overline{w}}}\rho^w\omega^{i\overline{w}}\mathbf{g}^{\overline{iw}}+\epsilon^{\overline{\overline{w}}}\nabla p^w-\epsilon^{\overline{\overline{w}}}\rho^w\mathbf{g}^{\overline{w}}+\epsilon^{\overline{\overline{w}}}\hat{R}^p\nabla\epsilon^{\overline{\overline{w}}}\right.\\&\quad\left.-\nabla\left(\epsilon^{\overline{\overline{w}}}p^w\right)+\overset{ws\to w}{\mathbf{T}}\right\}\cdot\frac{\mathbf{v}^{\overline{w},\overline{s}}}{\theta^{\overline{\overline{w}}}}=\Lambda\geq0\ ,\end{aligned} \tag{A.112}$$

which can be simplified for a constant gravity force independent of species to

$$\begin{aligned}&\frac{1}{\theta^{\overline{\overline{w}}}}\left(\epsilon^{\overline{\overline{w}}}p^w\mathbf{I}+\epsilon^{\overline{\overline{w}}}\mathbf{t}^{\overline{\overline{w}}}\right):\mathbf{d}^{\overline{\overline{w}}}-\frac{1}{\theta^{\overline{\overline{w}}}}\epsilon^{\overline{\overline{w}}}\rho^w\omega^{A\overline{w}}\mathbf{u}^{\overline{\overline{Aw}}}\cdot\nabla\left(\mu^{\overline{Aw}}+\psi^{\overline{Aw}}-\mu^{\overline{Bw}}-\psi^{\overline{Bw}}\right)\\&\quad-\left\{\epsilon^{\overline{\overline{w}}}\hat{R}^p\nabla\epsilon^{\overline{\overline{w}}}-p^w\nabla\epsilon^{\overline{\overline{w}}}+\overset{ws\to w}{\mathbf{T}}\right\}\cdot\frac{\mathbf{v}^{\overline{w},\overline{s}}}{\theta^{\overline{\overline{w}}}}\\&\quad=\Lambda\geq0\ ,\end{aligned} \tag{A.113}$$

The sum of the Gibbs-Duhem equation and the gravitational potential equation for a species in the w phase can be written as

$$\begin{aligned}
&\rho^w\omega^{i\overline{w}}\nabla\left(\mu^{\overline{iw}}+\psi^{\overline{iw}}\right)-X^{\overline{\overline{iw}}}\nabla p^w+\rho^w\omega^{i\overline{w}}\mathbf{g}^{\overline{iw}}-\rho^w\omega^{i\overline{w}}\nabla\mu^{\overline{iw}}\Big|_{p^w,\theta^{\overline{\overline{w}}}}\\
&\quad+\left\langle\rho_w\omega_{iw}\nabla\left(\mu_{iw}+\psi_{iw}-\mu^{\overline{iw}}-\psi^{\overline{iw}}\right)-\left(X_{iw}\nabla p_w-X^{\overline{\overline{iw}}}\nabla p^w\right)\right\rangle_{\Omega_w,\Omega_w}\\
&\quad-\left\langle\rho_w\omega_{iw}\nabla\left(\mu_{iw}|_{p_w,\theta_w}-\mu^{\overline{iw}}\Big|_{p^w,\theta^{\overline{\overline{w}}}}\right)\right\rangle_{\Omega_w,\Omega_w}=0\ ,
\end{aligned}\tag{A.114}$$

which can be rearranged as

$$\begin{aligned}
\nabla\left(\mu^{\overline{iw}}+\psi^{\overline{iw}}\right)&=\frac{X^{\overline{\overline{iw}}}}{\rho^w\omega^{i\overline{w}}}\nabla p^w-\mathbf{g}^{\overline{iw}}+\nabla\mu^{\overline{iw}}\Big|_{p^w,\theta^{\overline{\overline{w}}}}\\
&\quad-\frac{1}{\rho^w\omega^{i\overline{w}}}\left\langle\rho_w\omega_{iw}\nabla\left(\mu_{iw}+\psi_{iw}-\mu^{\overline{iw}}-\psi^{\overline{iw}}\right)-\left(X_{iw}\nabla p_w-X^{\overline{\overline{iw}}}\nabla p^w\right)\right\rangle_{\Omega_w,\Omega_w}\\
&\quad+\frac{1}{\rho^w\omega^{i\overline{w}}}\left\langle\rho_w\omega_{iw}\nabla\left(\mu_{iw}|_{p_w,\theta_w}-\mu^{\overline{iw}}\Big|_{p^w,\theta^{\overline{\overline{w}}}}\right)\right\rangle_{\Omega_w,\Omega_w}\ .
\end{aligned}\tag{A.115}$$

where $X^{\overline{\overline{iw}}}$ is the partial mass volume fraction of species i and $\nabla\mu^{\overline{iw}}\Big|_{p^w,\theta^{\overline{\overline{w}}}}$ is the gradient of the chemical potential of species i with the density and temperature of the water phase held constant.

The deviations between the microscale and macroscale potentials are assumed to be negligible. We also assume the product terms in the average of deviation pressures are separable. This produces

$$\nabla\left(\mu^{\overline{iw}}+\psi^{\overline{iw}}\right)\ =\ \frac{X^{\overline{\overline{iw}}}}{\rho^w\omega^{i\overline{w}}}\nabla p^w\ -\ \mathbf{g}^{\overline{iw}}\ +\ \nabla\mu^{\overline{iw}}\Big|_{p^w,\theta^{\overline{\overline{w}}}}\ +\ \frac{X^{\overline{\overline{iw}}}}{\rho^w\omega^{i\overline{w}}}\left\langle\nabla p_w-\nabla p^w\right\rangle_{\Omega_w,\Omega_w}\tag{A.116}$$

For a two species system, where there the gravity force is constant and independent of species and using Eqn (A.111), we have

$$\begin{aligned}
\nabla\left(\mu^{\overline{Aw}}+\psi^{\overline{Aw}}-\mu^{\overline{Bw}}-\psi^{\overline{Bw}}\right)&=\nabla\mu^{\overline{Aw}}\Big|_{p^w,\theta^{\overline{\overline{w}}}}-\nabla\mu^{\overline{Bw}}\Big|_{p^w,\theta^{\overline{\overline{w}}}}\\
&\quad+\frac{X^{\overline{\overline{Aw}}}-\omega^{A\overline{w}}}{\rho^w\omega^{A\overline{w}}\omega^{B\overline{w}}}\left(\nabla p^w+\hat{R}^p\nabla\epsilon^{\overline{\overline{w}}}\right)
\end{aligned}\tag{A.117}$$

The chemical potential is defined as

$$\mu^{\overline{iw}}\Big|_{p^w,\theta^{\overline{\overline{w}}}} = \mu_0^{\overline{iw}}(p^w,\theta^{\overline{\overline{w}}})\Big|_{p^w,\theta^{\overline{\overline{w}}}} + \frac{R_G\theta^{\overline{\overline{w}}}}{MW_i}\ln\left(x^{\overline{\overline{iw}}}\hat{\gamma}^{\overline{\overline{iw}}}\right), \tag{A.118}$$

and the gradient of the chemical potential as

$$\nabla\,\mu^{\overline{iw}}\Big|_{p^w,\theta^{\overline{\overline{w}}}} = \frac{R_G\theta^{\overline{\overline{w}}}}{MW_i\hat{\gamma}^{\overline{\overline{iw}}}}\nabla\hat{\gamma}^{\overline{\overline{iw}}}\Big|_{p^w,\theta^{\overline{\overline{w}}}} + \frac{R_G\theta^{\overline{\overline{w}}}}{MW_i x^{\overline{\overline{iw}}}}\nabla x^{\overline{\overline{iw}}}\Big|_{p^w,\theta^{\overline{\overline{w}}}}. \tag{A.119}$$

The following two relations for a binary system will also be used:

$$\nabla x^{\overline{\overline{Aw}}} = -\nabla x^{\overline{\overline{Bw}}} \tag{A.120}$$

and

$$\hat{\gamma}^{\overline{\overline{Bw}}}\nabla\left(\hat{\gamma}^{\overline{\overline{Aw}}}x^{\overline{\overline{Aw}}}\right)\Big|_{p^w,\theta^{\overline{\overline{w}}}} + \hat{\gamma}^{\overline{\overline{Aw}}}\nabla\left(\hat{\gamma}^{\overline{\overline{Bw}}}x^{\overline{\overline{Bw}}}\right)\Big|_{p^w,\theta^{\overline{\overline{w}}}} = 0\,. \tag{A.121}$$

The gradient of the chemical potentials, which can be seen in Eqn (A.117), can then be transformed into the following form

$$\begin{aligned}\nabla\mu^{\overline{Aw}}\Big|_{p^w,\theta^{\overline{\overline{w}}}} - \nabla\mu^{\overline{Bw}}\Big|_{p^w,\theta^{\overline{\overline{w}}}} = R_G\theta^{\overline{\overline{w}}}\Bigg[&\left(\frac{1}{MW_A x^{\overline{\overline{Aw}}}} + \frac{1}{MW_B x^{\overline{\overline{Bw}}}}\right)\nabla x^{\overline{\overline{Aw}}} \\ &+ \left(\frac{1}{MW_A\hat{\gamma}^{\overline{\overline{Aw}}}} + \frac{x^{\overline{\overline{Aw}}}}{MW_B\hat{\gamma}^{\overline{\overline{Aw}}}x^{\overline{\overline{Bw}}}}\right)\nabla\hat{\gamma}^{\overline{\overline{Aw}}}\Bigg]\,.\end{aligned} \tag{A.122}$$

To convert the mole fraction to mass fraction, we use the following relation

$$\nabla x^{\overline{\overline{Aw}}} = \left(\frac{MW_w^2}{MW_A MW_B}\right)\nabla\omega^{A\overline{w}}, \tag{A.123}$$

where the molecular weight of the solution (MW_w) is defined as

$$MW_W = x^{\overline{\overline{Aw}}}MW_A + x^{\overline{\overline{Bw}}}MW_B = \left(\frac{\omega^{A\overline{w}}}{MW_A} + \frac{\omega^{B\overline{w}}}{MW_B}\right)^{-1}. \tag{A.124}$$

The gradients of the chemical potentials then becomes

$$\nabla\mu^{\overline{Aw}}\Big|_{p^w,\theta^{\overline{\overline{w}}}} - \nabla\mu^{\overline{Bw}}\Big|_{p^w,\theta^{\overline{\overline{w}}}} =$$
$$R_G\theta^{\overline{\overline{w}}}\left[\left(\frac{1}{MW_A x^{\overline{\overline{Aw}}}} + \frac{1}{MW_B x^{\overline{\overline{Bw}}}}\right)\left(\frac{MW_w^2}{MW_A MW_B}\right)\nabla\omega^{A\overline{w}}\right.$$
$$\left. + \left(\frac{1}{MW_A\hat{\gamma}^{\overline{\overline{Aw}}}} + \frac{x^{\overline{\overline{Aw}}}}{MW_B\hat{\gamma}^{\overline{\overline{Aw}}}x^{\overline{\overline{Bw}}}}\right)\nabla\hat{\gamma}^{\overline{\overline{Aw}}}\right] . \tag{A.125}$$

Inserting Eqns (A.117) and (A.125) into the SEI, we have

$$\frac{1}{\theta^{\overline{\overline{w}}}}\left(\epsilon^{\overline{\overline{w}}}p^w\mathbf{I} + \epsilon^{\overline{\overline{w}}}\mathbf{t}^{\overline{\overline{w}}}\right):\mathbf{d}^{\overline{\overline{w}}}$$
$$- \frac{1}{\theta^{\overline{\overline{w}}}}\epsilon^{\overline{\overline{w}}}\rho^w\omega^{A\overline{w}}\mathbf{u}^{\overline{\overline{Aw}}}\cdot\left\{\frac{X^{\overline{\overline{Aw}}} - \omega^{A\overline{w}}}{\rho^w\omega^{A\overline{w}}\omega^{B\overline{w}}}\left(\nabla p^w + \hat{R}^p\nabla\epsilon^{\overline{\overline{w}}}\right)\right.$$
$$+R_G\theta^{\overline{\overline{w}}}\left[\left(\frac{1}{MW_A x^{\overline{\overline{Aw}}}} + \frac{1}{MW_B x^{\overline{\overline{Bw}}}}\right)\left(\frac{MW_w^2}{MW_A MW_B}\right)\nabla\omega^{A\overline{w}}\right.$$
$$\left.\left. + \left(\frac{1}{MW_A\hat{\gamma}^{\overline{\overline{Aw}}}} + \frac{x^{\overline{\overline{Aw}}}}{MW_B\hat{\gamma}^{\overline{\overline{Aw}}}x^{\overline{\overline{Bw}}}}\right)\nabla\hat{\gamma}^{\overline{\overline{Aw}}}\right]\right\}$$
$$- \left\{\epsilon^{\overline{\overline{w}}}\hat{R}^p\nabla\epsilon^{\overline{\overline{w}}} - p^w\nabla\epsilon^{\overline{\overline{w}}} + \overset{ws\to w}{\mathbf{T}}\right\}\cdot\frac{\mathbf{v}^{\overline{w},\overline{s}}}{\theta^{\overline{\overline{w}}}}$$
$$= \Lambda \geq 0 , \tag{A.126}$$

For the case of constant porosity, the SEI becomes

$$\frac{1}{\theta^{\overline{\overline{w}}}}\left(\epsilon^{\overline{\overline{w}}}p^w\mathbf{I} + \epsilon^{\overline{\overline{w}}}\mathbf{t}^{\overline{\overline{w}}}\right):\mathbf{d}^{\overline{\overline{w}}}$$
$$- \frac{1}{\theta^{\overline{\overline{w}}}}\epsilon^{\overline{\overline{w}}}\rho^w\omega^{A\overline{w}}\mathbf{u}^{\overline{\overline{Aw}}}\cdot\left\{\frac{X^{\overline{\overline{Aw}}} - \omega^{A\overline{w}}}{\rho^w\omega^{A\overline{w}}\omega^{B\overline{w}}}\nabla p^w\right.$$
$$+R_G\theta^{\overline{\overline{w}}}\left[\left(\frac{1}{MW_A x^{\overline{\overline{Aw}}}} + \frac{1}{MW_B x^{\overline{\overline{Bw}}}}\right)\left(\frac{MW_w^2}{MW_A MW_B}\right)\nabla\omega^{A\overline{w}}\right.$$
$$\left.\left. + \left(\frac{1}{MW_A\hat{\gamma}^{\overline{\overline{Aw}}}} + \frac{x^{\overline{\overline{Aw}}}}{MW_B\hat{\gamma}^{\overline{\overline{Aw}}}x^{\overline{\overline{Bw}}}}\right)\nabla\hat{\gamma}^{\overline{\overline{Aw}}}\right]\right\}$$
$$- \overset{ws\to w}{\mathbf{T}}\cdot\frac{\mathbf{v}^{\overline{w},\overline{s}}}{\theta^{\overline{\overline{w}}}} = \Lambda \geq 0 , \tag{A.127}$$

Eqn (A.127) includes three terms in force-flux form, which will be considered in turn. For the first term, we will use a zero-order closure, which leads to a flux that is independent of the conjugate force

that can be written as

$$\mathbf{t}^{\overline{\overline{w}}} = -p^{w}\mathbf{I} \; . \tag{A.128}$$

Eqn (A.128) is a standard macroscale inviscid flow approximation. Momentum transfer from the water phase to the water-solid interface is likely to be the dominant process, and at the macroscale the flow velocity is invariant at steady state. This is equivalent to neglecting wall effects.

The second term requiring an approximation is the term $\mathbf{u}^{\overline{\overline{Aw}}}$, which is defined as the macroscale deviation from the mass-averaged velocity for species A. A variety of physicochemical mechanisms can result in this deviation velocity. These include, molecular diffusion, and variations in flow caused by not only the pore morphology and topology but also variations in fluid density, viscosity, and activity. Thus some of these mechanisms are related to solution properties and some are related to variations in fluid flow. We will depart from previous closure approximations of this model (Gray and Miller, 2009) by using cross-coupled approximations in terms of forces yielding the approximations

$$\begin{aligned}
\omega^{A\overline{w}}\mathbf{u}^{\overline{\overline{Aw}}} = -x^{\overline{\overline{Aw}}}x^{\overline{\overline{Bw}}}\hat{\mathbf{D}}_{u}^{Aw}\cdot\Bigg\{ & \frac{X^{\overline{\overline{Aw}}} - \omega^{A\overline{w}}}{\rho^{w}\omega^{A\overline{w}}\omega^{B\overline{w}}}\nabla p^{w} \\
& + R_G\theta^{\overline{\overline{w}}}\Bigg[\left(\frac{1}{MW_A x^{\overline{\overline{Aw}}}} + \frac{1}{MW_B x^{\overline{\overline{Bw}}}}\right)\left(\frac{MW_w^2}{MW_A MW_B}\right)\nabla\omega^{A\overline{w}} \\
& + \left(\frac{1}{MW_A\hat{\gamma}^{\overline{\overline{Aw}}}} + \frac{x^{\overline{\overline{Aw}}}}{MW_B\hat{\gamma}^{\overline{\overline{Aw}}}x^{\overline{\overline{Bw}}}}\right)\nabla\hat{\gamma}^{\overline{\overline{Aw}}}\Bigg]\Bigg\} - \hat{\mathbf{R}}_{u}^{Aw}\cdot\mathbf{v}^{\overline{w},\overline{s}}
\end{aligned} \tag{A.129}$$

and

$$\begin{aligned}
{}^{ws\to w}\mathbf{T} = -x^{\overline{\overline{Aw}}}x^{\overline{\overline{Bw}}}\hat{\mathbf{D}}_{v}^{Aw}\cdot\Bigg\{ & \frac{X^{\overline{\overline{Aw}}} - \omega^{A\overline{w}}}{\rho^{w}\omega^{A\overline{w}}\omega^{B\overline{w}}}\nabla p^{w} \\
& + R_G\theta^{\overline{\overline{w}}}\Bigg[\left(\frac{1}{MW_A x^{\overline{\overline{Aw}}}} + \frac{1}{MW_B x^{\overline{\overline{Bw}}}}\right)\left(\frac{MW_w^2}{MW_A MW_B}\right)\nabla\omega^{A\overline{w}} \\
& + \left(\frac{1}{MW_A\hat{\gamma}^{\overline{\overline{Aw}}}} + \frac{x^{\overline{\overline{Aw}}}}{MW_B\hat{\gamma}^{\overline{\overline{Aw}}}x^{\overline{\overline{Bw}}}}\right)\nabla\hat{\gamma}^{\overline{\overline{Aw}}}\Bigg]\Bigg\} - \hat{\mathbf{R}}_{v}^{Aw}\cdot\mathbf{v}^{\overline{w},\overline{s}}
\end{aligned} \tag{A.130}$$

where $\hat{\mathbf{D}}_{u}^{Aw}$, $\hat{\mathbf{R}}_{u}^{Aw}$, $\hat{\mathbf{D}}_{v}^{Aw}$ and $\hat{\mathbf{R}}_{v}^{Aw}$ are second-order, cross-coupled closure tensors. The addition of the product of the mole fractions ensures that the model reduces properly in the dilute limit. The equations we wish to close are the conservation of mass equations for the w phase and the case of no mass

exchange among entities given by

$$\frac{\mathrm{D}^{\overline{w}}\left(\epsilon^{\overline{\overline{w}}}\rho^{w}\omega^{A\overline{w}}\right)}{\mathrm{D}t}+\epsilon^{\overline{\overline{w}}}\rho^{w}\omega^{A\overline{w}}\mathbf{I}\mathbf{:}\mathbf{d}^{\overline{\overline{w}}}+\nabla\cdot\left(\epsilon^{\overline{\overline{w}}}\rho^{w}\omega^{A\overline{w}}\mathbf{u}^{\overline{\overline{Aw}}}\right)=0\ , \tag{A.131}$$

where $\frac{\mathrm{D}^{\overline{w}}}{\mathrm{D}t}$ is the material derivative with respect to the water phase. This can be summed over both species yielding

$$\frac{\mathrm{D}^{\overline{w}}\left(\epsilon^{\overline{\overline{w}}}\rho^{w}\right)}{\mathrm{D}t}+\epsilon^{\overline{\overline{w}}}\rho^{w}\mathbf{I}\mathbf{:}\mathbf{d}^{\overline{\overline{w}}}=0\ , \tag{A.132}$$

and the conservation of momentum equation for the w phase given by

$$\frac{\mathrm{D}^{\overline{w}}\left(\epsilon^{\overline{\overline{w}}}\rho^{w}\mathbf{v}^{\overline{w}}\right)}{\mathrm{D}t}+\epsilon^{\overline{\overline{w}}}\rho^{w}\mathbf{v}^{\overline{w}}\mathbf{I}\mathbf{:}\mathbf{d}^{\overline{\overline{w}}}-\nabla\cdot\left(\epsilon^{\overline{\overline{w}}}\mathbf{t}^{\overline{\overline{w}}}\right)-\sum_{i\in\mathbb{J}_{s}}\epsilon^{\overline{\overline{w}}}\rho^{w}\omega^{i\overline{w}}\mathbf{g}^{i\overline{w}}-{}^{ws\rightarrow w}\mathbf{T}=0\ . \tag{A.133}$$

Inserting Eqns (A.128) and (A.130) into Eqn (A.133), where we have assumed the porosity is constant and the gravitational force is constant and independent of species, yields

$$\begin{aligned}&\frac{\mathrm{D}^{\overline{w}}\left(\epsilon^{\overline{\overline{w}}}\rho^{w}\mathbf{v}^{\overline{w}}\right)}{\mathrm{D}t}+\epsilon^{\overline{\overline{w}}}\rho^{w}\mathbf{v}^{\overline{w}}\mathbf{I}\mathbf{:}\mathbf{d}^{\overline{\overline{w}}}+\epsilon^{\overline{\overline{w}}}\nabla p^{w}-\epsilon^{\overline{\overline{w}}}\rho^{w}\mathbf{g}^{\overline{w}}+x^{\overline{\overline{Aw}}}x^{\overline{\overline{Bw}}}\hat{\mathbf{D}}_{v}^{Aw}\cdot\left\{\frac{X^{\overline{\overline{Aw}}}-\omega^{A\overline{w}}}{\rho^{w}\omega^{A\overline{w}}\omega^{B\overline{w}}}\nabla p^{w}\right.\\&+R_{G}\theta^{\overline{\overline{w}}}\left[\left(\frac{1}{MW_{A}x^{\overline{\overline{Aw}}}}+\frac{1}{MW_{B}x^{\overline{\overline{Bw}}}}\right)\left(\frac{MW_{w}^{2}}{MW_{A}MW_{B}}\right)\nabla\omega^{A\overline{w}}\right.\\&\left.\left.+\left(\frac{1}{MW_{A}\hat{\gamma}^{\overline{\overline{Aw}}}}+\frac{x^{\overline{\overline{Aw}}}}{MW_{B}\hat{\gamma}^{\overline{\overline{Aw}}}x^{\overline{\overline{Bw}}}}\right)\nabla\hat{\gamma}^{\overline{\overline{Aw}}}\right]\right\}+\hat{\mathbf{R}}_{v}^{Aw}\cdot\mathbf{v}^{\overline{w},\overline{s}}=0\ .\end{aligned} \tag{A.134}$$

Eqn (A.132) can be used to simplify Eqn (A.134) to

$$\begin{aligned}&\epsilon^{\overline{\overline{w}}}\rho^{w}\frac{\mathrm{D}^{\overline{w}}\mathbf{v}^{\overline{w}}}{\mathrm{D}t}+\epsilon^{\overline{\overline{w}}}\nabla p^{w}-\epsilon^{\overline{\overline{w}}}\rho^{w}\mathbf{g}^{\overline{w}}+x^{\overline{\overline{Aw}}}x^{\overline{\overline{Bw}}}\hat{\mathbf{D}}_{v}^{Aw}\cdot\left\{\frac{X^{\overline{\overline{Aw}}}-\omega^{A\overline{w}}}{\rho^{w}\omega^{A\overline{w}}\omega^{B\overline{w}}}\nabla p^{w}\right.\\&+R_{G}\theta^{\overline{\overline{w}}}\left[\left(\frac{1}{MW_{A}x^{\overline{\overline{Aw}}}}+\frac{1}{MW_{B}x^{\overline{\overline{Bw}}}}\right)\left(\frac{MW_{w}^{2}}{MW_{A}MW_{B}}\right)\nabla\omega^{A\overline{w}}\right.\\&\left.\left.+\left(\frac{1}{MW_{A}\hat{\gamma}^{\overline{\overline{Aw}}}}+\frac{x^{\overline{\overline{Aw}}}}{MW_{B}\hat{\gamma}^{\overline{\overline{Aw}}}x^{\overline{\overline{Bw}}}}\right)\nabla\hat{\gamma}^{\overline{\overline{Aw}}}\right]\right\}+\hat{\mathbf{R}}_{v}^{Aw}\cdot\mathbf{v}^{\overline{w},\overline{s}}=0\ .\end{aligned} \tag{A.135}$$

Neglecting inertial terms yields

$$\epsilon^{\overline{\overline{w}}}\nabla p^w - \epsilon^{\overline{\overline{w}}}\rho^w \mathbf{g}^{\overline{w}} + x^{\overline{\overline{Aw}}}x^{\overline{\overline{Bw}}}\hat{\mathbf{D}}_v^{Aw}\cdot\left\{\frac{X^{\overline{\overline{Aw}}} - \omega^{A\overline{w}}}{\rho^w\omega^{A\overline{w}}\omega^{B\overline{w}}}\nabla p^w\right.$$
$$+R_G\theta^{\overline{\overline{w}}}\left[\left(\frac{1}{MW_A x^{\overline{\overline{Aw}}}} + \frac{1}{MW_B x^{\overline{\overline{Bw}}}}\right)\left(\frac{MW_w^2}{MW_A MW_B}\right)\nabla\omega^{A\overline{w}}\right.$$
$$\left.\left. + \left(\frac{1}{MW_A\hat{\gamma}^{\overline{\overline{Aw}}}} + \frac{x^{\overline{\overline{Aw}}}}{MW_B\hat{\gamma}^{\overline{\overline{Aw}}}x^{\overline{\overline{Bw}}}}\right)\nabla\hat{\gamma}^{\overline{\overline{Aw}}}\right]\right\} + \hat{\mathbf{R}}_v^{Aw}\cdot\mathbf{v}^{\overline{w},\overline{s}} = 0\ . \tag{A.136}$$

Eqns (A.131) and (A.129) can be combined to give

$$\frac{\mathrm{D}^{\overline{w}}\left(\epsilon^{\overline{\overline{w}}}\rho^w\omega^{A\overline{w}}\right)}{\mathrm{D}t} + \epsilon^{\overline{\overline{w}}}\rho^w\omega^{A\overline{w}}\mathbf{I}\!:\!\mathbf{d}^{\overline{\overline{w}}} - \nabla\cdot\left(\epsilon^{\overline{\overline{w}}}\rho^w\hat{\mathbf{R}}_u^{Aw}\cdot\mathbf{v}^{\overline{w},\overline{s}}\right)$$
$$- \nabla\cdot\left[\epsilon^{\overline{\overline{w}}}\rho^w x^{\overline{\overline{Aw}}}x^{\overline{\overline{Bw}}}\hat{\mathbf{D}}_u^{Aw}\cdot\left(\frac{X^{\overline{\overline{Aw}}} - \omega^{A\overline{w}}}{\rho^w\omega^{A\overline{w}}\omega^{B\overline{w}}}\right)\nabla p^w\right]$$
$$- \nabla\cdot\left[\epsilon^{\overline{\overline{w}}}\rho^w x^{\overline{\overline{Aw}}}x^{\overline{\overline{Bw}}}R_G\theta^{\overline{\overline{w}}}\hat{\mathbf{D}}_u^{Aw}\right.$$
$$\left.\cdot\left(\frac{1}{MW_A x^{\overline{\overline{Aw}}}} + \frac{1}{MW_B x^{\overline{\overline{Bw}}}}\right)\left(\frac{MW_w^2}{MW_A MW_B}\right)\nabla\omega^{A\overline{w}}\right]$$
$$- \nabla\cdot\left[\epsilon^{\overline{\overline{w}}}\rho^w x^{\overline{\overline{Aw}}}x^{\overline{\overline{Bw}}}R_G\theta^{\overline{\overline{w}}}\hat{\mathbf{D}}_u^{Aw}\cdot\left(\frac{1}{MW_A\hat{\gamma}^{\overline{\overline{Aw}}}} + \frac{x^{\overline{\overline{Aw}}}}{MW_B\hat{\gamma}^{\overline{\overline{Aw}}}x^{\overline{\overline{Bw}}}}\right)\nabla\hat{\gamma}^{\overline{\overline{Aw}}}\right] = 0\ . \tag{A.137}$$

After manipulations and using the following relation

$$\frac{x^{\overline{\overline{Aw}}}x^{\overline{\overline{Bw}}}}{\omega^{A\overline{w}}\omega^{B\overline{w}}} = \frac{MW_W^2}{MW_A MW_B}, \tag{A.138}$$

Eqn (A.136) becomes

$$\epsilon^{\overline{\overline{w}}}\nabla p^w - \epsilon^{\overline{\overline{w}}}\rho^w\mathbf{g}^{\overline{w}} + \hat{\mathbf{R}}_v^{Aw}\cdot\mathbf{v}^{\overline{w},\overline{s}} + \left[\frac{x^{\overline{\overline{Aw}}}x^{\overline{\overline{Bw}}}}{\omega^{A\overline{w}}\omega^{B\overline{w}}}\right]\left[\left(\frac{R_G\theta^{\overline{\overline{w}}}MW_W}{MW_A MW_B}\right)\hat{\mathbf{D}}_v^{Aw}\cdot\nabla\omega^{A\overline{w}}\right.$$
$$\left. + \left(\frac{R_G\theta^{\overline{\overline{w}}}x^{\overline{\overline{Aw}}}}{MW_W\hat{\gamma}^{\overline{\overline{Aw}}}}\right)\hat{\mathbf{D}}_v^{Aw}\cdot\nabla\hat{\gamma}^{\overline{\overline{Aw}}} + \left(\frac{X^{\overline{\overline{Aw}}} - \omega^{A\overline{w}}}{\rho^w}\right)\hat{\mathbf{D}}_v^{Aw}\cdot\nabla p^w\right] = 0\ . \tag{A.139}$$

and Eqn (A.137) becomes

$$\frac{\partial\left(\epsilon^{\overline{\overline{w}}}\rho^w\omega^{A\overline{w}}\right)}{\partial t} + \nabla\cdot\left[\epsilon^{\overline{\overline{w}}}\rho^w\left(\omega^{A\overline{w}}\mathbf{I} - \hat{\mathbf{R}}_u^{Aw}\right)\cdot\mathbf{v}^{\overline{w},\overline{s}}\right]$$

$$
\begin{aligned}
&- \nabla\cdot\left\{\epsilon^{\overline{\overline{w}}}\rho^{w}\left[\frac{x^{\overline{\overline{Aw}}}\left(1-x^{\overline{\overline{Aw}}}\right)}{\omega^{A\overline{w}}\left(1-\omega^{A\overline{w}}\right)}\right]\left[\left(\frac{X^{\overline{\overline{Aw}}}-\omega^{A\overline{w}}}{\rho^{w}}\right)\hat{\mathbf{D}}_{u}^{Aw}\cdot\nabla p^{w}\right.\right.\\
&\left.\left.+\left(\frac{R_G\theta^{\overline{\overline{w}}}MW_W}{MW_AMW_B}\right)\hat{\mathbf{D}}_{u}^{Aw}\cdot\nabla\omega^{A\overline{w}}+\left(\frac{R_G\theta^{\overline{\overline{w}}}x^{\overline{\overline{Aw}}}}{MW_W\hat{\gamma}^{\overline{\overline{Aw}}}}\right)\hat{\mathbf{D}}_{u}^{Aw}\cdot\nabla\hat{\gamma}^{\overline{\overline{Aw}}}\right]\right\}=0\ . \qquad \text{(A.140)}
\end{aligned}
$$

BIBLIOGRAPHY

Aho, K., Derryberry, D., and Peterson, T. (2014). "Model selection for ecologists: the worldviews of aic and bic." *Ecology*, 95(3), 631–636.

Anderson, S. J. (1997). "An experimental investigation of high concentration displacements in saturated porous media.." Ph.D. thesis, Department of Civil Engineering, The University of Western Australia, Nedlands, Western Australia, Australia., Department of Civil Engineering, The University of Western Australia, Nedlands, Western Australia, Australia.

Andrade, J. S., Almeida, M. P., Mendes Filho, J., Havlin, S., Suki, B., and Stanley, H. E. (1997). "Fluid flow through porous media: The role of stagnant zones." *Phys. Rev. Lett.*, 79, 3901–3904.

Aramideh, S., Vlachos, P. P., and Ardekani, A. M. (2018). "Pore-scale statistics of flow and transport through porous media." *Phys. Rev. E*, 98, 013104.

Baliga, B. R. and Patankar, S. V. (1980). "A new finite-element formulation for convection-diffusion problems." *Numerical Heat Transfer*, 3(4), 393–409.

Baranau, V. and Tallarek, U. (2014). "Random-close packing limits for monodisperse and polydisperse hard spheres." *Soft Matter*, 10, 3826–3841.

Barlow, P. M. and Reichard, E. G. (2010). "Saltwater intrusion in coastal regions of north america." *Hydrogeology Journal*, 18(1), 247–260.

Bashar, K. and Tellam, J. H. (2011). "Sandstones of unexpectedly high diffusibility." *Journal of contaminant hydrology*, 122(1), 40–52.

Battiato, I., Ferrero, P. T., O'Malley, D., Miller, C. T., Takhar, P. S., Valdés-Parada, F. J., and Wood, B. D. (2019). "Theory and applications of macroscale models in porous media." *Transport in Porous Media*.

Bear, J. (1972). *Dynamics of Fluids in Porous Media*. Elsevier, New York.

Bear, J. (1979). *Hydraulics of Groundwater*. McGraw-Hill, New York.

Bear, J. (2012). *Hydraulics of groundwater*. Courier Corporation.

Bijeljic, B. and Blunt, M. J. (2007). "Pore-scale modeling of transverse dispersion in porous media." *Water Resources Research*, 43(12).

Bijeljic, B., Mostaghimi, P., and Blunt, M. J. (2011). "Signature of non-fickian solute transport in complex heterogeneous porous media." *Phys. Rev. Lett.*, 107, 204502.

Bijeljic, B., Muggeridge, A. H., and Blunt, M. J. (2004). "Pore-scale modeling of longitudinal dispersion." *Water Resources Research*, 40(11).

Bijeljic, B., Raeini, A., Mostaghimi, P., and Blunt, M. J. (2013). "Predictions of non-fickian solute transport in different classes of porous media using direct simulation on pore-scale images." *Phys. Rev. E*, 87, 013011.

Bird, R. B., Stewart, W. E., and Lightfoot, E. N. (2007). *Transport Phenomena*. John Wiley & Sons, Inc., revised 2nd edition.

Boccardo, G., Marchisio, D. L., and Sethi, R. (2014). "Microscale simulation of particle deposition in porous media." *Journal of Colloid and Interface Science*, 417, 227 – 237.

Boufadel, M. C., Suidan, M. T., and Venosa, A. D. (1999). "A numerical model for density-and-viscosity-dependent flows in two-dimensional variably saturated porous media." *Journal of Contaminant Hydrology*, 37(1), 1 – 20.

Brigham, W. E., Reed, P. W., Dew, J. N., et al. (1961). "Experiments on mixing during miscible displacement in porous media." *Society of Petroleum Engineers Journal*, 1(01), 1–8.

Broeke, L. V. D. and Krishna, R. (1995). "Experimental verification of the maxwell-stefan theory for micropore diffusion." *Chemical Engineering Science*, 50(16), 2507 – 2522.

Bruning, K. and Miller, C. T. (2019). "Toward a new generation of two-fluid flow models based on the thermodynamically-constrained averaging theory." *Water*, 11(11).

Calhoun-Lopez, M. and Gunzburger, M. D. (2006). "A finite element, multiresolution viscosity method for hyperbolic conservation laws." *SIAM Journal on Numerical Analysis*, 43(5), 1988–2011.

Carver, M. B. and Hinds, H. (1978). "The method of lines and the advective equation." *SIMULATION*, 31(2), 59–69.

Crevacore, E., Tosco, T., Sethi, R., Boccardo, G., and Marchisio, D. L. (2016). "Recirculation zones induce non-fickian transport in three-dimensional periodic porous media." *Phys. Rev. E*, 94, 053118.

Demidov, D. (2006). "Mathematical modelling of nonlinear brine transport processes." Ph.D. thesis, Kazan State Univeristy, Kazan State Univeristy.

Diersch, H. J. G. and Kolditz, O. (2002). "Variable-density flow and transport in porous media: Approaches and challenges." *Advances in Water Resources*, 25(8-12), 899–944.

Duda, A., Koza, Z., and Matyka, M. (2011). "Hydraulic tortuosity in arbitrary porous media flow." *Phys. Rev. E*, 84, 036319.

Dye, A. L., McClure, J. E., Adalsteinsson, D., and Miller, C. T. (2016). "An adaptive lattice Boltzmann scheme for modeling two-fluid-phase fow in porous medium systems." *Water Resources Research*, 52(4), 2601–2617.

Egorov, A. G., Demidov, D. E., and Schotting, R. J. (2005). "On the interaction between gravity forces and dispersive brine fronts in micro-heterogeneous porous media." *Advances in Water Resources*, 28(1), 55–68.

Evans, D. L., Drew, J. H., and Leemis, L. M. (2008). "The distribution of the kolmogorov–smirnov, cramer–von mises, and anderson–darling test statistics for exponential populations with estimated parameters." *Communications in Statistics - Simulation and Computation*, 37(7), 1396–1421.

Farthing, M. W. and Miller, C. T. (2000). "A comparison of high-resolution, finite-volume, adaptive-stencil schemes for simulating advective-dispersive transport." *Advances in Water Resources*, 24(1), 29–48.

Fernandez, J., Kurowski, P., Petitjeans, P., and Meiburg, E. (2002). "Density-driven unstable flows of miscible fluids in a hele-shaw cell." *Journal of Fluid Mechanics*, 451, 239–260.

Ferziger, J. H. and Perić, M. (2002). *Computational Methods for Fluid Dynamics*. Springer, Berlin, Germany, third edition.

Frolkovic, P. and Schepper, H. D. (2000). "Numerical modelling of convection dominated transport coupled with density driven flow in porous media." *Advances in Water Resources*, 24(1), 63 – 72.

Gablonsky, J. M. and Kelley, C. T. (2001). "A locally-biased form of the DIRECT algorithm." *Journal of Global Optimization*, 21, 27–37.

Ghanbarzadeh, S., Hesse, M. A., Prodanović, M., and Gardner, J. E. (2015). "Deformation-assisted fluid percolation in rock salt." *Science*, 350(6264), 1069–1072.

Godunov, S. K. (1959). "Finite difference method for numerical computation of discontinuous solutions of the equations of fluid dynamics." *Mat. Sb.*, 47, 428–441.

Goldberg, R. N. and Nuttall, R. L. (1978). "Evaluated activity and osmotic coefficients for aqueous solutions: The alkaline earth metal halides." *Journal of Physical and Chemical Reference Data*, 7(1), 263–310.

Gordon, A. (1937). "The diffusion constant of an electrolyte, and its relation to concentration." *The Journal of Chemical Physics*, 5(7), 522–526.

Gray, W. G., Bruning, K., and Miller, C. T. (2019). "Non-hysteretic functional form of capillary pressure in porous media." *In review*.

Gray, W. G., Dye, A. L., McClure, J. E., Pyrak-Nolte, L. J., and Miller, C. T. (2015). "On the dynamics and kinematics of two-fluid-phase flow in porous media." *Water Resources Research*, 51(7), 5365–5381.

Gray, W. G., Leijnse, A., Kolar, R. L., and Blain, C. A. (1993). *Mathematical Tools for Changing Spatial Scales in the Analysis of Physical Systems*. CRC Press, Boca Raton.

Gray, W. G. and Miller, C. T. (2005). "Thermodynamically constrained averaging theory approach for modeling flow and transport phenomena in porous medium systems: 1. Motivation and overview." *Advances in Water Resources*, 28(2), 161–180.

Gray, W. G. and Miller, C. T. (2006). "Thermodynamically constrained averaging theory approach for modeling flow and transport phenomena in porous medium systems: 3. Single-fluid-phase flow." *Advances in Water Resources*, 29(11), 1745–1765.

Gray, W. G. and Miller, C. T. (2009). "Thermodynamically constrained averaging theory approach for modeling flow and transport phenomena in porous medium systems: 5. Single-fluid-phase transport." *Advances in Water Resources*, 32(5), 681–711.

Gray, W. G. and Miller, C. T. (2010). "Thermodynamically constrained averaging theory approach for modeling flow and transport phenomena in porous medium systems: 8. Interface and common curve dynamics." *Advances in Water Resources*, 33(12), 1427–1443.

Gray, W. G. and Miller, C. T. (2013). "A generalization of averaging theorems for porous medium analysis." *Advances in Water Resources*, 62, 227–237.

Gray, W. G. and Miller, C. T. (2014). *Introduction to the Thermodynamically Constrained Averaging Theory for Porous Medium Systems*. Springer, Switzerland.

Gray, W. G., Miller, C. T., and Schrefler, B. A. (2013). "Averaging theory for description of environmental problems: What have we learned?." *Adv Water Resour*, 51, 123–138.

Greenshields, C. J. (2019). *OpenFOAM User Guide*. The OpenFOAM Foundation, Christopher J. Greenshields, 7 edition (July).

Gruber, M., Johnson, C., Tang, C., Jensen, M., Yde, L., and Hélix-Nielsen, C. (2011). "Computational fluid dynamics simulations of flow and concentration polarization in forward osmosis membrane systems." *Journal of Membrane Science*, 379(1), 488 – 495.

Gruber, M. F., Aslak, U., and H©lix-Nielsen, C. (2016). "Open-source cfd model for optimization of forward osmosis and reverse osmosis membrane modules." *Separation and Purification Technology*, 158, 183 – 192.

Guermond, J. and Nazarov, M. (2014). "A maximum-principle preserving c^0 finite element method for scalar conservation equations." *Computer Methods in Applied Mechanics and Engineering*, 272, 198–213.

Guermond, J., Nazarov, M., Popov, B., and Tomas, I. (2018). "Second-order invariant domain preserving approximation of the euler equations using convex limiting." *SIAM Journal on Scientific Computing*, 40(5), A3211–A3239.

Guermond, J., Pasquetti, R., and Popov, B. (2010). "From suitable weak solutions to entropy viscosity." *Quality and Reliability of Large-Eddy Simulations II*, ERCOFTAC Series, Springer.

Guermond, J.-L., de Luna, M. Q., and Thompson, T. (2017). "An conservative anti-diffusion technique for the level set method." *Journal of Computational and Applied Mathematics*, 321, 448 – 468.

Guermond, J.-L., Nazarov, M., Popov, B., and Yang, Y. (2014). "A second-order maximum principle preserving lagrange finite element technique for nonlinear scalar conservation equations." *SIAM Journal on Numerical Analysis*, 52(4), 2163–2182.

Guermond, J.-L., Pasquetti, R., and Popov, B. (2011). "Entropy viscosity method for nonlinear conservation laws." *Journal of Computational Physics*, 230(11), 4248 – 4267 Special issue High Order Methods for CFD Problems.

Guermond, J.-L. and Popov, B. (2014). "Viscous regularization of the euler equations and entropy principles." *SIAM Journal on Applied Mathematics*, 74(2), 284–305.

Guermond, J.-L. and Popov, B. (2017). "Invariant domains and second-order continuous finite element approximation for scalar conservation equations." *SIAM Journal on Numerical Analysis*, 3120–3146.

Hamer, W. J. and Wu, Y.-C. (1972). "Osmotic coefficients and mean activity coefficients of uni-univalent electrolytes in water at 25 ° c." *Journal of Physical and Chemical Reference Data*, 1(4), 1047–1100.

Harten, A., Hyman, J. M., Lax, P. D., and Keyfitz, B. (1976). "On finite-difference approximations and entropy conditions for shocks." *Communications on Pure and Applied Mathematics*, 29(3), 297–322.

Harten, A., Lax, P. D., and van Leer, B. (1997). *On Upstream Differencing and Godunov-Type Schemes for Hyperbolic Conservation Laws*. Springer Berlin Heidelberg, Berlin, Heidelberg, 53–79.

Hassanizadeh, S. (1990). "Experimental study of coupled flow and mass transport: A model validation exercise." *Model CARE*, 90, 241–250.

Hassanizadeh, S. M. (1986). "Derivation of basic equations of mass transport in porous media, part 2. Generalized Darcy's and Fick's laws." *Advances in Water Resources*, 9(4), 207–222.

Hassanizadeh, S. M. (1996). "On the transient non-Fickian dispersion theory." *Transport in Porous Media*, 23(1), 107–124.

Hassanizadeh, S. M. and Leijnse, A. (1995). "A non linear theory of high-concentration-gradient dispersion in porous media." *Advances in Water Resources*, 18(4), 203–215.

Hassanizadeh, S. M. and Leijnse, T. (1988). "On the modeling of brine transport in porous media." *Water Resources Research*, 24(3), 321–330.

Hauswirth, S. (2019) (January).

Hill, E. H., Moutier, M., Alfaro, J., and Miller, C. T. (2001). "Remediation of DNAPL pools using dense-brine barrier strategies." *Environmental Science & Technology*, 35(14), 3031–3039.

Hindmarsh, A. C., Brown, P. N., Grant, K. E., Lee, S. L., Serban, R., Shumaker, D. E., and Woodward, C. S. (2005). "SUNDIALS: Suite of nonlinear and differential/algebraic equation solvers." *ACM Transactions on Mathematical Software (TOMS)*, 31(3), 363–396.

Homsy, G. M. (1987). "Viscous fingering in porous media." *Annual Review of Fluid Mechanics*, 19, 271–311.

Ibaraki, M. (1998). "A robust and efficient numerical model for analyses of density-dependent flow in porous media." *Journal of Contaminant Hydrology*, 34(3), 235 – 246.

Icardi, M., Boccardo, G., Marchisio, D. L., Tosco, T., and Sethi, R. (2014). "Pore-scale simulation of fluid flow and solute dispersion in three-dimensional porous media." *Phys. Rev. E*, 90, 013032.

Issa, R. (1986). "Solution of the implicitly discretised fluid flow equations by operator-splitting." *Journal of Computational Physics*, 62(1), 40 – 65.

Jackson, A. S., Miller, C. T., and Gray, W. G. (2009). "Thermodynamically constrained averaging theory approach for modeling flow and transport phenomena in porous medium systems: 6. Two-fluid-phase flow." *Advances in Water Resources*, 32(6), 779–795.

Jackson, A. S., Rybak, I., Helmig, R., Gray, W. G., and Miller, C. T. (2012). "Thermodynamically constrained averaging theory approach for modeling flow and transport phenomena in porous medium systems: 9. Transition region models." *Advances in Water Resources*, 42, 71–90.

Jiao, C. Y. and Hötzl, H. (2004). "An experimental study of miscible displacements in porous media with variation of fluid density and viscosity." *Transport in Porous Media*, 54(2), 125–144.

Johannsen, K., Kinzelbach, W., Oswald, S., and Wittuma, G. (2002). "The saltpool benchmark problem a numerical simulation of saltwater upconing in a porous medium." *Advances in Water Resources*, 25(3), 335 – 348.

Johnson, D. N., Pedit, J. A., and Miller, C. T. (2004). "Efficient, near-complete removal of DNAPL from three-dimensional, heterogeneous porous media using a novel combination of treatment technologies." *Environmental Science & Technology*, 38(19), 5149–5156.

Johnson, S. G. (2014). "The NLopt nonlinear-optimization package.

Kanney, J. F., Miller, C. T., and Kelley, C. T. (2002). "Convergence of iterative split-operator approaches for approximating nonlinear reactive transport problems." *American Geophysical Union Spring Meeting*, Vol. 83(19), Washington, DC, American Geophysical Union, S198.

Kaslusky, S. F. and Udell, K. S. (2002). "A theorectical model of air and steam co-injection to prevent the downward migration of DNAPLs during steam-enhanced extraction." *Journal of Contaminant Hydrology*, 55(3–4), 213–232.

Kees, C. E. and Miller, C. T. (1999). "C++ implementations of numerical methods for solving differential-algebraic equations: Design and optimization considerations." *Association for Computing Machinery, Transactions on Mathematical Software*, 25(4), 377–403.

Kees, C. E. and Miller, C. T. (2002). "Higher order time integration methods for two-phase flow." *Advances in Water Resources*, 25(2), 159–177.

Ketabchi, H., Mahmoodzadeh, D., Ataie-Ashtiani, B., and Simmons, C. T. (2016). "Sea-level rise impacts on seawater intrusion in coastal aquifers: Review and integration." *Journal of Hydrology*, 535, 235–255.

Knabner, P. and Frolkovic, P. (1996). "Consistent velocity approximation for finite volume or element discretizations of density driven flow in porous media." *Computational Methods in Water Resources XI, Volume 1, Computational Methods in Subsurface Flow and Transport Problems*, A. A. Aldama, J. Aparicio, C. A. Brebbia, W. G. Gray, I. Herrera, and G. F. Pinder, eds., Cancun, Mexico, Computational Mechanics Publications, 93–100.

Kolditz, O., Ratke, R., Diersch, H. J. G., and Zielke, W. (1998). "Coupled groundwater flow and transport: 1. Verification of variable density flow and transport models." *Advances in Water Resources*, 21(1), 27–46.

Konz, M., Younes, A., Ackerer, P., Fahs, M., Huggenberger, P., and Zechner, E. (2009). "Variable-density flow in heterogeneous porous media—laboratory experiments and numerical simulations." *Journal of contaminant hydrology*, 108(3), 168–175.

Koponen, A., Kataja, M., and Timonen, J. (1996). "Tortuous flow in porous media." *Phys. Rev. E*, 54, 406–410.

Kuzmin, D. (2006). "On the design of general-purpose flux limiters for finite element schemes. i. scalar convection." *Journal of Computational Physics*, 219(2), 513 – 531.

Kuzmin, D. and Turek, S. (2002). "Flux correction tools for finite elements." *Journal of Computational Physics*, 175(2), 525 – 558.

Landman, A. J., Johannsen, K., and Schotting, R. (2007a). "Density-dependent dispersion in heterogeneous porous media Part I: A numerical study." *Advances in Water Resources*, 30(12), 2467–2480.

Landman, A. J., Schotting, R., Egorov, A., and Demidov, D. (2007b). "Density-dependent dispersion in heterogeneous porous media Part II: Comparison with nonlinear models." *Advances in Water Resources*, 30(12), 2481–2498.

Lax, P. (1971). "Shock waves and entropy." *Contributions to Nonlinear Functional Analysis*, E. H. Zarantonello, ed., Academic Press, 603 – 634.

Lee, S. and Wheeler, M. F. (2017). "Adaptive enriched galerkin methods for miscible displacement problems with entropy residual stabilization." *Journal of Computational Physics*, 331, 19 – 37.

LeVeque, R. J. (1992). *Numerical Methods for Conservation Laws*. Springer, Basel, Switzerland.

LeVeque, R. J. (2002). *Finite Volume Methods for Hyperbolic Problems*. Cambridge University Press, Cambridge, United Kingdom.

Li, H., Farthing, M. W., Dawson, C. N., and Miller, C. T. (2007). "Local discontinuous Galerkin approximations to Richards' equation." *Advances in Water Resources*, 30(4), 555–575.

McClure, J. E., Armstrong, R. T., Berrill, M. A., Schlüeter, S., Berg, S., Gray, W. G., and Miller, C. T. (2018). "A geometric state function for two-fluid flow in porous media." *Physical Review Fluids*, 3(8), 084306.

McClure, J. E., Dye, A. L., Miller, C. T., and Gray, W. G. (2017). "On the concistency of scale among experiments, theory, and simulation." *Hydrology and Earth System Sciences*, 21, 1063–1076.

Miller, C. T., Abhishek, C., and Farthing, M. W. (2006). "A spatially and temporally adaptive solution of Richards equation." *Advances in Water Resources*, 29(4), 525–545.

Miller, C. T., Bruning, K., Talbot, C. L., McClure, J. E., and Gray, W. G. (2019a). "Non-hysteretic capillary pressure in two-fluid porous media: Definition, evaluation, validation, and dynamics." *Water Resources Research*.

Miller, C. T., Dawson, C. N., Farthing, M. W., Hou, T. Y., Huang, J. F., Kees, C. E., Kelley, C. T., and Langtangen, H. P. (2013). "Numerical simulation of water resources problems: Models, methods, and trends." *Advances in Water Resources*, 51, 405–437.

Miller, C. T., Farthing, M. W., Kees, C. E., Dye, A. L., Weigand, T. M., Schultz, P. B., and Adalsteinsson, D. (2016). "Groundwater modeling." *The Handbook of Groundwater Engineering*, J. H. Cushman and D. M. Tartakovsky, eds., CRC Press, 3rd edition.

Miller, C. T. and Gray, W. G. (2005). "Thermodynamically constrained averaging theory approach for modeling flow and transport phenomena in porous medium systems: 2. Foundation." *Advances in Water Resources*, 28(2), 181–202.

Miller, C. T. and Gray, W. G. (2008). "Thermodynamically constrained averaging theory approach for modeling flow and transport phenomena in porous medium systems: 4. Species transport fundamentals." *Advances in Water Resources*, 31(3), 577–597.

Miller, C. T., Gray, W. G., and Kees, C. E. (2018a). "Thermodynamically constrained averaging theory: principles, model hierarchies, and deviation kinetic energy extensions." *Entropy*, 20(4)(253).

Miller, C. T., Gray, W. G., Kees, C. E., Rybak, I. V., and Shepherd, B. J. (2019b). "Modeling sediment transport in three-phase surface water systems." *In press: Journal of Hydraulic Research*.

Miller, C. T., Hill, E. H., and Moutier, M. (2000). "Remediation of DNAPL-contaminated subsurface systems using density-motivated mobilization." *Environmental Science & Technology*, 34(4), 719–724.

Miller, C. T., Valdés-Parada, F. J., Ostvar, S., and Wood, B. D. (2018b). "A priori parameter estimation for the thermodynamically constrained averaging theory: Species transport in a saturated porous medium." *Transport in Porous Media*, 122(3), 611–632.

Miller, C. T., Valdés-Parada, F. J., and Wood, B. D. (2017). "A pedagogical approach to the thermodynamically constrained averaging theory." *Transport in Porous Meda*, 119, 585–609.

Mills, R. (1973). "Self-diffusion in normal and heavy water in the range 1-45. deg.." *The Journal of Physical Chemistry*, 77(5), 685–688.

Nick, H., Schotting, R., Gutierrez-Neri, M., and Johannsen, K. (2009). "Modeling transverse dispersion and variable density flow in porous media." *Transport in porous media*, 78(1), 11–35.

Noordman, T. and Wesselingh, J. (2002). "Transport of large molecules through membranes with narrow pores: The maxwellâìstefan description combined with hydrodynamic theory." *Journal of Membrane Science*, 210(2), 227 – 243.

Oldenburg, C. M. and Pruess, K. (1995). "Dispersive transport dynamics in a strongly coupled groundwater brine flow system." *Water Resources Research*, 31(2), 289–302.

Osher, S. (1984). "Riemann solvers, the entropy condition, and difference approximations." *SIAM Journal on Numerical Analysis*, 21(2), 217–235.

Osher, S. and Chakravarthy, S. R. (1984). "High resolution schemes and the entropy condition." *SIAM Journal on Numerical Analysis*, 21, 955–984.

Pellegrini, F. (2008). "Scotch and libScotch 5.1 User's Guide, <https://hal.archives-ouvertes.fr/hal-00410327> (August). User's manual.

Powell, M. J. (1994). "A direct search optimization method that models the objective and constraint functions by linear interpolation." *Advances in optimization and numerical analysis*, Springer, 51–67.

Puppo, G. (2003). "Numerical entropy production for central schemes." *SIAM J. Sci. Comput.*, 25(4), 1382–1415.

Rybak, I. V., Gray, W. G., and Miller, C. T. (2015). "Modeling two-fluid-phase flow and species transport in porous media." *Journal of Hydrology*, 521, 565–581.

Schotting, R. and Landman, A. (2004). "Towards a physically based theory of high-concentration-gradient dispersion in porous media." *Emerging Technologies and Techniques in Porous Media*, 321–336.

Schotting, R. J., Moser, H., and Hassanizadeh, S. M. (1999). "High-concentration-gradient dispersion in porous media: Experiments, analysis and approximations." *Advances in Water Resources*, 22(7), 665–680.

Schroth, M. H., Ahearn, S. J., Selker, J. S., and Istok, J. D. (1996). "Characterization of Miller-similar silica sands for laboratory hydrologic studies." *Soil Science Society of America Journal*, 60(5), 1331–1339.

Sharp, D. (1984). "An overview of rayleigh-taylor instability." *Physica D: Nonlinear Phenomena*, 12(1), 3 – 18.

Shen, L. and Chen, Z. (2007). "Critical review of the impact of tortuosity on diffusion." *Chemical Engineering Science*, 62(14), 3748–3755.

Siena, M., Riva, M., Hyman, J. D., Winter, C. L., and Guadagnini, A. (2014). "Relationship between pore size and velocity probability distributions in stochastically generated porous media." *Phys. Rev. E*, 89, 013018.

Simmons, C. T., Fenstemaker, T. R., and Sharp, J. M. (2001). "Variable-density groundwater flow and solute transport in heterogeneous porous media: approaches, resolutions and future challenges." *Journal of Contaminant Hydrology*, 52(1-4), 245–275.

Slobod, R. (1964). "The effects of gravity segregation in laboratory studies of miscible displacement in vertical unconsolidated porous media." *Society of Petroleum Engineers Journal*, 4(01), 1–8.

Smith, R. L., Harvey, R. W., and LeBlanc, D. R. (1991). "Importance of closely spaced vertical sampling in delineating chemical and microbiological gradients in groundwater studies." *Journal of Contaminant Hydrology*, 7, 285–300.

Smoller, J. (1994). *Shock waves and reaction—diffusion equations; 2nd ed.* Grundlehren der mathematischen Wissenschaften A Series of Comprehensive Studies in Mathematics. Springer, New York, <http://cds.cern.ch/record/1609381>.

Starr, J. L. and Parlange, J. Y. (1976). "Solute dispersion in saturated soil columns." *Soil Science*, 121(6), 364–372.

Steefel, C. I., Arora, B., Molins, S., Spycher, N., Appelo, C. A. J., Jacques, D., Kalbacher, T., Kolditz, O., Shao, H., Lagneau, V., Lichtner, P. C., Mayer, K. U., Meeussen, J. C. L., Moulton, D., Simunek, J., Yabusaki, S. B., and Yeh, G. T. (2015). "Reactive transport codes for subsurface environmental simulation." *Comput. Geosci. Computational Geosciences*, 19(3), 445–478.

Svanberg, K. (1987). "The method of moving asymptotes—a new method for structural optimization." *International journal for numerical methods in engineering*, 24(2), 359–373.

Tadmor, E. (1990). "Shock capturing by the spectral viscosity method." *Computer Methods in Applied Mechanics and Engineering*, 80(1), 197 – 208.

Virtanen, P., Gommers, R., Oliphant, T. E., Haberland, M., Reddy, T., Cournapeau, D., Burovski, E., Peterson, P., Weckesser, W., Bright, J., van der Walt, S. J., Brett, M., Wilson, J., Jarrod Millman, K., Mayorov, N., Nelson, A. R. J., Jones, E., Kern, R., Larson, E., Carey, C., Polat, İ., Feng, Y., Moore, E. W., Vand erPlas, J., Laxalde, D., Perktold, J., Cimrman, R., Henriksen, I., Quintero, E. A., Harris, C. R., Archibald, A. M., Ribeiro, A. H., Pedregosa, F., van Mulbregt, P., and Contributors, S. . . (2019). "SciPy 1.0–Fundamental Algorithms for Scientific Computing in Python." *arXiv e-prints*, arXiv:1907.10121.

VonNeumann, J. and Richtmyer, R. D. (1950). "A method for the numerical calculation of hydrodynamic shocks." *Journal of Applied Physics*, 21(3), 232–237.

Voss, C. I. (1984). "A finite-element simulation model for saturated-unsaturated, fluid-density-dependent ground-water flow with energy transport or chemically-reactive single-species solute transport." *Report No. U.S. Geological Survey Water-Resources Investigations Report 84-4369*, U.S. Geological Survey.

Watson, S. J., Barry, D. A., Schotting, R. J., and Hassanizadeh, S. M. (2002a). "On the validity of Darcy's law for stable high-concentration displacements in granular porous media." *Transport in Porous Media*, 47(2), 149–167.

Watson, S. J., Barry, D. A., Schotting, R. J., and Hassanizadeh, S. M. (2002b). "Validation of classical density-dependent solute transport theory for stable, high-concentration-gradient brine displacements in coarse and medium sands." *Advances in Water Resources*, 25(6), 611–635.

Watson, S. J., Barry, D. A., Schotting, R. J., and Hassanizadeh, S. M. (2002c). "Validation of classical density-dependent solute transport theory for stable, high-concentration-gradient brine displacements in coarse and medium sands." *Advances in Water Resources*, 25(6), 611–635.

Weigand, T. M., Harrison, E. C., and Miller, C. T. (2017). "Evaluation and validation of a tcat model to describe non-dilute flow and species transport in porous media." *American Geophysical Union, Fall Meeting 2017, abstract H11F-1244*.

Weigand, T. M., Schultz, P. B., Giffen, D. H., Farthing, M. W., Crockett, A., Kelley, C. T., Gray, W. G., and Miller, C. T. (2018a). "Modeling nondilute species transport using the thermodynamically constrained averaging theory." *Water Resources Research*, 54(9), 6656–6682.

Weigand, T. M., Schultz, P. B., Giffin, D. H., Farthing, M. W., Crockett, A., Kelley, C. T., Gray, W. G., and Miller, C. T. (2018b). "Modeling non-dilute species transport using the thermodynamically constrained averaging theory." *Water Resources Research*, 54, 6656–6682.

Weiser, A. and Wheeler, M. F. (1988). "On convergence of block-centered finite differences for elliptic problems." *SIAM Journal on Numerical Analysis*, 25(2), 351–375.

Weller, H. G., Tabor, G., Jasak, H., and Fureby, C. (1998). "A tensorial approach to computational continuum mechanics using object-oriented techniques." *Comput. Phys.*, 12(6), 620–631.

Welty, C. and Gelhar, L. W. (1991). "Stochastic analysis of the effects of fluid density and viscosity variability on macrodispersion in heterogeneous porous media." *Water Resources Research*, 27(8), 2061–2075.

Werner, A. D., Bakker, M., Post, V. E., Vandenbohede, A., Lu, C., Ataie-Ashtiani, B., Simmons, C. T., and Barry, D. A. (2013). "Seawater intrusion processes, investigation and management: recent advances and future challenges." *Advances in Water Resources*, 51, 3–26.

Widdowson, M. A., Molz, F. J., and Benefield, L. D. (1988). "A numerical transport model for oxygen- and nitrate-based respiration linked to substrate and nutrient availability in porous media." *Water Resources Research*, 24(9), 1553–1565.

Wright, D. J., Pedit, J. A., Farthing, M. W., Murphy, L. L., Brubaker, G. R., Knight, S. R., and Miller, C. T. (2009). "Dense, viscous brine behavior in heterogeneous porous medium systems." *Journal of Contaminant Hydrology*, 115(1-4), 46–63.

Xin, J. and Flaherty, J. E. (2006). "Viscous stabilization of discontinuous galerkin solutions of hyperbolic conservation laws." *Applied Numerical Mathematics*, 56(3), 444 – 458 Selected Papers, The Third International Conference on the Numerical Solutions of Volterra and Delay Equations.